GEOTECHNICAL RESEARCH CENTRE

GRC STUDIES ON MOBILITY AND PERFORMANCE:

a) ROAD SURFACE ROUGHNESS
b) INFLUENCE OF SNOWPACK

SOIL MECHANICS SERIES NO. 58

December 1993

McGill University
Montreal, Que Canada

ISSN 0541-6329

F O R E W O R D

The following selection of papers on **Mobility and Performance: a) Road Surface Roughness and b) Influence of Snowpack**, has recently been published in the Journal of Terramechanics, and in the Proceedings of the 4th Regional North American Meeting of the International Society for Terrain-Vehicle Systems:

1. Xu, D-M. and <u>Yong, R.N.</u> (1993)
   Autocorrelation Model of Road Roughness
   Journal of Terramechanics, 30-4:259-274.

2. Xu, D-M., Mohamed, A.M.O., <u>Yong, R.N.</u> and Caporuscio, F. (1992)
   Development of Criterion for Road Surface Roughness based on Power Spectral Density Function
   Proceedings, ISTVS 4th Regional North American Meeting, pp.306-315.

3. Mohamed, A.M.O., <u>Yong, R.N.</u> and Murcia, A.J. (1993)
   Evaluation of the Performance of Deep Snowpack under Compression Loading using Finite Element Analysis
   Journal of Terramechanics, 30-4:219-257.

4. Irwin, G.J., Xu, D-M., Mohamed, A.M.O. and <u>Yong, R.N.</u> (1992)
   Trafficability Evaluation of Deep Snowpack
   Proceedings, ISTVS 4th Regional North American Meeting, pp.259-265.

Journal of Terramechanics, Vol. 30, No. 4, pp. 259–274, 1993.
Printed in Great Britain.
0022-4898/93 $6.00+0.00
Pergamon Press Ltd

AUTOCORRELATION MODEL OF ROAD ROUGHNESS

DA-MING XU* and RAYMOND N. YONG*

Summary—Road surface roughness is the excitation source for the dynamic response of a moving vehicle system. Driving comfort is indicated by either the driver absorbed power level or the vehicle vertical acceleration level. An autocorrelation function model for road roughness is proposed to specify the road surface random characteristics. Subsequently, the power spectral densities (PSDs) for both road roughness and vehicle response, the driver-absorbed power level, are formulated. A road quality index (RQI) in accordance with such energy considerations is defined to catalog the road grade. The laboratory test results show the applicability of the RQI method for road classification using the ISO criteria as a comparison check.

INTRODUCTION

PREDICTION of vehicle mobility over rough terrain has always been hampered by a lack of rational tools to assess riding road surface roughness. In part, this is due to the problems involved in the complicated measurement of a "true" representative road surface profile and the data treatment in regarding to an inherent random process, and in part on the development of adequate modelling procedures. During the past 30 years or so, various methods have been proposed for evaluation of road service condition. Qualitatively speaking, the effects of road roughness on driving safety, driving comfort, energy consumption and deterioration to both vehicles and roads due to dynamic loading are well known. From a qualitative point of view, none of these effects can be properly rationalized except through empirical models.

Road surface roughness itself is not an easily explained concept even though several definitions have been proposed. In the subjective sense, road surface geometric irregularity may characterize the road roughness essence from geometric point of view. It includes the road surface ruts, cracks, patches, irregularities and "bumps", developed during service life of the road under traffic flow and weathering conditions. This is represented by a road profile measurement. This understanding is still, somehow, not precise, so far as the filtering effect is concerned, because what a vehicle "sees" may not be an original road surface profile. This suggests the need for an investigation of interaction between a vehicle system and a rough road, which considers the vehicle response. It is customary to classify the road surface condition into various grades: i.e. very good, good, satisfactory, poor and very poor. Regular survey of the road condition is an important and necessary routine task in the management and maintenance of highway (road) service.

The general method for classification of road conditions is based on observation

*Geotechnical Research Centre, McGill University, 817 Sherbrooke St. W., Montreal, Quebec, Canada H3A 2K6.

and measurement of ruts, patches, cracks and irregularities, to obtain a so called PSI value (Present Serviceability Index) through a regression equation [1, 2]. Though this classical method is physically sound, one is required to measure total crack lengths, crack opening sizes, number of total ruts and patches, and the slope variations in a unit road surface area (normally 1000 ft^2 (93 m^2)). This involves considerable field measurements. In the final analysis, road surface quality is generally determined (judged) by the roads engineer's experience.

Techniques for road classification developed in the past 30 years are quite fascinating. Among them, the panel rating method in Ontario, Canada, and some states of the U.S.A., the pattern recognition method in New York state, the Major meter method, the average slope method, the average acceleration method (response type of measurement methods) etc. are still adopted in road survey practice. However, the PSD (Power Spectral Density) method for road classification [3, 4] based on road profile measurement tends to get more and more attention. The international organization for standardization, ISO, has proposed a road roughness classification (class a to h) in 1982 [5–7] using this method, i.e. random process data treatment. Some characteristics of the method, however, need to be further developed, e.g. the assumed linear form PSD distribution over the spatial frequency domain in log–log plot is not quite correct (especially for the low frequency band), since the area under the PSD curve, which represents the mean square value, will yield an infinite value. Additionally, the assumption of certain types of distribution of PSD may not represent the actual road PSD distribution, and the classification of road grade is only based on the PSD value at spatial frequency $\Omega_0 = 1/2\pi$ (cycle/meter).

The PSD method is superior to the classic field measurement method, as it opens a way for road classification without involving much field measurement. Further development of the PSD method requires one to provide more physical sense to the mathematical treatment. For example, the physical unit used is m^3/cycle, which is neither a force unit nor a power unit, but some strange unit not frequently encountered in the engineering field. To address this problem, the theoretical development presented in this study uses energy relationships in considering the human body absorbed power level in relation to rough road surfaces.

A two-parameter autocorrelation model is proposed. One parameter is the root mean square (RMS) value σ of the rough road height and the other is an exponential parameter which specifies the correlation degree. The use of two parameters provides one with a better opportunity to represent the real road roughness. Subsequently, PSDs for road roughness and vehicle response, driver absorbed power level are formulated, and a Road Quality Index (RQI) is used to classify the road condition.

AUTOCORRELATION MODEL

A schematic representation of a rough road is shown in Fig. 1. $y(x)$ denotes the height at a distance of x away from the reference. $y(x)$ is a random function and is best explained as follows: with the same vehicle, same speed, same driver and same weather conditions, for each driving test (assuming a total of n tests) on a rough road, a different record will probably be obtained. This is because it is very difficult for a vehicle to be driven along an exact repeatable lane. It is assumed that the

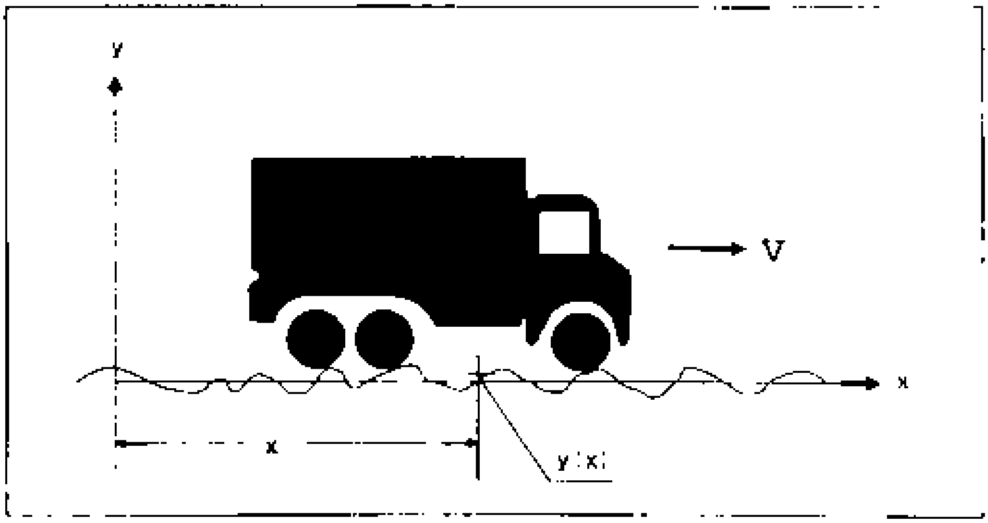

FIG. 1. Schematic of a vehicle moving on a rough road surface.

surface is not deformable, i.e. the surface roughness is expected to be rigid and will not distort under load.

The autocorrelation function is defined as:

$$R(x, \mu) = E[y(x)y(x + \mu)] \quad (1)$$

where μ = spatial difference. The symbol E represents the mathematical expectation. If we assume that the random process $y(x)$ is stationary, then $R(x, \mu)$ is independent of x. If we further assume that the random process $y(x)$ is ergodic, and using $R(\mu)$ instead of $R(x, \mu)$, we will have:

$$R(\mu) = \left(\frac{1}{L}\right)\int_0^L y(x)y(x + \mu)\,\mathrm{d}x. \quad (2)$$

Theoretically speaking, L is supposed to approach ∞. However, from an engineering point view, L is taken to be sufficiently large to assure that $R(\mu)$ is stable.

The autocorrelation function $R(\mu)$ has three properties:

(a) It is an even function;
(b) $R(0)$ at maximum $= \sigma^2$;
(c) When μ reaches ∞, $R(\mu)$ reaches 0.

Based on the above properties, $R(\mu)$ is modelled as:

$$R(\mu) = \sigma^2 \exp[-a^2\mu^2]. \quad (3)$$

This model satisfies all properties (a), (b) and (c). It involves two parameters σ and a. σ is the root mean square value, and portrays the information on the road surface "amplitude", and parameter a specifies the correlation degree. If a is small, the curve $R(\mu)$ is "flatter", indicating a tight correlation. This parameter provides the frequency information—as will be seen later in the PSD distribution. Figure 2 shows the general shape of $R(\mu)$.

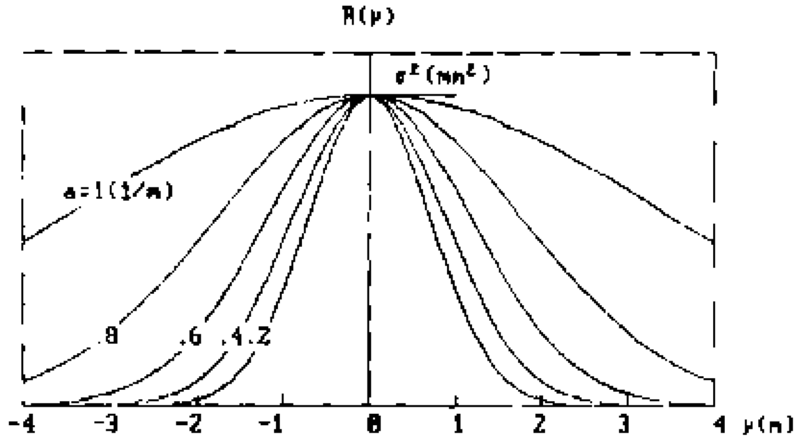

FIG. 2. Autocorrelation function $R(\mu)$.

PSD FOR ROAD ROUGHNESS

$R(\mu)$ and PSD, $S_y(\Omega)$ are paired Fourier Transforms. Since $R(\mu)$ is an even function, we have:

$$S_y(\Omega) = \frac{1}{\pi}\int_0^{\infty} R(\mu)\cos(\Omega\mu)\,d\mu \tag{4}$$

where Ω is the spatial frequency in rad/m. Substituting equation (3) into equation (4), we have:

$$S_y(\Omega) = [\sigma^2/(2a\sqrt{\pi})]\exp[-\Omega^2/(4a^2)]. \tag{5}$$

$S(\Omega)$ specifies the power spectral density distribution with respect to road roughness height y, which is shown in Fig. 3.

From equation (5), it is noted that the value of $S_y(\Omega)$ is a function of Ω and two parameters σ and a. If a is fixed, then for different values of σ, the $S(\Omega)$ curves show similar shapes—albeit with different values.

One basic factor needs to be emphasized: the vehicle response. If the vehicle is modelled as a one-degree mass spring–dashpot system, and if road roughness is

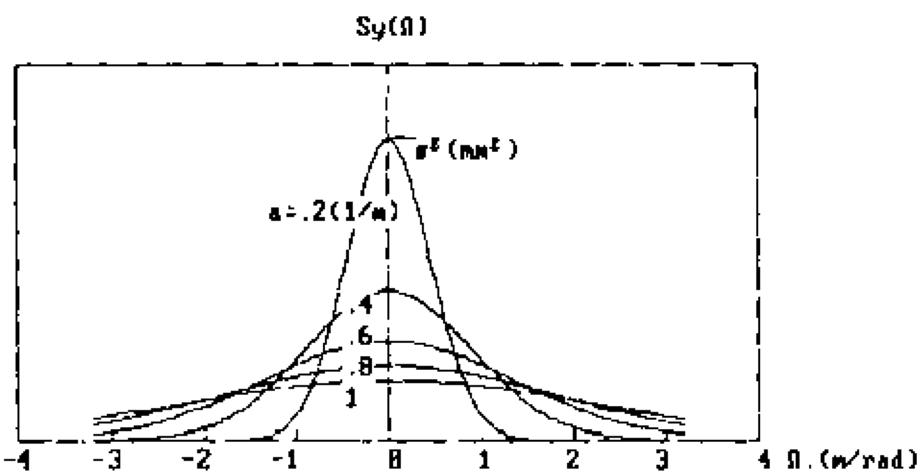

FIG. 3. Power spectral density $S_y(\Omega)$.

regarded as an excitation source, then the excitation a vehicle senses from road roughness is also a random process regardless of whether the excitation is represented as a force excitation or an acceleration excitation. To an individual vehicle, response excitation is related to road roughness, as well as the vehicle system characteristics -especially the natural frequency of the system. The judgment of the road condition is directly related to vehicle excitation rather than road roughness itself. This argument suggests it is necessary to consider the PSD of vehicle response.

PSD $S_v(\Omega)$ OF VEHICLE RESPONSE

The PSD $S_v(\omega)$ of the vehicle response v is also a stationary random process where v denotes the vibrational displacement of a vehicle system. $S_v(\omega)$ is linked to $S_y(\omega)$ in the following term:

$$S_v(\omega) = S_y(\omega)/|H(\omega)|^2 \tag{6}$$

where $H(\omega)$ is the vehicle system characteristic function. Frequency ω is related to spatial frequency Ω as:

$$\omega = V\Omega \tag{7}$$

where V is vehicle speed. In using equations (5), (6) and (7), we obtain $S_v(\Omega)$ as:

$$S_v(\Omega) = [\sigma^2/(2a\sqrt{\pi})]\exp[-\Omega^2/(4a^2)]/|H(\Omega)|^2. \tag{8}$$

If a spring–mass–dashpot system is used to model the vehicle system dynamic behaviour, the system equation is described as:

$$M\,\mathrm{d}^2v/\mathrm{d}t^2 + C\,\mathrm{d}v/\mathrm{d}x + Kv = C\,\mathrm{d}y/\mathrm{d}t + Ky. \tag{9}$$

The RHS term is the excitation term from the road roughness. M, C and K denote mass, damping coefficient and spring constant, respectively. The characteristic function $H(\omega)$ is described as:

$$H(\omega) = \{[1-(\omega/\omega_0)^2] + 2\xi(\omega/\omega_0)i\}/\{1 + 2\xi\,(\omega/\omega_0)i\} \tag{10}$$

where ω_0 is the natural frequency of the vehicle system. i is $\sqrt{-1}$, and ξ is the damping ratio. ω_0 and ξ are given by:

$$\omega_0 = \sqrt{(K/M)} \tag{11}$$

and

$$\xi = \sqrt{C/[2KM]}. \tag{12}$$

Accordingly, $|H(\omega)|^2$ is given as:

$$|H(\omega)|^2 = \{[1-(\omega/\omega_0)^2]^2 + 4\xi^2(\omega/\omega_0)^2\}/\{1 + 4\xi^2(\omega/\omega_0)^2\}. \tag{13}$$

Equations (6) and (13) are written in time t domain, and are not convenient for rough road representation since the vehicle speed V is not unique. They can be represented in space x domain according to the following linear transformation:

$$\mathrm{d}x = V\,\mathrm{d}t \tag{14}$$

and we have

$$\omega/\omega_0 = \Omega/\Omega_0 \tag{15}$$

and

$$1/|H(\Omega)|^2 = [1 + 4\xi^2(\Omega/\Omega_0)^2]/\{[1 - (\Omega/\Omega_0)^2]^2 + 4\xi^2(\Omega/\Omega_0)^2\} \quad (16)$$

as illustrated in Fig. 4.

Thus, in the spatial x domain, the PSD of the vibrational displacement $v(x)$ response is given as:

$$S_v(\Omega) = [\sigma^2/(2a\sqrt{\pi})]\exp[-\Omega^2/(4a^2)]\{1 + 4\xi^2(\Omega/\Omega_0)^2\} \times \{[1 - (\Omega/\Omega_0)^2]^2 + 4\xi^2(\Omega/\Omega_0)^2\}^{-1}. \quad (17)$$

The general picture of $S_v(\Omega)$ is illustrated in Fig. 5.

VEHICLE KINETIC ENERGY AND ABSORBED POWER BY HUMAN BODY

From the problem at hand, energy relationships represent the most basic sets of considerations. Since the rough road continuously "excites" the vehicle being transported on the rough road surface, the vehicle is in a resultant state of forced vibration. The driver, who is "attached" to the vehicle body mass through the driving

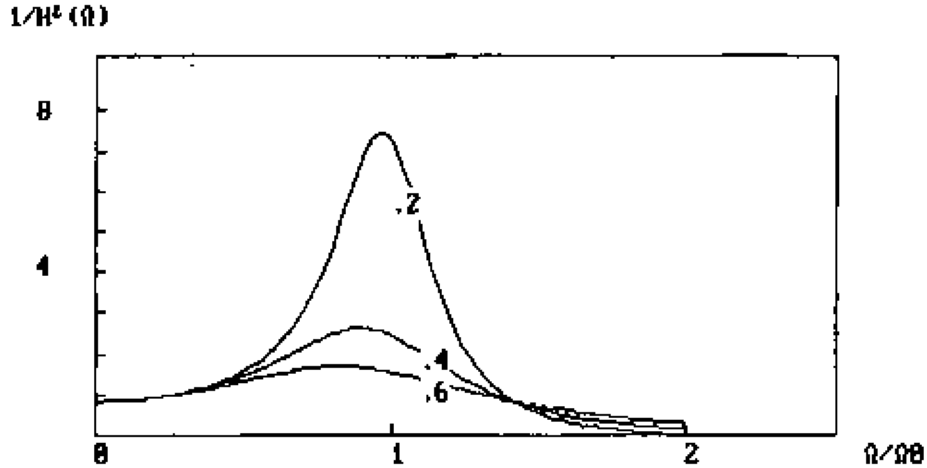

Fig. 4. Vehicle system characteristic function $H^2(\Omega)$ at ξ = 0.2, 0.4 and 0.6.

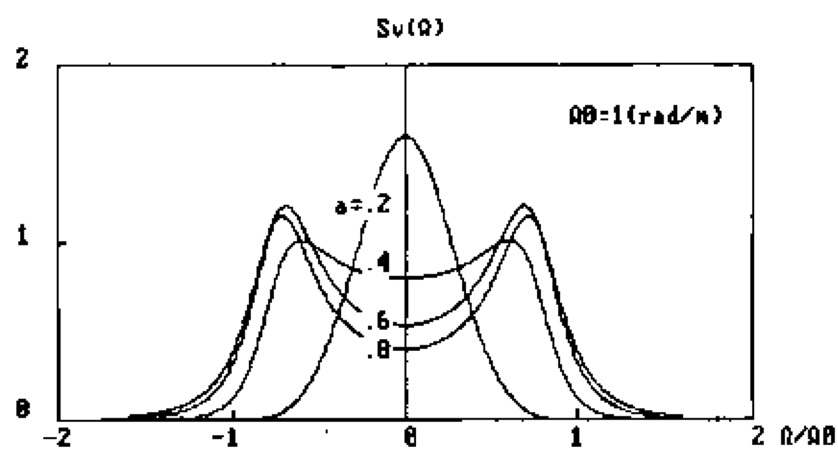

Fig. 5. Power spectral density S_v (Ω).

seat, can be assumed to be vibrating in a similar manner—as if firmly "fixed" to the vehicle. Therefore, the kinetic energy of the vehicle mass associated with vertical vibrational motion is extremely important compared with other energy components such as the dashpot dissipated energy or the spring stored energy (potential energy). The same might be said for the power that a human body in driving absorbs, which is the absorbed kinetic energy in unit time. Experiments have shown that a human body will exhibit considerable distress if the absorbed power reaches 6 watts.* Accordingly, it is useful to classify road roughness according to the level of absorbed power.

The average excited kinetic energy for a unit mass of the vehicle in vertical excitation due to horizontal travel over a rough road given by:

$$E_i = \left(\frac{1}{2T}\right)\int_0^T\left[\frac{\mathrm{d}v_i(t)}{dt}\right]^2 \mathrm{d}t \tag{18}$$

where $v_i(t)$ is ith realization of random process $v(t)$. Since it is assumed that the random process of $y(x)$ is ergodic, $v(t)$ must also be an ergodic random process. Thus, the temporal average of one realization is equal to the ensemble average and it is unique, i.e. $E_i = E_j$ (if i is not equal to j). For simplicity in mathematical representation, a new symbol E_k is used to represent this unique value. Accordingly, one obtains:

$$E_k = 1/2\ E[(\mathrm{d}v/\mathrm{d}t)^2] = R_{\mathrm{d}v/\mathrm{d}t}(0) \tag{19}$$

where E represents the mathematical expectation and $R_{\mathrm{d}v/\mathrm{d}t}(\tau)$ is given as:

$$\begin{aligned} R_{\mathrm{d}v/\mathrm{d}t}(\tau) &= E[\mathrm{d}v(t)/\mathrm{d}t\ \mathrm{d}v(t+\tau)/\mathrm{d}t] \\ &= V^2E[\mathrm{d}v(x)/\mathrm{d}x\ \mathrm{d}v(x+\mu)/\mathrm{d}x] \\ &= V^2R_{\mathrm{d}v/\mathrm{d}x}(\mu) \end{aligned} \tag{20}$$

where τ is time difference, and μ the corresponding spatial difference. Since

$$R_{\mathrm{d}v/\mathrm{d}x}(0) = \int_{-\infty}^{\infty} S_{\mathrm{d}v/\mathrm{d}t}(\Omega)\,\mathrm{d}\Omega \tag{21}$$

and

$$S_{\mathrm{d}v/\mathrm{d}x}(\Omega) = \Omega^2 S_v(\Omega). \tag{22}$$

$S_{\mathrm{d}v/\mathrm{d}x}(\Omega)$ is the PSD with respect to vibration rate $\mathrm{d}v/\mathrm{d}x$. Substituting equation (22) into equation (21) and subsequently equation (21) into equation (20), we have:

$$E_k = V^2\int_0^{\infty}\frac{\Omega^2 S_y(\Omega)}{|H(\Omega)|^2}\,\mathrm{d}\Omega. \tag{23}$$

With the use of equation (17), we obtain:

$$E_k = \left[\frac{V^2\sigma^2}{(2a\sqrt{\pi})}\right]\int_0^{\infty}\Omega^2\exp[-\Omega^2/(4a^2)]\frac{[1+4\xi^2\Omega/\Omega_0)^2]}{\{[1-(\Omega/\Omega_0)^2]^2+4\xi^2(\Omega/\Omega_0)^2\}}\,\mathrm{d}\Omega. \tag{24}$$

*See Ref. [8] on page 142: ". . .One of the principle measures of ride comfort is absorbed power, which is a measure of the rate at which vibrational energy is absorbed by a typical human. A criterion of 6 watts of absorbed power has been established as an upper bound of vibration that will permit crew members to effectively perform their tasks."

Equation (24) gives the estimation of the kinetic energy for a unit mass of the vehicle excited under random vertical excitation from horizontal motion over a rough rigid road surface.

The integration in equation (24) can be performed if the residue theorem is employed (see Appendix A). This leads to:

$$E_k = (V^2\sigma^2 a^2\sqrt{\pi}/c_1)B^3 \exp[-B^2\cos\theta]\{\cos[B^2\sin\theta - \theta/2] + 4\xi^2\cos[B^2\sin\theta - 3\theta/2]\} \tag{25}$$

where

$$c_1 = \xi\sqrt{(1-\xi^2)} \tag{26}$$

$$\theta/2 = \arctan(\xi/\sqrt{(1-\xi^2)}) \tag{27}$$

and

$$B = \Omega_0/(2a). \tag{28}$$

The theoretical relationship between E_k and Ω_0 is shown in Figs 6–9, at $V = 100$ km/h. Parameter a has three values, 0.4, 0.6 and 0.8, while parameter ξ has four values, 0.15, 0.3, 0.45 and 0.6. From Figs 6–9, we notice that:

(1) When ξ is about 0.3, the global level of E_k is smallest compared with others in Figs 6, 8 and 9. This indicates that the vehicle design should adopt a damping ratio of about 0.3 for the vehicle system.

(2) E_k is proportional to σ^2, the mean square value of the rough road height.

(3) For the parameter a, a peak value of E_k at $\Omega_0 \approx 2a$ (approximately) is obtained. For a specified rough road, parameter a has a certain definite value. It reflects the resonance in the spatial frequency domain.

For $\Omega_0 = \omega_0/V$, where ω_0 is the natural frequency of the vehicle system, we note that Ω_0 is related to V, vehicle speed. In general, ω_0 is around 1 Hz for passenger vehicles. As V increases from 0, Ω_0 decreases from ∞. At speed $V = 100$ km/h (27.78 m/s), Ω_0 is $= 1/27.78$ (cycle/m), or the wavelength is 27.78 m/cycle. This

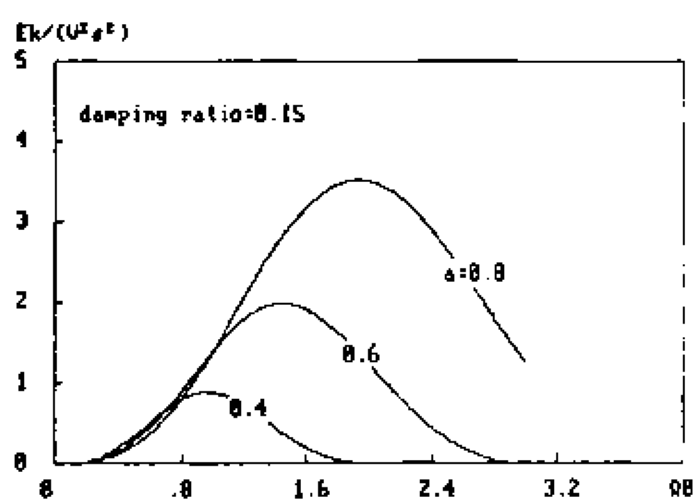

FIG. 6. Kinetic energy E_k vs Ω_0 at $\xi = 0.15$

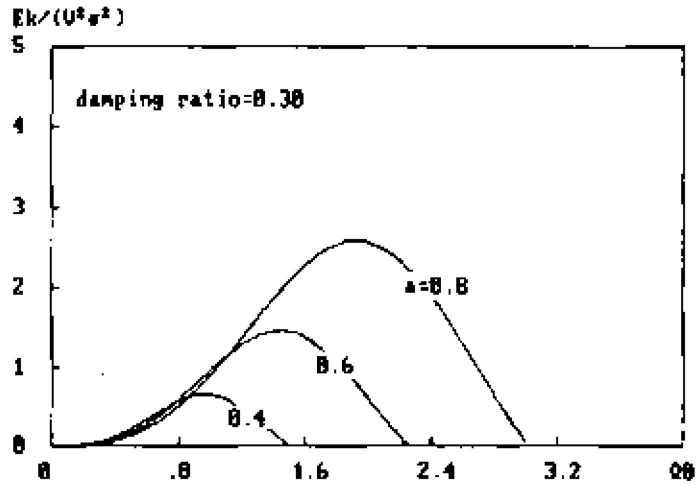

Fig. 7. Kinetic energy E_k vs Ω_0 at $\xi = 0.30$.

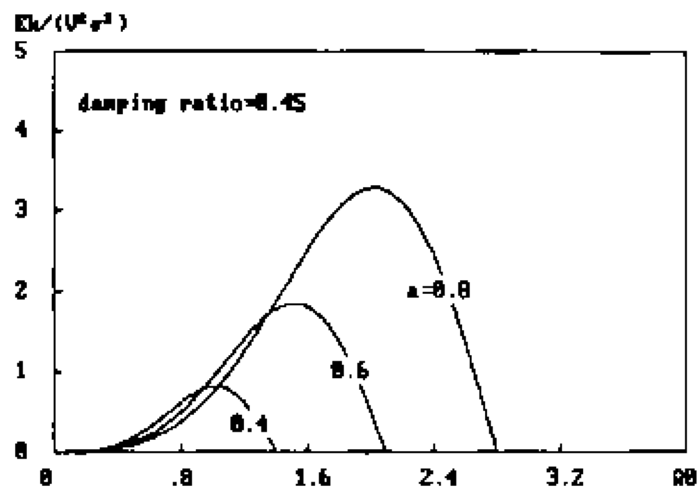

Fig. 8. Kinetic energy E_k vs Ω_0 at $\xi = 0.45$.

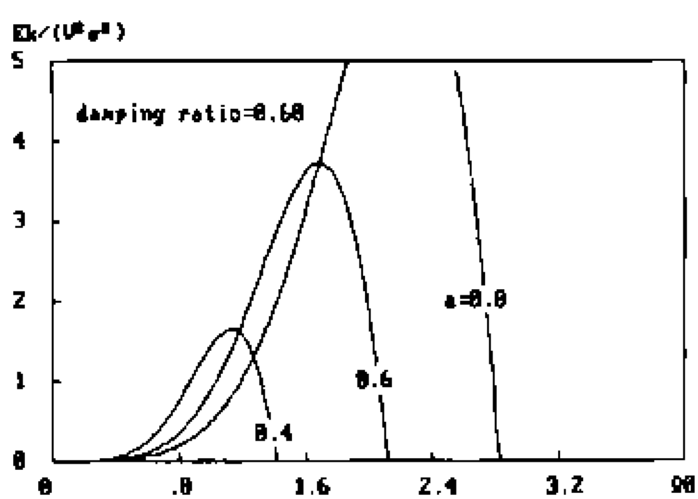

Fig. 9. Kinetic energy E_k vs Ω_0 at $\xi = 0.60$.

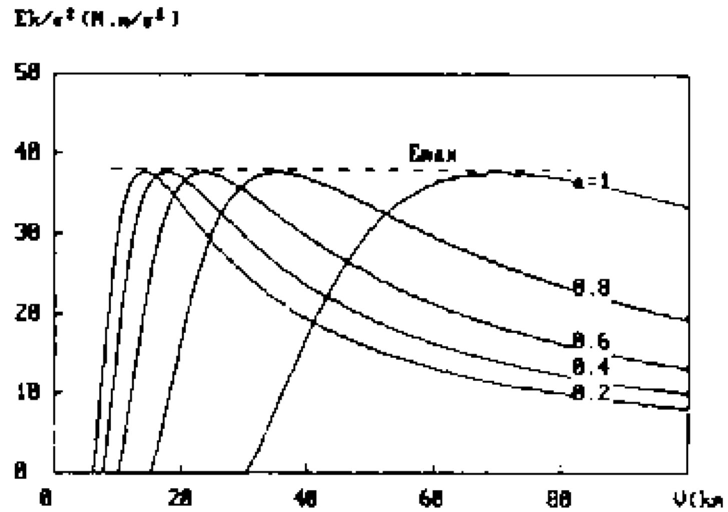

FIG. 10. Kinetic energy E_k vs speed V.

highlights a commonly recognized important conclusion, i.e. that the long wavelengths of a rough road surface higher than a limit around 50 m are of marginal effect.

The relationship between E_k and V is shown in Fig. 10, where ω_0 is taken as 1 Hz ($= 1$ cycle/s $= 2\pi$ rad/s) while parameter a has five values 0.2, 0.4, 0.6, 0.8 and 1. From the figure, we observe:

(1) The peak value of E_k for any value of a appears to be a constant for the same vehicle system with the same primary natural frequency ω_0 and damping ratio ξ. This can be approximately shown as (see Appendix B):

$$E_{k\max} \approx 0.19004\ \omega_0^2\sigma^2\{[1 + 4\xi^2]/[\xi\sqrt{(1-\xi^2)}\sqrt{(1-2\xi^2)}]\}. \tag{29}$$

The peak value appears approximately at $V = \omega_0\sqrt{\cos\theta}/(\sqrt{2a})$. E_k is not monotonically increasing with V, but decreases after this speed.

(2) For a big a value, the peak E_k value appears at an earlier speed V.

$(E_k)_{\max}$ can be used as an indicative parameter for road classification, inasmuch as it represents the maximum kinetic energy of a unit vehicle mass in motion over a rough road surface.

To evaluate the absorbed power for the human body (driver or passenger), we have to investigate how the energy is absorbed in unit time by the human body. When the vehicle mass vibrates, the body receives the vertical motion through the connecting seat and seat belt. Since the human body is by no means a simple "structure", but a very complicated system which is neither homogeneous nor isotropic from a material viewpoint, some assumptions need to be introduced if a simple "model" treatment is to be provided.

To model the absorbed power (energy in unit time) P_a, we assume there is an average viscodamping coefficient C_b:

$$P_a = C_b E[(\mathrm{d}v/\mathrm{d}t)^2] \tag{30}$$

where E is the mathematical expectation. $C_b\ \mathrm{d}v/\mathrm{d}t$ is the damping force. $c_b\ \mathrm{d}v/\mathrm{d}t\ \mathrm{d}v$ is the work the vehicle body does to the human body (inversely the human body absorbed energy in time dt due to vibrational motion) and $C_b[dv/dt]^2$ is the power that the body absorbs. Hence, we obtain the average absorbed power as:

$$P_a = 2C_b E_k. \tag{31}$$

The value of C_b is taken as 300 Ns/m (see Ref. [8]). From equations (29) and (31), we have:

$$(P_a)_{max} = 2C_b(E_k)_{max} = 114.02[(1 + 4\xi^2)/\xi\sqrt{(1 - \xi^2)}\sqrt{(1 - 2\xi^2)}]\omega_0^2\sigma^2. \tag{32}$$

It is seen that the maximum human body absorbed power $(P_a)_{max}$ depends on:

(a) rough road height RMS value σ^2—from the external road condition;

(b) vehicle system characteristics—the primary natural frequency ω_0 and the damping ratio ξ.

Since it has been chosen that $\xi = 0.3$ is the optimum damping ratio (to be chosen), the significant factor is ω_0. If ω_0 increases, $(P_a)_{max}$ also increases, indicating thereby the effect of the primary natural frequency of the vehicle system. An increase in the mass of vehicle, or a soft suspension spring, or a decrease in the inflation pressure of tyre, will reduce the vibration energy level.

APPLICATIONS FOR ROAD CLASSIFICATION

(a) Method

To classify the road quality based on human body absorbed power P_a, it is reasoned that when P_a reaches six watts (= 0.612 kg m/s = 6.004 N m/s), the body is in distress, i.e. the road is unacceptable. Below 6 watts, the road surface characteristics can be sequentially graded as very poor, poor, satisfactory, good and very good. One therefore needs to find a way to distinguish the road grades according to a P_a value. The simplest way is to divide 6 watts into five intervals. In considering human body sensation in a non-linear fashion and "borrowing" from signal analysis, we divide road grades in the following way: if P_a is over 6 watts, the road is unacceptable; if P_a is within 3–6 watts, the road is very poor, where 3 watts is half of 6 watts; if P_a is between 1.5 and 3 watts, then road grade is poor; so on so forth. Since each grade reduces the P_a value in half from the previous value, this yields a linear decline in log units. The corresponding road grades are shown in Table 1. Furthermore, Road Quality Index (RQI) is defined as:

$$\begin{aligned} \text{RQI} &= (20/\log 2)\log(6\ (\text{watts})/P_a) \\ &= (20/\log 2)\log(6.004\ (\text{N m/s})/P_a). \end{aligned} \tag{33}$$

When P_a is 6 watts, RQI is 0; when P_a = 3 watts, RQI = 20; etc.

TABLE 1. ROAD GRADES AND RQI VALUES ACCORDING TO P_a VALUE

No.	P_a (watts)	RQI	Grade
1	> 6	< 0	unacceptable
2	3–6	0–20	very poor
3	1.5–3	20–40	poor
4	0.75–1.5	40–60	satisfactory
5	0.375–0.75	60–80	good
6	< 0.375	> 80	very good

In general, P_a is a function of a, σ, V and the vehicle system characteristic parameters ω_0 and ξ, as formulated in equation (25) and (31). This consideration includes too many parameters. Selecting $(P_a)_{max}$ in equation (32) as a representative value of P_a, we can use equations (32) and (33) for road classification. By using equations (32) and (33), we build a relationship between road quality index, RQI, and σ^2, the RMS value of road rough surface height, which is given by:

$$\mathrm{RQI} = (20/\log 2)\log\{6.004(\mathrm{N\,m/s})/[114.02(1+4\xi^2)/\xi\sqrt{(1-\xi^2)} \times \sqrt{(1-2\xi^2)}]\omega_0^2\sigma^2\}(\mathrm{Nm/s}). \tag{34}$$

This is an approximate formula. For $\xi = 0.3$ and $\omega_0 = 1$ Hz ($= 2\pi$ rad/s), we obtain $(E_k)_{max}$ from equation (29)—a neat analytical formula:

$$(E_k)_{max} = 39.37\sigma^2\ (1/s^2) \tag{35}$$

and

$$\mathrm{RQI} = (20/\log 2)\log\{6.004/(598.4\sigma^2)\}. \tag{36}$$

As seen from Appendix B, formula (29) is approximate. In using a numerical program through more tedious calculation, a more accurate value $(E_k)_{max} = 38\ \sigma^2$ is obtained. The difference is within 3%, which is marginal.

Thus, $(P_a)_{max} = 2C_b(E_k)_{max} = 22800\ \ \sigma^2(\mathrm{Nm/s})$, where σ is in meters. For $(P_a)_{max} = 6$, 3, 1.5, 0.75, 0.375 watts, the corresponding values of σ are 0.0162, 0.0114, 0.0081, 0.0057, 0.0041 and 0.0028 m respectively. The RQI is given as:

$$\begin{aligned}\mathrm{RQI} &= (20/\log 2)\log\{6.002/[22800\sigma^2]\}\\ &= -238 - 57.7\log\sigma.\end{aligned} \tag{37}$$

The proposed method for road classification is solely dependent on the value of σ. The relationship between the RQI and σ is shown in Fig. 11.

The RMS value σ of the rough road surface is the root mean square value of the road surface height viewed from a vehicle mass centre. This is because a one-degree system has been used to model the vehicle system. Disregarding the fact that the vehicle system is a multi-degree system, which includes pitch angle motion, the

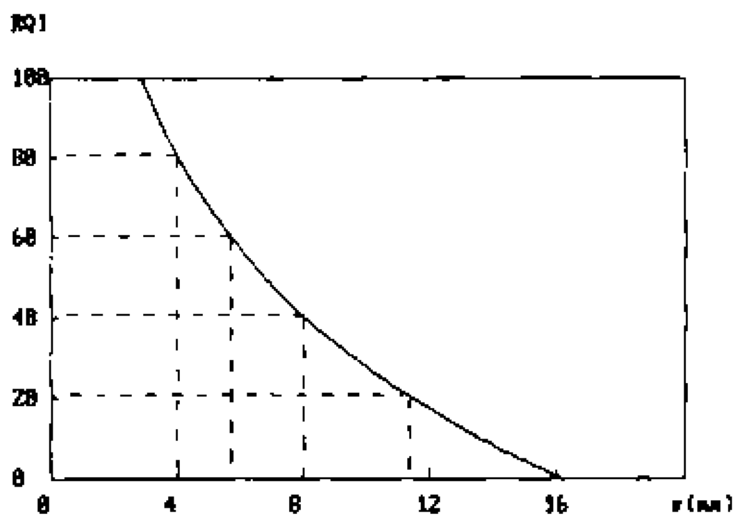

Fig. 11 Road Quality Index (RQI) vs RMS value of rough road height, σ.

reference line to measure the rough surface height is the line connecting the centres of the front wheel and rear wheels.

(b) Laboratory tests

Laboratory tests for road roughness classification were performed in the Geotechnical Research Centre of McGill University. Four rough non-deformable surfaces were used as test surfaces: (a) flat and smooth surface; (b) rough 1; (c) rough 2; (d) rough and sinusoidal. The ultrasonic wave apparatus (called ultrasonic distance detector) was used to measure the rough surface profile amplitude. It was pre-calibrated to convert the distance data into electronic voltage. The relationship between voltage and distance is very linear.

In the tests reported by Eiyo [9] the measured profile data were continuously recorded on a magnetic tape and the FFT (Fast Fourier Transform) was used to calculate the PSD of each profile. The sampling interval is chosen to be 3.5 mm and the number of data points was 1024. Because of the limitation of profile surface length (about 5 m) in the laboratory, the low frequency component was not expected to be accurate. The measured original profiles were calculated to obtain PSD curves, and subsequently classified according to the ISO method.

According to the developed model, the RQI method is used to classify the surface condition. The results are compared with the ISO method, and are shown in Table 2. This demonstrates the application of the RQI method. The rating is similar to that using the ISO method. However, there is a major difference between them—the simplicity. In using the ISO method, a lot of data treatment jobs need to be done: FFT (Fast Fourier Transform) to obtain PSD (Power Spectral Density) etc. In using the present RQI method, only σ—the RMS (root mean square) value of the road profile—is needed. It is not only very easily understood by the road service technicians (compared with the concept of PSD), but also involves much less time for the data treatment process.

SUMMARY AND CONCLUSIONS

Road classification deals with a road roughness stochastic process. The interaction between the vehicle dynamical system and the rough road surface profile determines the ride quality.

In the present investigation on road classification, the PSD method is adopted. The autocorrelation function for the road roughness random process is described in an analytical form which involves two basic parameters: σ and a. Subsequently the power spectral densities for road roughness profile and the responses of vehicle

TABLE 2. RQI VALUES FOR FOUR SURFACE PROFILE

Case	σ(m)	RQI ($10^{-6}m^3$/cycle)	Road class	
			RQI	ISO
(a)	0.0022	> 100	very good	very good
(b)	0.0045	74	good	good
(c)	0.0085	37	satisfactory	satisfactory
(d)	0.0144	6.7	very poor	very poor

system, the vibration energy, the human absorbed power and the vibration level are formulated.

In regard to road classification, the principle of human body absorbed power is used to set the standard for judgment of the road conditions. A RQI (road quality index) is also defined. It is shown that the RMS value σ is the most significant value for road classification.

Acknowledgments—The authors wish to thank Dr Fumiharu Eiyo, Dr A. M. O. Mohamed and Mr F. Caporuscio for their assistance. We would like to extend our gratitude to Dr M. Pehlivanidis and Mr B. Petitclerc (Ministry of Transport of the Government of Quebec) for their generous support.

REFERENCES

[1] S. Michel, *Pavements and Surfacings for Highways and Airports*. Halsted Press (1975).
[2] R. G. Hennes, *Fundamentals of Transportation for Engineering*. Second Edition. McGraw-Hill, New York (1969).
[3] A. A. Butkunas, Power spectral density and ride evaluation. *SAE Trans* 75, Paper 660138 (1967).
[4] W. E. Thompson, Measurements and Power Spectra of Runaway Roughness at Airports in Countries of North Atlantic Treaty Organization. NACA TN 4303 (1958).
[5] ISO/TC108/SC2/WG4 N57, Reporting Vertical Road Surface Irregularities (1982).
[6] ISO 2631, Guide for the Evaluation of Human Response to Whole-body Vibration (1974, 1978, 1982).
[7] D. A. Crolla, Off-road vehicle dynamics. *Vehicle System Dynamics*, Vol. 10, pp. 253–266 (1981).
[8] C. C. Daniel, Revised Vehicle Dynamics Module: User's Guide for Computer Program VEHDYN II, US Army Engineering Waterways Experiment Station, Structures Laboratory, 39180-0631 (1986).
[9] Fumiharu Eiyo, Effect of Off-Road Surface Roughness on Tyre Performance, Ph.D. Thesis, McGill University (1989).

APPENDIX A (E_k *integral*)

E_k is given by equation (24). Let

$$\alpha = \Omega/\Omega_0 \quad \text{(A.1)}$$

thus,

$$d\Omega = \Omega_0\, d\alpha. \quad \text{(A.2)}$$

The integral of equation (24) is given as:

$$E_k = [V^2\sigma^2\Omega_0^3/(4a\sqrt{\pi})]J \quad \text{(A.3)}$$

and

$$J = \int_{-\infty}^{\infty} \alpha^2 \exp\{[-\Omega_0^2/(4a^2)]\alpha^2\} \frac{[1 + 4\xi^2\alpha^2]}{[(1-\alpha^2)^2 + 4\xi^2\alpha^2]}\, d\alpha. \quad \text{(A.4)}$$

The term $\Omega_0^2/(4a^2)$ is usually small. Hence integrals are dominated by the poles. To carry on with integration of J, the Residue Theorem is used:

$$J = 2\pi i \Sigma \text{ residues of } z^2 \exp\{[-\Omega_0^2/(4a^2)]z^2\}[1 + 4\xi^2 z^2]/[(z^2-1)^2 + 4\xi^2 z^2]$$

$$\text{(over the upper half } z \text{ plane)} \quad \text{(A.5)}$$

where z is a complex variable.

Poles are obtained from:

$$(z^2 - 1)^2 + 4\xi^2 z^2 = 0. \quad \text{(A.6)}$$

There are four poles, named $z1$, $z2$, $z3$ and $z4$, and they are given by:

$$z1 = \exp[(\theta/2)i] \quad \text{(A.7a)}$$

$$z2 = \exp[-(\theta/2)i] \quad \text{(A.7b)}$$

$$z3 = -\exp[-(\theta/2)i] \quad \text{(A.7c)}$$

and

$$z4 = -\exp[(\theta/2)i] \tag{A.7d}$$

where

$$\theta/2 = \arctan[\xi/\sqrt{(1-\xi^2)}] \tag{A.8}$$

or

$$\theta = \arctan[2\xi\sqrt{(1-\xi^2)}/(1-2\xi^2)]. \tag{A.9}$$

$z1$ is conjugate with $z2$, so is $z3$ with $z4$. Over the top half z plane, the residues are with respect to the poles $z1$ and $z3$, but not $z2$ and $z4$, since they are in the lower half z plane.

$$\begin{aligned}\text{Residue 1} = {} & \exp[(\theta/2)i]\exp\{[-\Omega_0^2/(4a^2)]\exp(\theta i)\}\\ & \times[1+4\xi^2\exp(\theta i)]/[8i\xi\sqrt{(1-\xi^2)}]\end{aligned} \tag{A.10}$$

and

$$\begin{aligned}\text{Residue 2} = {} & \exp[-(\theta/2)i]\exp\{[-\Omega_0^2/(4a^2)]\exp(-\theta i)\}\\ & \times[1+4\xi^2\exp(-\theta i)]/[8i\xi\sqrt{(1-\xi^2)}].\end{aligned} \tag{A.11}$$

Hence, E_k is given by:

$$\begin{aligned}E_k = {} & V^2\sigma^2\Omega_0^1\sqrt{\pi}/[16a\xi\sqrt{(1-\xi^2)}]\\ & \times\{\exp(\theta/2i)\exp[-\Omega_0^2/(4a^2)\exp(\theta i)]\\ & +\exp(-\theta/2i)\exp[-\Omega_0^2/(4a^2)\exp(-\theta i)]\}.\end{aligned} \tag{A.12}$$

By expanding and collecting terms, this can be expressed as:

$$\begin{aligned}E_k = {} & V^2\sigma^2\Omega_0^1\sqrt{\pi}/[8a\xi\sqrt{(1-\xi^2)}]\exp[-\Omega_0^2/(4a^2)\cos\theta]\\ & \times\{\cos[\Omega_0^2/(4a^2)\sin\theta-\theta/2]+4\xi^2\cos[\Omega_0^2/(4a^2)\sin\theta-3\theta/2]\}\\ & (\text{for } \Omega_0/(2a)<1).\end{aligned} \tag{A.13}$$

The terms in the imaginary part cancel out each other.

Letting

$$c_1 = \xi\sqrt{(1-\xi^2)} \tag{A.14}$$

and

$$B = \Omega_0/(2a) \tag{A.15}$$

we will obtain:

$$\begin{aligned}E_k = {} & [V^2\sigma^2a^2\sqrt{\pi}/c_1]B^1\exp[-B^2\cos\theta]\\ & \times\{\cos[B^2\sin\theta-\theta/2]+4\xi^2\cos[B^2\sin\theta-3\theta/2]\}\\ & (\text{for } B<1).\end{aligned} \tag{A.16}$$

This is formula (25) in the main body of the paper

APPENDIX B

The condition to find the maximum value of E_k with respect to different a values is:

$$\mathrm{d}(E_k)/\mathrm{d}a = 0. \tag{B.1}$$

From equation (A.13) in Appendix A, E_k is given approximately as

$$E_k \approx [V^2\sigma^2\sqrt{\pi}/8][(1+4\xi^2)/c_1]\exp\{-[\Omega_0/(2a)]^2\cos\theta\}/a. \tag{B.2}$$

In using condition (B.1), one obtains.

$$-1/a^2+(1/a^4)(\Omega_0^2\cos\theta)/2=0$$

or

$$a^2 = \Omega_0^2 \cos\theta/2 \tag{B.3}$$

or

$$a = \Omega_0 \sqrt{\cos\theta}/\sqrt{2}. \tag{B.4}$$

Returning this value back into (B.2), we have:

$$\begin{aligned}(E_t)_{max} &\approx [\sqrt{\pi}/(4\sqrt{2})][\exp(-0.5)][V^2\sigma^2\Omega_0^3][1 + 4\xi^2]/[c_1(\cos\theta)] \\ &\approx 0.19004\,(1 + 4\xi^2)[\omega_0^3\sigma^2]/(c_1\sqrt{\cos\theta}) \\ &= 0.19004\omega_0^3\sigma^2\{[1 + 4\xi^2]/[\xi\sqrt{(1 - \xi^2)}\sqrt{(1 - 2\xi^2)}]\}.\end{aligned} \tag{B.5}$$

International Society for Terrain-Vehicle Systems
Proceedings of the 4th Regional North American Meeting
Sacramento, CA, March 25-27, 1992

DEVELOPMENT OF CRITERION FOR ROAD SURFACE ROUGHNESS BASED ON POWER SPECTRAL DENSITY FUNCTION

D.M. XU[1], A.M.O. Mohamed[1], R.N. Yong[1], and F. Caporuscio[1]

ABSTRACT

The study has demonstrated that non contact acoustical transducer is a reasonable sensor for reflecting the road roughness profile, and it is much faster in detecting the road surface roughness as compared to other measurement devices. Thus, it s a very promising sensor with regard to road roughness measurement. Furthermore, the ISO may be used to classify the road grade. However, the assumed linearity in the PSD on a log-log graphical representation may not be true in reality, especially in the lower frequency band. Therefore, a new approach to classify the road surface roughness is to be developed.

INTRODUCTION

When a vehicle is operated on an uneven road surface, ride quality diminishes and factors such as vehicle vibration, fatigue of vehicle frame and changes in vehicle traction induced by excitation from the ground surface, and contribute to unsafe driving conditions. Other problems arising from vehicle-road interaction concern dynamic loading of the road. The greater the roughness of the road surface, the more intense is the dynamic loading of the road. Deterioration of the pavement slab and subgrade can be accelerated because of dynamic loading from the vehicle, thus increasing the frequency of repair.

A critical issue is the ability to determine a preventive maintenance schedule to avoid catastrophic deterioration and dangerous consequences. The question of effect of road surface roughness on accelerated road deterioration needs to be answered. To evaluate the repair time and plan a schedule of road maintenance, as well as to set an acceptance criterion for newly paved roads, it is necessary to first obtain a correct road surface profile.

For the measurement of the road surface height profile and roughness, many methods have been employed, or are currently still being used, depending on the objectives. They are classified as the conventional method, profilometer method, servoseismic method,slope integration method and fifth wheel method. However, these methods are generally tedious, or need relatively large data processing capability. In addition the measured data by contact methods, excluding the conventional method, may be somewhat distorted because of the enveloping effect of the contact development with the ground surface. To avoid this, a methodology and non-contact acoustical transduce are required to accurately measure the road profile, and to perform quick processing of the road profile information.

[1] Geotechnical Research Centre, McGill University, 817 Sherbrooke St. West, Montreal, Quebec, Canada H3A 2K6

This study is designed to: (1) use a noncontact acoustical transducer to measure surface profile and roughness in the laboratory on manufactured rough road surfaces as well as in the field on actual rough road surfaces; (2) use the power spectral density function (PSD) to evaluate and classify road surface roughness, and (3) develop a correlation between (1) and (2) using PSD along the lines of the ISO classification.

SURFACE ROUGHNESS CHARACTERIZATION

In the early studies of vehicle performance on a rough road, simple function such as sine waves, step function or triangular waves were generally applied as disturbances from the ground. While these inputs provide a basic idea for comparative evaluation of designs, it is recognized that the road surface is usually not represented by these simplified functions, and therefore, the deterministic irregular shapes cannot serve as a valid basis or studying the actual behaviour of the vehicle. In this study, a real road surface, taken as a random exciting function, is used as an input to a ride-road system. Since the main factors in a loading function are frequency and amplitude, the geometrical characteristics of a non-deformable terrain need to be described by these two quantities. The excitation frequencies are directly related to vehicle translational speed and the wavelengths contained in various waveforms of the rough surface profile. This illustrates the problem of the expression of roughness, i.e., randomness of surface profile.

It may be noted that the main characteristic of a random function is uncertainty. That is, there is not way to predict an exact value at a future time. The function must be described in terms of probability statements as statistical averages, rather than by explicit equations. Four main methods can be used to describe the basic properties of random data: 1) root mean square values; (2) probability density function; (3) auto correlation function, and (4) power spectral density function. In this study emphasis will be given to power spectral density analysis.

POWER SPECTRAL DENSITY FUNCTION

The power spectral density (PSD) function for a stationary record represents the rate of change of mean values with frequency. It is estimated by computing the mean square value in a narrow frequency band at various centre frequencies, and then dividing by the frequency band. The total area under the PSD curve over all frequencies will be the total mean surface value of the record. The partial area under the PSD curve from frequency f_1, to f_2 represents the mean energy value of the record associated with that frequency range.

The autocorrelation function and the PSD function are Fourier transforms of each other (Wiener-Khinchine relation), and therefore furnish similar information in the time domain and frequency domain, respectively. Most importantly, the PSD function may satisfy the requirements of road vehicle studies since both amplitudes and frequencies, which are essential factors for vehicle vibration dynamics, a described in terms of energy density. Thus it may be suitable to express the road surface profile (representantion of surface roughness) by a spectral description such as the PSD function. The PSD function will contribute to a response analysis which will describe, with adequate precision, the motion of the system expressed in most of displacement, acceleration or stress.

Since the terrain surface roughness under consideration is a spatial disturbance, rather than a disturbance in time, it is desirable to define the PSD in terms of the spatial frequency, Ω, in cycles per meter, rather than in terms of the conventional time frequency, f, in cycles per second. Spatial frequency is another description of frequency in the space domain. Then road surface roughness can be expressed in a concrete manner, disregarding the effect of various operating speeds of the vehicle. In terms of the spatial frequency argument, the PSD of the road surface is defined in the following manner [1]

$$S_y(\Omega)=\lim_{X\to\infty}\frac{2}{X}\left|\int_0^X y(x)e^{-2i\pi\Omega x}dx\right|^2 \tag{1}$$

where: $S_y(\Omega)$ = on sided PSD of the road surface file,(m^3/c); Ω = spatial frequency (c/m); X = length of course (m); x = horizontal distance over surface (m); and y(x) = surface height profile from a reference plane (m)

CLASSIFICATION OF ROAD SURFACE ROUGHNESS

Several attempts have been made to classify the roughness of a road surface. In this study, classification based on the International Organization for Standardization (ISO) is used. The ISO has proposed road roughness classification(Classes A to H) using the PSD values, Figure 1 shows the classification by ISO [2] and the corresponding range of PSD values at a frequency of $\frac{1}{2\pi}$ c/m. It is observed that the smoother surface possesses less power over a whole frequency range than the rougher surfaces. In the ISO proposal, the amplitude of PSD function of the road surface can be approximated by means of two straight lines with different slopes, since the PSD curves of many road surface show concavity. The approximate forms of smoothed PSD's (one sided) are given as follows:

$$\begin{aligned} S_y(\Omega)&=S_y(\Omega_o)\left(\frac{\Omega}{\Omega_o}\right)^{-n_1} \quad for \ \Omega\le\Omega_o=\frac{1}{2\pi}c/m \\ S_y(\Omega)&=S_y(\Omega_o)\left(\frac{\Omega}{\Omega_o}\right)^{-n_2} \quad for \ \Omega>\Omega_o \end{aligned} \tag{2}$$

where: n_1 and n_2 are 2.0 and 1.5, respectively, in the ISO draft. These two values are determined from filed measurements. A more simplified mathematical form is suggested as follows [3].

$$S_y(\Omega)=G_o\Omega^{-n} \tag{3}$$

Where: G_o and n are positive constants.

Eq. 3 represents a linear relationship between log $S_y(\Omega)$ and log Ω, which can be seen if the log operation is applied to both sides of the equation. However, Eq. 3 is questionable for the following reasoning. It is known that the inverse Fourier transform of $S_y(\Omega)$ gives the auto correlation function as:

$$\begin{aligned} R(\mu) &= \frac{1}{2}\int_{-\infty}^{\infty} S_y(\Omega) e^{2i\pi\Omega\mu} d\Omega \\ &= \int_0^{\infty} S_y(\Omega) \cos 2\pi\Omega\mu \; d\Omega \end{aligned} \tag{4}$$

Let $\mu = 0$, the Eq. 4 is reduced to:

$$R(0) = \int_0^{\infty} S_y(\Omega) d\Omega \tag{5}$$

$S_y(\Omega)$ has the following three properties: (1) $S_y(\Omega)$ is positive definite; (2) $S_y(\Omega) \to 0$ *when* $\Omega \to \infty$, and (3) the area covered by the $S_y(\Omega)$ curve is equal to root mean square value, σ^2.

Substituting Eq. 3 into Eq. 5, one gets:

$$G_o \int_0^{\infty} \Omega^{-n} d\Omega = \frac{G_o}{-n+1} \Omega^{-n+1} \Big|_0^{\infty} = \frac{G_o}{n-1} \lim_{\Omega \; 0} \Omega^{-n+1} \tag{6}$$

Since n is generally around 2, the integration reaches $\infty\left(\frac{1}{0}\right)$, an infinite value of σ^2. The problem is noticeable at the low frequency band. It is known that the power spectral density is always an even function with respect to $\Omega = 0$, i.e., the left side is symmetric to the right. At $\Omega = 0$, the slope of the power spectral density function is always zero. Hence, the PSD shape is more likely to be flat at low frequencies in the vicinity of $\Omega = 0$. Results from Eyio and Yong [4], which were carried out at the Geotechnical Research Centre for four artificially made rough road surface height profiles, do not likely to support the ISO relation presented by Eq. 3.

MODEL DEVELOPMENT

Based on the properties of the autocorrelation function, $R(\mu)$, as well as the experimental data from Eyio and Yong [4], the following autocorrelation function is proposed:

$$R(\mu) = \sigma^2 \exp[-a^2\mu^2] \tag{7}$$

Eq. 7 has the following properties: (1) it is an even function; (2) R(0) is the root mean square value (σ^2), and (3) when $\mu \to \infty$, the function approaches zero. The autocorrelation function proposed by Eq. 7 involves two parameters 'σ' and 'a' which need to be determined.

The physical meaning of parameter σ is rather simple. It denotes the statistical value for mean average rough road amplitude. This is an important quantity which species the road surface roughness. As the σ value increase, the road surface roughness increases proportionally. While, the physical meaning of parameter "a" is not as obvious. It is related to the wave shape of the rough road surface profile.

Based on the proposed autocorrelation function given by Eq. 7,the corresponding PSD, $S_y(\Omega)$, is obtained by:

$$S_y(\Omega)=\frac{\sigma^2}{2a\sqrt{\pi}}\ \exp[-\Omega^2/(4a^2)] \tag{8}$$

It can be seen from Eq. 8 that "a" is small, the term $\exp\left(\frac{-\Omega^2}{4a^2}\right)$ decreases rapidly with Ω, indicating a narrow frequency band.

EXPERIMENTATION

The primary components of the road roughness measurement system are an acoustical transducer and a ranging circuit board. Together these units are capable of detecting and measuring the distance of objects (surfaces) within a range of approximately 275 mm to 427 mm. During operation, a pulse is transmitted toward a target and the resulting echo is received. The elapsed time between the initial transmission and the echo detection is then converted to distance with respect to sound. The principal component is the acoustical transducer, which acts both as a loudspeaker and a microphone. The polaroid transducer was designed to transmit the outgoing signal and also function as an electrostatic microphone in order to receive the reflected signal (the echo).

When the unit is activated, the transducer emits a sound pulse, then waits to receive the echo. The emitted pulse is a high-frequency, inaudible "chirp", lasting approximately one millisecond and consisting of fifty-six pulses. After generating the "chirp", the operating mode of the transducer changes from loudspeaker to microcomponent detect the returning echo. The transducer then converts the echo sound energy to electrical energy, which is amplified by the analog circuit, and then detected by the digital circuit to produce the echo received signal. The received signal is then fed to a distance to voltage converter and, subsequently, the recording system.

During the 1990 field testing program, the acoustical transducer was mounted on the rear axle (on the drive side) with a special "U" type mount. The transduce was positioned 305 mm above the pavement. All the required electronics, plus the AC power for the data recording system, were installed in a van. The van was driven over a specified areas at a speed of 6-7 km/h. The data was recorded both on a trip chart recorder and a magnetic tape machine. The magnetic tape was then converted from analog to digital, copied onto floppy diskettes, and then input into a personal computer for data reduction.

RESULTS AND DISCUSSION

The road section (piste) number and the corresponding location of the tested road sections are shown in Table 1. The length of each road section was 300 m. In comparison with laboratory test conducted by Eyio and Yong [4], field test were representative of the real situation in terms of the length of each road section, as well as the surface roughness. It should be noted that for field conditions the minimum spatial frequency is 0.0033 cycle/m (for each 300 m length), while for the laboratory test the minimum frequency was 0.25 cycle/m (for each 4 m length). Therefore, field conditions provide more input in relation to the dynamic behaviour in the lower frequency range.

In considering the fact that there might be different road roughness within the 300 m section, the PSD calculations were carried out for a window length of 50 m. The choice of 50 m as the basic length is attributed to the following reasons. First of all the lowest spatial frequency is 0.02 cycle/m, which is quite small compared with the specific spatial frequency (0.16 cycle /m) used in the ISO method. Therefore, it will provide a more accurate PSD value at a specific special frequency. The second reason is related to practical considerations. For road reparation, a distance of 50 m is considered to be an adequate length. Therefore, for each piste, one has 5 basic lengths, which are: (a) from 0-50m; (b) from 5-100 m; (c) from 100-150 m; (d) from 150-100m; (e) from 200-250 m, and (f) from 250-300m.

Due to a similarity in data analysis, piste number 13 is only presented in order to illustrate the roughness condition, as well as the method of classification. Figure 2 shows the measured road surface roughness profiles for 0-300 m for the 50 m subsections, whilst Figure 3 shows the calculated PSD curves for piste number 13. According to the ISO method of classification (i.e. at spatial frequency 0.16 cycle/m), the road is classified as good for all subsections (a) to (f).

Table 2 summarizes the road classifications for all 10 pistes according to: (1) PSD evaluation; (2) International Roughness Index (IRI), and (3) Emperical Rolling Coefficient (KR). It can be concluded from Table 2 that all road section are in good service condition. However, the worst subsections are: (a) piste 7, section (f) - i.e. , from 250-300 m and (b) piste 28, sections (a) and (b) - i.e. from 0-100 m. These subsections are graded average according to the ISO method of classification. However, they are still in fair service condition at the present time.

CONCLUSION

The salient features covered in this study may be concluded as follows:

(1) the acoustical transducer is a reasonable sensor for reflecting the road roughness profile, and it is much faster in detecting the road surface roughness as compared to to other measurement devices. Thus, it is a very promising sensor with regard to road roughness measurement.

(2) the ISO method may be used to classify the road grade. The assumed linearity in the PSD on a log-log graphical representation may not be true in reality, especially in the lower frequency band.

(3) the proposed PSD function is governed by only two parameters: (1) parameter "a" which are directly related to the wave shape of the rough road surface profile, and (2) parameter "σ" which denotes a statistical value or mean average rough road amplitude. The parameter σ is the most important parameter for characterizing a rough road surface profile. The dynamic response increases as σ increases.

ACKNOWLEDGEMENT

This study was financially supported by Quebec Ministry of Transport

REFERENCES

[1] Wendenborn, J.G. (1966). "The Irregularities of Farm Roads and Fields as Sources of Farm Vehicle Vibrations". J. Terramech. Vol. 3, No. 3, pp. 9-40.

[2] ISO/TC108/SC2/WG4 N57 (1982). "Reporting Vehicle Road Surface Irregularities".

[3] Crolla, D.A. (1981) "Of-road Vehicle Dynamics" Vehicle System Dynamics, Vol. 190, pp. 253-266.

[4] Eyio, F.and Yong, R.N. (1990). "Measurement of Road Surface Roughness by Ultrasonic Detector" Proc. 10th Int. Conf. of the ISTVS/Kobe, Japan/August 20-24, pp. 25-35.

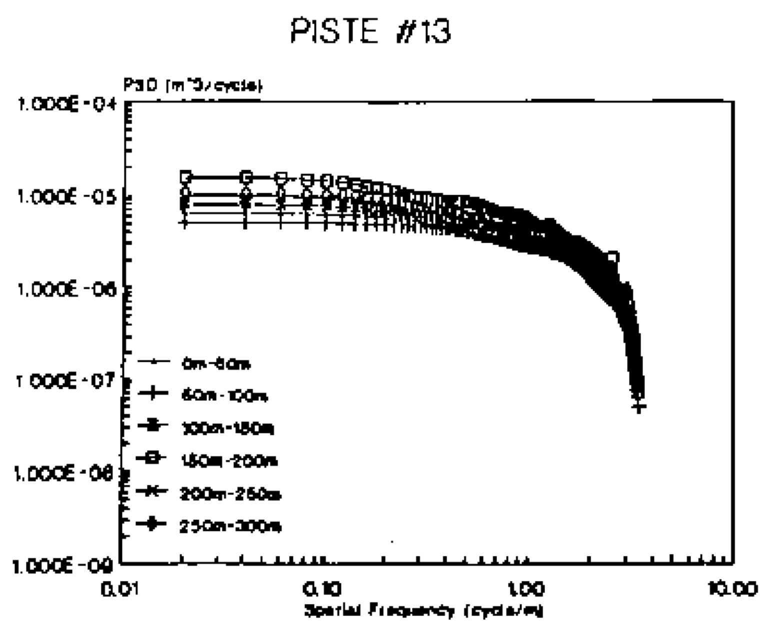

Fig. 3 Power Spectral Density - Spatial Frequency Relationships

Table 1 Road Sections* (Pistes) and Their Locations

Road Section (piste)	Location
3	Rte. 171-01-40 South
4	Rte. 171-01-40 North
7	Rte. St-Aimé (86380) South
13	Rte. 218-02-110 West
28	Rte. St-Aimé (86380) North
29	Rte. 86530 East
35	Rte. St-Aimé (86380) South
36	Rte. St-Aimé (86380) North
37	Rte. 171-01-50 North
38	Rte. 218-02-102 West

Table 2 Road Classifications

Method	PSD evaluation						IRI*	KR *
Sections / Piste #	(a) 0-50 m	(b) 50-100 m	(c) 100-150 m	(d) 150-200 m	(e) 200-250 m	(f) 250-300 m		
13	good	good	good	good	good	good	3.55	65
3	very good	excellent	excellent	excellent	excellent	excellent	1.28	95
4	excellent	excellent	very good	good	excellent	excellent	1.07	99
7	good	good	good	good	good	average	6.82	43
28	average	average	good	good	good	good	8.57	49
29	very good	very good	good	very good	excellent	very good	2.26	85
35	good	very good	very good	very good	good	very good	1.99	82
36	excellent	good	good	good	good	good	5.69	65
37	very good	good	excellent	excellent	very good	very good	1.78	86
38	good	very good	good	good	very good	good	2.97	56

* values provided by Ministry of Transport

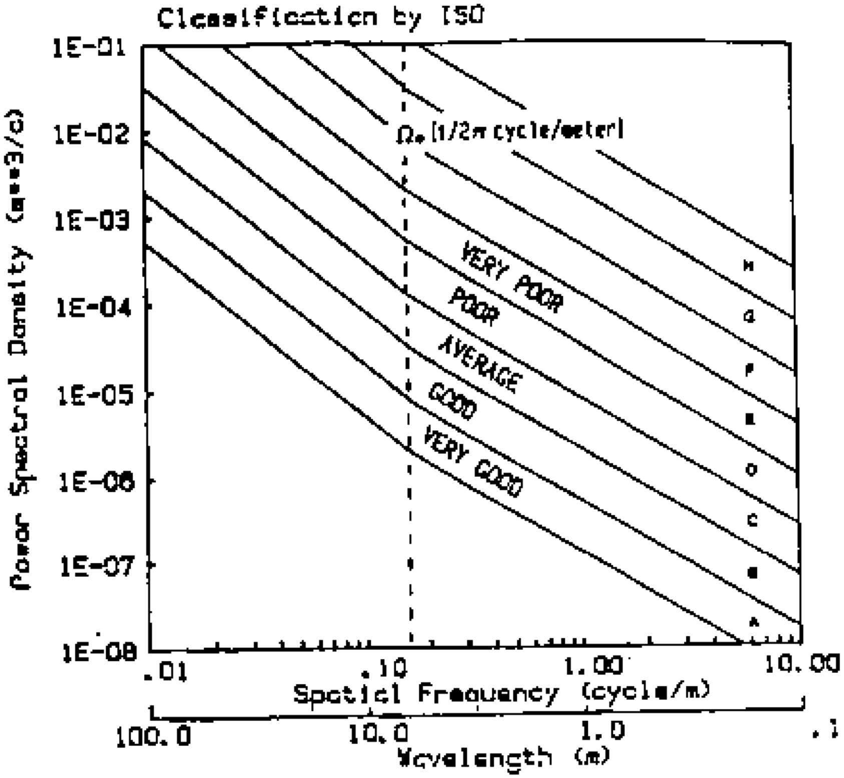

Road Class	Degree of Roughness $S(\Omega_0)$ 1E-6	
	Range	Geometric mean
A (Very Good)	< 8	4
B (Good)	8-32	16
C (Average)	32-128	64
D (Poor)	128-512	256
E (Very Poor)	512-2048	1024
F	2048-8192	4096
G	8192-32768	16384
H	32768 <	

Fig. 1 Road Roughness Classification by ISO

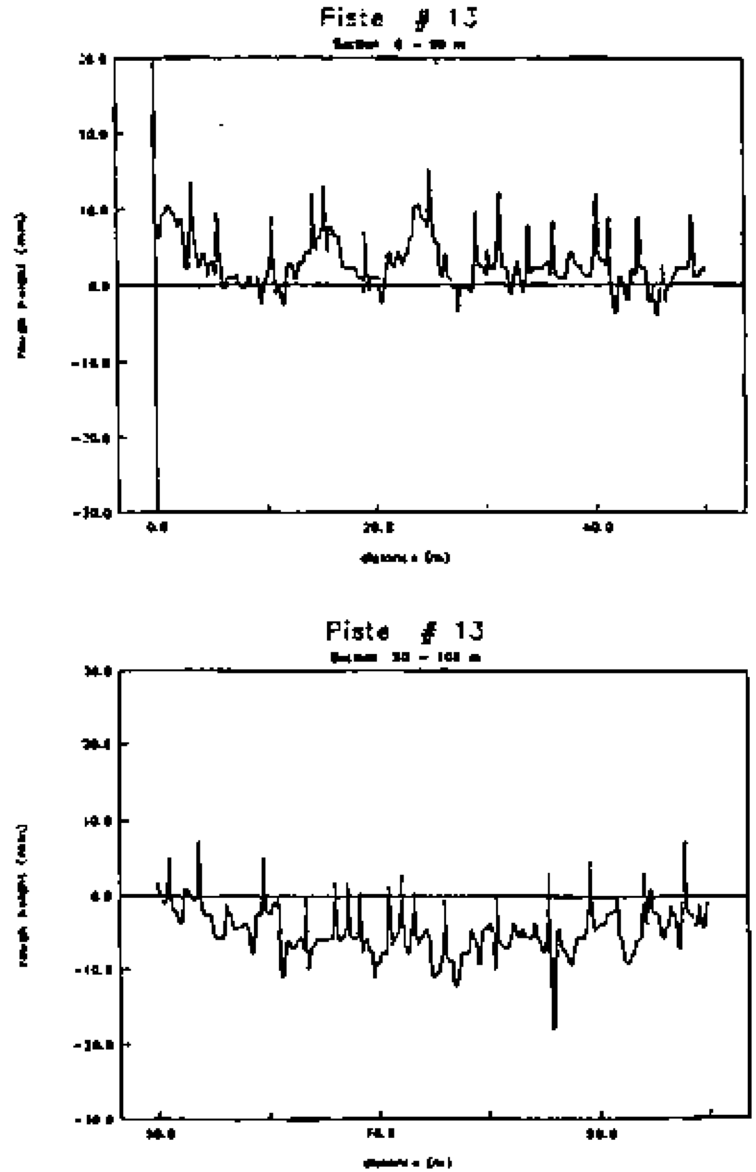

Fig. 2 Measured Road Surface Profiles

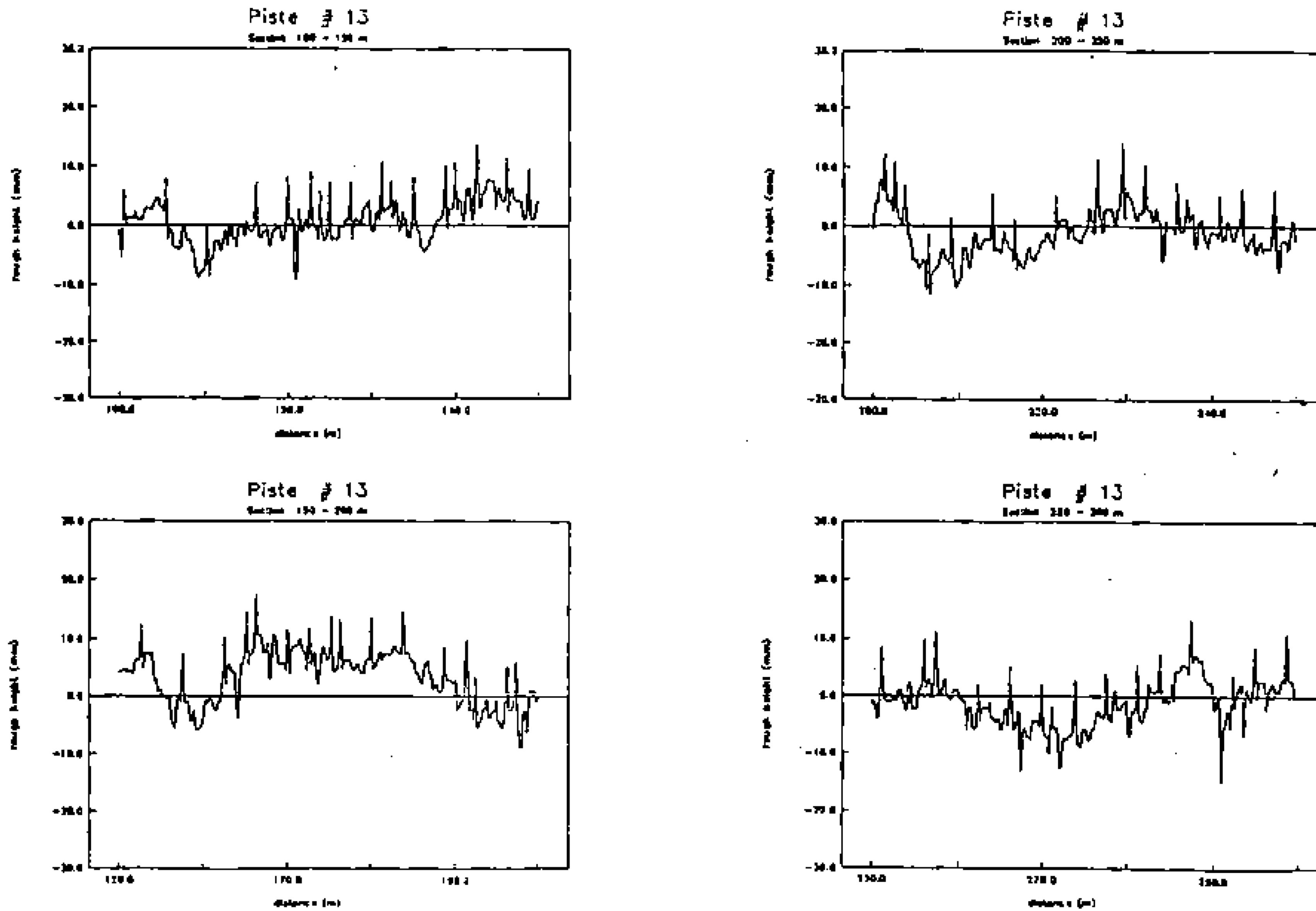

Fig. 2 Measured Road Surface Profiles (cont.)

Journal of Terramechanics, Vol. 30, No. 4, pp. 219–257, 1993.
Printed in Great Britain.

0022–4898/93 $6.00+0.00
Pergamon Press Ltd

EVALUATION OF THE PERFORMANCE OF DEEP SNOWPACK UNDER COMPRESSION LOADING USING FINITE ELEMENT ANALYSIS

A. M. O. MOHAMED, R. N. YONG and A. J. MURCIA*

Summary—The scope of this study extends to the development and validation of a computerized numerical model predicting the load–sinkage relationship of a rigid strip footing on deep snow. The creation of such a model focused on the volume change and shear characteristics of the material and their relationship to the overall behavior under plate loading conditions. It therefore become necessary to obtain information on the response of snow under the following conditions: (a) volume change only; (b) shear only, and (c) combination of both volume change and shear occurring simultaneously. The confined compression test was the obvious choice for investigating the volume change behavior or compressibility of the snow (condition a) whereas the direct shear test was selected to characterize the material response in pure shear (condition b). The rigid plate, or footing test, was performed in order to assess the validity of the model through a comparison of experimentally obtained curves and those predicted by the computer model based on the properties of the snow material in compression and shear. The validity of the proposed model is verified through a comparison of predicted and experimentally obtained results. Most results obtained from the finite element model are found to be in reasonably good agreement with the experimental data while some discrepancies are found to exist between specific types of results.

INTRODUCTION

THE MECHANICS of snow formation and precipitation is a complex subject involving many factors and is governed by the laws of physics, chemistry, thermodynamics as well as by meteorological conditions. In general, snow precipitation occurs provided sufficient atmospheric moisture is present in the air and that the climatic environment is suitable to initiate and maintain the mechanism by which this moisture is converted into snowfall. Condensation of water vapor in the atmosphere results in the formation of a cloud within which, provided the temperature drops below freezing, droplets join to generate ice crystals. Continued growth of an ice crystal leads to the formation of a snow crystal, which is a particle sufficiently large to be visible to the naked eye. A snowflake is produced as a result of aggregation of several hundreds of snow crystals. Snowflake sizes vary from a fraction of a millimeter to several centimeters. Normally, larger snowflakes are generated when the ambient temperature is near 0 °C and size decreases with decreasing temperature [1].

The accumulation of snowflakes on the ground leads to the generation of the snow-cover. Evidently, characteristics of the snow-cover, such as crystalline structure and density, are highly controlled by the type of weather during precipitation (i.e. temperature, wind speed, humidity, etc.) and are likely to change with time according

*Geotechnical Research Centre, McGill University, 817 Sherbrooke St. West, Montreal, Quebec, Canada H3A 2K6

to the meteorological conditions prevailing after deposition. Properties of the snow-cover such as strength, stiffness and density are of particular interest to transportation engineers concerned with travel over snow in northern countries. Transportation of supplies and goods to remote communities, mines, construction sites, etc. is heavily dependent on the efficiency of over-snow vehicles. Proper design of such vehicles requires not only a sound mechanical engineering basis but adequate understanding of the response of snow under loading. Since engineering design essentially and inevitably involves a mathematical idealization of the real problem at hand, the problem of describing the behavior of snow under loading arises.

Various subjects on snow mechanics have been studied over the years in order to develop a methodology to analyse and predict the stability of a snow mass and its response when subjected to external loading. Respective examples are avalanche prediction, which has been studied by Perla and Martinelli [2] and Fraser [3], and over-snow travel problems for which Harrison [4], Yong [5] and Brown [6] have proposed approaches and solution techniques. Strength analyses of snow are difficult because of the nature of the material at hand but a theoretical evaluation has been proposed by Ballard and McGaw [7].

The analytical prediction of the load--penetration curve of a rigid footing on snow is a complex problem involving a series of stress analyses of a highly compressible material under a given set of boundary conditions. The determination of stresses and deformations within a mass of material is a highly statistically indeterminate problem, the solution of which requires satisfying the following conditions as dictated by basic mechanics of materials:

(1) equilibrium of the mass is maintained;

(2) compatibility of deformations (i.e. deformation field is continuous within the mass and is geometrically consistent with the imposed boundary conditions);

(3) the constitutive relationship (or equations of material behavior) is respected at any point within the mass.

In so far as the material is assumed to be a continuum, the solution of the problem can be investigated through continuum mechanics. The classical theory of linear elasticity constitutes a powerful tool for solving many such problems. The method is purely analytical and consists in solving equations of stress with a particular set of boundary conditions. The above theory involves many assumptions regarding the behavior of the material under study. The most significant are:

(a) the material is isotropic and homogeneous;

(b) the material is linearly elastic;

(c) small strain theory applies;

(d) the deformation field is continuous such that no gaps or relative displacements between parts of the body occur.

The analytical solution of continuum mechanics problems is only possible for simple cases of loading and boundary conditions. The problem of determining the load–sinkage response of a footing in the type of deep snow considered in this study is already complicated by the presence of shear stresses along the sides of the pressure bulb generated by the plate penetration process. Moreover, the deformation field along the sides of the bulb is not continuous due to the differential vertical displacement of points on either side of the planes of shear. Assumption (d) above therefore automatically rules out the possibility of using classical elasticity as a solution procedure. The fact that the material is highly compressible and that large deformations occur during the plate penetration process also opposes assumption (c). In addition, snow is a non-linear material whose stiffness increases with volumetric strain and therefore, in this case, assumption (b) is violated. Finally, it is also evident that no material is perfectly isotropic and homogenous but assumption (a) is a justification always applied for idealization for these types of problems.

In light of the above, it is obvious that simulation of the plate penetration process cannot be performed by purely analytical means. The method required should be able to easily handle material non-linearity, as well as large and discontinuous deformations. The finite element method was thus judged as suited for the present problem. An incremental approach, according to which the rigid plate is displaced downwards in steps for each of which material properties and deformations are updated, is selected. Accordingly, the problem is divided into a series of linear elasticity problems (the material is not elastic but all elements are essentially undergoing loading such that rebound of the material is not allowed) for which a finite element solution is obtained. The method is elegant in that the body analysed (i.e. the snow beneath the penetrating plate) is assumed to be composed of a series of triangular plates of material or elements for each of which stresses and strains, corresponding to each of the plate displacement increments introduce above, are known. Similarly, one-dimensional elements representing the shearing mechanisms developed along the vertical sides of the pressure bulb are also incorporated into the analysis. Stresses and displacements for these elements are also updated with plate displacement.

MODELLING

Formulation of the problem

The simultaneous shear and volume change mechanisms that occur during plate penetration, as experimentally demonstrated by Metaxas [8], are schematically illustrated in Fig. 1 showing the shear and compression actions undergone by elements A and B, respectively. The stresses associated with these actions are controlled by the stiffness and strength of the snow which are a function of snow density. The success of the solution procedure thus relies on the ability to determine the density distribution beneath the plate, from which stiffness and strength values can be correctly assigned to any given point within and along the sides of the pressure bulb as a function of plate penetration. The knowledge of the resulting system stiffness at a given plate sinkage then permits the calculation of incremental reaction forces on the plate from which a load-penetration curve can be constructed.

The problem thus involves the determination of the load-deflection relationship of a non-linear system in which the total stiffness K is a function of deflection and deflection rate. The mechanics of the system suggest that the reaction force on the plate at a penetration is composed basically of two parts (Fig. 2a): (a) a force P_v due to the volume change resistance of the snow within the pressure bulb, and (b) a force P_s resulting from the resistance of the snow to shear along the failure planes.

The nature of the problem thus implies that, in fact, these forces are also a function of the plate penetration z, as a result of the variation of properties of the material (i.e. stiffening effect due to snow densification and softening effect due to local shear failures along the planes of cutting shear) as plate penetration progresses. In addition,

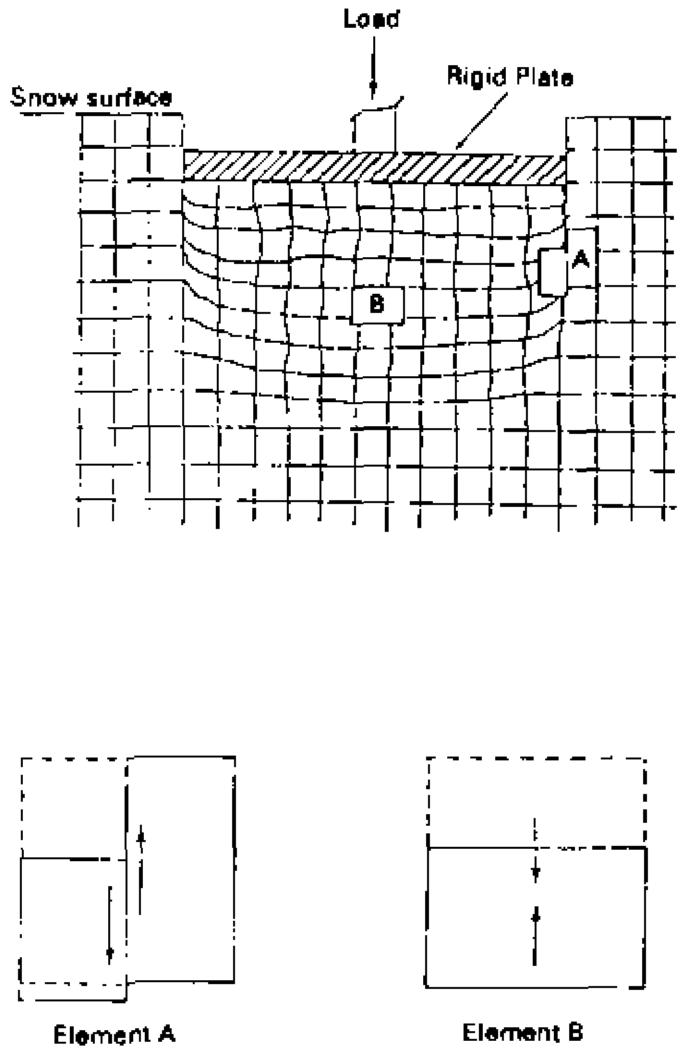

FIG. 1. Volume change and cutting shear mechanics under plate loading.

the penetration speed of the plate u constitutes another parameter to consider since, for a viscous material such as snow, the velocity field generated has a direct effect on material properties and hence, on the reaction force. The total system stiffness can thus be expressed in terms of the volume change and shear components as follows:

$$P(z, u) = P_v(z, u) + P_s(z, u) \tag{1}$$

where: $P(z, u)$ = total reaction force on the plate as a function of plate penetrations and plate penetration rate u; $P_v(z, u)$ = reaction force on the plate due to volume change resistance of snow, and $P_s(z, u)$ = reaction force on the plate due to shear resistance of snow.

Differentiating the above expression with respect to plate penetrations and rewriting it in differential form:

$$\mathrm{d}P(z, u) = \frac{\partial P_v(z, u)}{\partial z}\mathrm{d}z + \frac{\partial P_s(z, u)}{\partial z}\mathrm{d}z \tag{2}$$

$$\mathrm{d}P(z, u) = [K_v(z, u) + K_s(z, u)]\,\mathrm{d}z \tag{3}$$

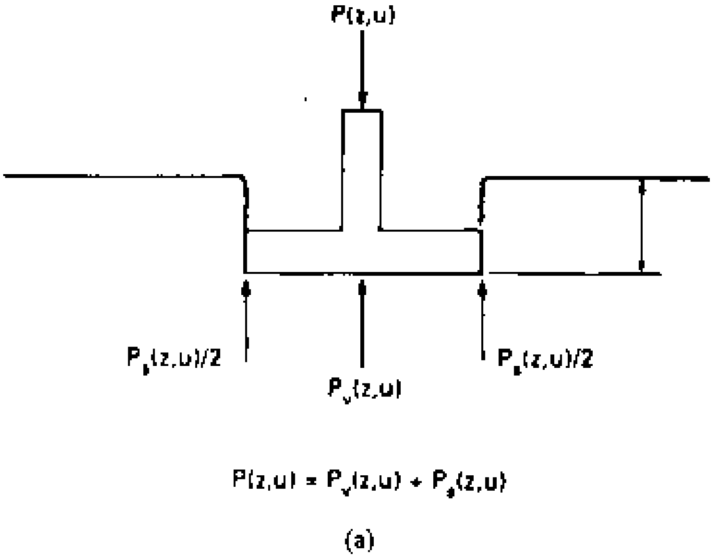

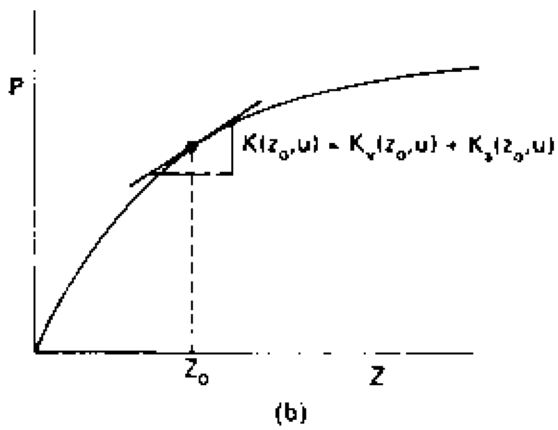

FIG. 2. (a) Forces on plate due to volume change and cutting shear mechanisms; (b) schematic representation of the relationship between stiffness function of load (P)–penetration (z) curve.

where: $K_v(z, u)$ = tangent volumetric stiffness function (Fig. 2b), and $K_s(z, u)$ = tangent shear stiffness function (Fig. 2b).

Equation (3) is the basic relationship that numerically represents the process of a rigid plate penetrating into a snow mass at a constant rate.

Solution

The solution of the problem thus requires knowledge of the volumetric and shear stiffness functions $K_v(z, u)$ and $K_s(z, u)$ both of which are essentially dependent on the plate penetration z and the penetration rate u. The load–penetration relationship can then be determined by integration of equation (3):

$$P(z, u) = \int_0^z [K_v(z, u) + K_s(z, u)]\, dz. \tag{4}$$

The following two sections discuss the above functions in more detail.

Volumetric stiffness function $K_v(z, u)$

For a given plate penetration rate, the volumetric stiffness function in the present model is controlled by density distribution within the stress bulb due to the variation of the compressibility of the snow with density. Prior to any penetration of the plate, the snow deposit in the situation under study has a more or less uniform density. As penetration proceeds, the snow directly below the plate compresses somewhat more than that further below due to the simultaneous action of shear stresses along the pair of planes of cutting shear. A given plate penetration therefore yields a density profile in which density is highest near the plate and decreases with depth until attaining the original value corresponding to the unloaded state. Therefore prior to any plate penetration, the snow exhibits uniform volumetric stiffness properties but as penetration increases, the stiffness at a given point in the snow mass changes and therefore affects the subsequent density distributions which, as a result, causes a change in the volumetric stiffness function $K_v(z, u)$ with plate penetration.

Consider an infinitesimal element of snow, of type "B" in Fig. 1, within the pressure bulb, after a plate penetration Z_p and having a volume dV in which the density is γ and the instantaneous strain rate is $\dot{\varepsilon}$ (Fig. 3). Also let the compressive modulus, defined herein as the ratio of stress to strain under pure axial deformation conditions, be $E_c(\gamma, u)$ for the density γ and the strain u. Upon an additional increment of plate displacement ΔZ_p, both axial and shearing strains ε_x, ε_y, ε_{xy} develop, the latter due to the distortion effect of shearing stresses generated along the planes of cutting shear. The strains are then related to stresses through the compressive modulus defined above and the Poisson's ratio of the material. The work done in deforming the given snow element is then:

$$dW = (\sigma_x \varepsilon_x + \sigma_y \varepsilon_y + \sigma_{xy} \varepsilon_{xy}) dV. \tag{5}$$

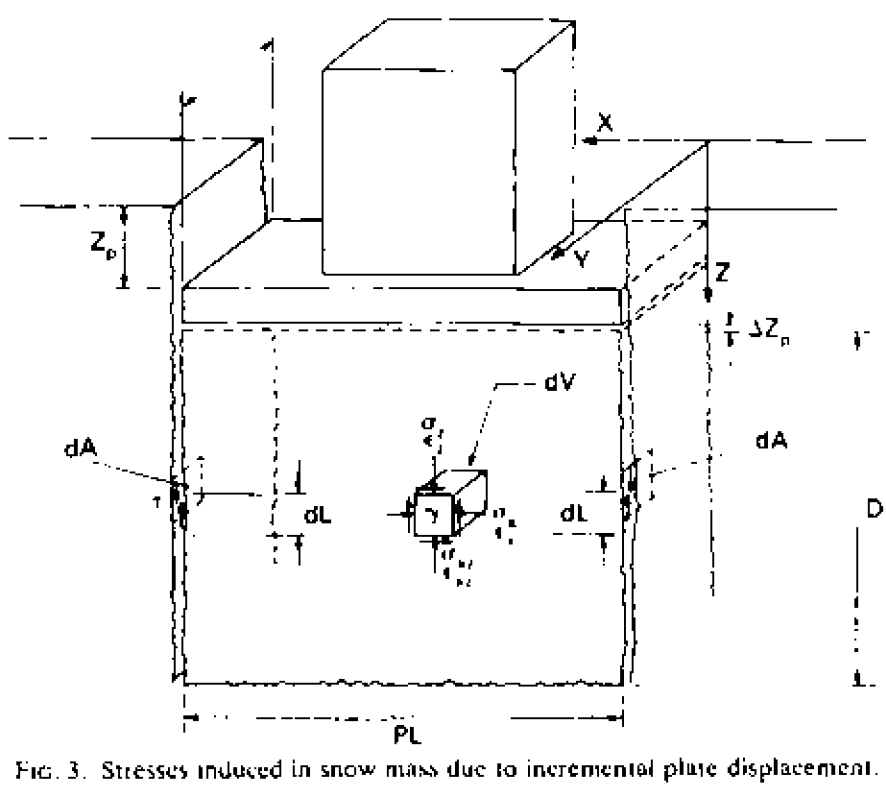

FIG. 3. Stresses induced in snow mass due to incremental plate displacement.

Integration of the above expression over the entire pressure bulb yields the total energy spent in compressing and distorting the snow for the given plate incremental displacement. Due to the particular boundary conditions of the present problem and the low Poisson's ratio of the material, the energy involved in the distortion of the snow mass within the pressure bulb is small relative to the volume change energy. It can therefore safely be stated that evaluation of the integral of equation (5) over the volume of the pressure bulb is basically equal to the volume change energy component due to an increment of plate penetration Z:

$$\Delta E_v = \text{volume change energy} = \int_0^D \int_0^{PW} \int_0^{PL} (\sigma_x \varepsilon_x + \sigma_y \varepsilon_y + \sigma_{xy} \varepsilon_{xy})\, dx\, dy\, dz. \quad (6)$$

Assuming plane strain conditions and realizing that the pressure bulb depth is, in general, a function of plate penetration Z_p:

$$\Delta E_v = PW \int_0^{D(Z_p)} \int_0^{PL} (\sigma_x \varepsilon_x + \sigma_y \varepsilon_y + \sigma_{xy} \varepsilon_{xy})\, dx\, dz. \quad (7)$$

The above quantity is equal to the work done by the incremental force P_v. Therefore;

$$\Delta E_v = \Delta P_v \Delta Z_p. \quad (8)$$

From which the volume change stiffness function evaluated at a plate penetration Z_p can be obtained:

$$K_v(Z_p, u) = \frac{\Delta P_v}{\Delta Z_p} = \frac{\Delta E_v}{(\Delta Z_p)^2}. \quad (9)$$

Substituting for E_v (equation 7) in equation (9), the volumetric stiffness function is thus:

$$K_v(z, u) = \frac{PW}{\Delta (Z_p)^2} \int_0^{D(Z_p)} \int_0^{PL} (\sigma_x \varepsilon_x + \sigma_y \varepsilon_y + \sigma_{xy} \varepsilon_{xy})\, dx\, dz. \quad (10)$$

The key in the determination of the function $K_v(Z_p, u)$ thus lies in defining the following functional relationships:

(1) distribution of incremental stresses and strains, density, strain rate and pressure bulb depth as a function of plate penetration Z_p. These functions can be determined from the proposed finite element model and are thus obtained by numerical computation.

(2) compressive modulus of snow as a function of density and plate penetration rate. This function is a characteristic describing the compressibility of the material and therefore needs to be obtained through tests.

Shear stiffness function $K_s(z, u)$

The shear stiffness function is linked with the effect of shear stresses supporting the stress bulb along the two planes of cutting shear described before. As for the volume change component, the shear stiffness of the system is dependent on the amount of plate penetration, density distribution and penetration rate.

When the plate penetration process is initiated, high vertical shear stresses develop below both edges of the plate so that the shear strength of the snow material at these points is likely to be exceeded thus starting the cutting shear mechanism.

If one considers that the two planes of shear are composed of a series of elements of the "A" type in Fig. 1, it is clear that, as the plate begins to penetrate into the snow mass, such an element located immediately below one of the edges of the plate eventually undergoes a shear deformation sufficient to cause a shear stress build up and consequently, failure of the element. Other elements further below are subjected to smaller displacements which, depending on the stiffness and strength of the material in shear at the density across the plane of deformation, may also imply failure. However, at a certain distance below the edges of the plate, these displacements and stresses are eventually insignificant so that failure does not occur. Upon an additional increment of plate penetration, the shear elements may or may not fail depending on the respective cumulative shear stress and shear strength associated with them. The failure condition for snow in shear is therefore defined by consideration of the cumulative shear stress in a given element and the value corresponding to failure, determined by the shear resistance of the snow material at a density equal to that along the plane of shear: i.e. failure occurs if $\tau_c > \tau_f(\gamma)$, where τ_c = cumulative shear stress in the given shear element; γ = snow density along the shear plane of the element, and $\tau_f(\gamma)$ = shear resistance of the snow at a density equal to that across the plane of shear.

Failure in the present context refers to the point of breakage of bonds between snow particles, corresponding to the maximum or peak shear stresses that the snow material can resist at a given density. At larger strains, the behavior of the material is somewhat questionable. In the case of a relatively rapid shearing action (i.e. high strain rate) the material exhibits a strain softening behavior with a steadily decreasing residual shear strength due to the self-polishing action (heat generated due to friction melts down particles) of the two surfaces rubbing against one another.

The shear stiffness function $K_s(z, u)$ is determined by the following analysis. Consider a shear element of surface area $\mathrm{d}A$, as shown in Fig. 3 in which the snow density and instantaneous strain rate at its center are γ and $\dot{\varepsilon}$, respectively, when the total penetration of the plate is Z_p. If the plate is further displaced downwards by an amount ΔZ_p, a shear strain develops, whose value is related to a corresponding shear stress τ through the stiffness of the material in shear, which, in general, is a function of density γ, strain ε and strain rate $\dot{\varepsilon}$:

$$K_s = G(\gamma, u). \tag{11}$$

The total shear force developed in the process is:

$$\mathrm{d}P_s = \tau\,\mathrm{d}A = \tau\,\mathrm{d}y\,\mathrm{d}z. \tag{12}$$

The total area of shearing consists of the two vertical planes of cutting shear passing through the edges of the penetrating plate. Therefore, integrating the above equation over this area yields the shear force due to an incremental plate displacement ΔZ_p:

$$\Delta P_s = 2\int_0^D\int_0^{PW} \tau\,\mathrm{d}y\,\mathrm{d}z. \tag{13}$$

For plane strain conditions, and setting the stress bulb depth D to be a function of the plate penetration Z_p:

$$\Delta P_s = 2PW\int_0^{D(Z_p)} \tau\,\mathrm{d}z. \tag{14}$$

The shear stiffness function evaluated at a plate penetration Z_p is then

$$K_s(Z_p, u) = \Delta P_s/\Delta Z_p = \frac{2PW}{\Delta Z_p}\int_0^{D(Z_p)} \tau \, dz. \tag{15}$$

Again, as for the volume change stiffness function, the determination of the shear stiffness function thus requires investigation of two types of functions:

(1) distribution of shear stresses along the planes of cutting shear as a function of plate penetration Z_p: i.e. $\tau(Z, Z_p)$. This function is obtainable through the finite element form of analysis proposed in this study.

(2) parameters describing the shear stress–strain behavior as a function of density γ, strain ε and strain rate $\dot{\varepsilon}$: i.e. (a) shear strength: $\tau_f(\gamma, u)$, and (b) shear modulus: $G(\gamma, \varepsilon, \dot{\varepsilon})$.

FINITE ELEMENT ANALYSIS

Idealization

The solution of engineering problems always implies a certain degree of idealization of the material considered. In the present study, snow is assumed to have the following properties: (a) the material is homogeneous and isotropic; (b) the material is weightless; (c) Poisson's ratio is 0; (d) the material exhibits a linear–plastic behavior in pure shear such that stress increases linearly with strain until failure and remains constant afterwards, and (e) the material is non-frictional (i.e. shear stresses and strength are independent of normal stresses).

In addition, the material is known to exhibit the following characteristics: (a) the material is non-linear and highly compressible thus implying large strain behavior; (b) the material exhibits a stiffening type of stress–strain curve in compression such that its stiffness increases with strain, and (c) the shear strength of the material depends on density and shearing velocity.

Further assumptions concerning the solution scheme itself can be summarized as follows:

(a) the plate penetration problem can be treated on a plane strain basis. This seems reasonable in the light of the loading conditions imposed during testing in which the snow deposit is constrained to deform in basically two directions;

(b) body forces due to gravity are neglected since stresses, strains, reactions, etc., due to external loading only are of interest;

(c) the material fails in shear when the cumulative shear stress at a given point along the shearing plane exceeds the shear strength corresponding to the density at that same point;

(d) the stiffness of snow in compression is directly dependent on accumulated volume change and, hence on density;

(e) the planes of cutting shear passing through the edges of the plate are vertical and symmetrical with respect to the plate;

(f) the effect of strain rate is included in the analysis only through the use of material properties in compression and shear corresponding to a deformation velocity equal to that of the penetrating plate;

(g) the shear stiffness parameter K_s is kept constant throughout the analysis although it is recognized that K_s is in general a function of density, strain and strain rate.

Finite element mesh and boundary conditions

The initial step in the finite element solution of a given problem is the design of a mesh physically representing the body under study with proper consideration of boundary conditions. In the present case, the body in question is the snow mass extending sufficiently far from the plate to cover the maximum pressure bulb depth and contained between the two shearing planes passing through the edges of the plate. In addition, a layer of snow just outside the shear planes is included for a more realistic representation. This body is divided into constant plane strain triangular elements and joint elements [9] are used to model the effect of vertical shear stresses supporting the pressure bulb along its walls. Due to the symmetrical nature of the problem, only one half of the bulb is considered in the finite element analysis. The mesh used in this study is shown in Fig. 4.

The choice of displacement boundary conditions, rather than load boundary conditions, for the finite element analysis is motivated by two main factors pertaining to the nature of the problem at hand: (a) in the plate penetration tests, displacement of the plate is controlled by the constant penetration rate and the corresponding reaction force on the plate. The use of displacement boundary conditions combined with the incremental finite element technique used in this study, in which the plate is progressively displaced into the snow material and corresponding reactions are computed from nodal displacements, therefore renders the numerical simulation that much more realistic, and (b) a better control on the large strain behavior of the material is achieved with the displacement boundary condition approach which, in

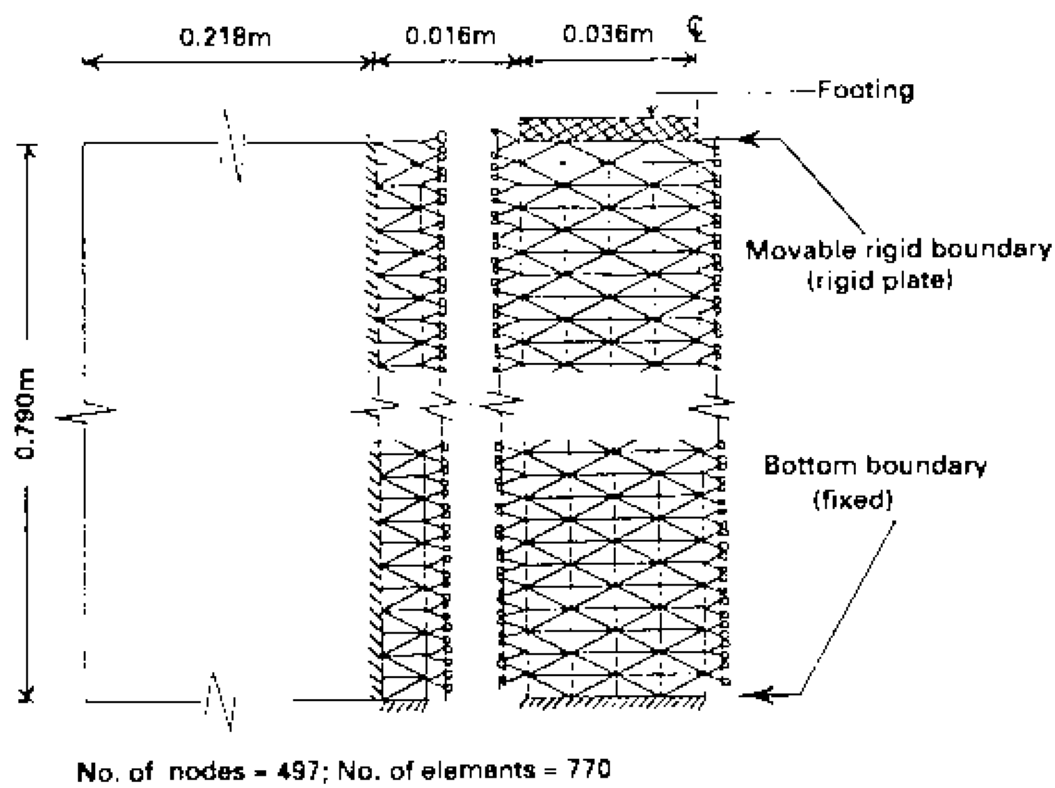

FIG. 4. Boundary conditions for finite element analysis

addition, enables the constant updating of material properties (both in compression and shear) as plate penetration progresses.

Furthermore, the selection of relatively small increments of displacement not only enables the handling of the brittle behavior of the material in shear but also preserves the validity of the small strain assumption induced in the stiffness matrix formulation of the constant strain triangular elements. Consequently, the detrimental effect of geometric non-linearity is also diminished by the use of such an incremental procedure.

The boundary conditions assumed for the solution of the present problem are schematically described in Fig. 4. The top of the mesh, representing the snow surface, rigidly moves downwards, thus simulating penetration of the plate in the snow. These surface nodes are however free to displace horizontally thus implying a smooth plate, i.e. displacements are allowed in both vertical and horizontal directions. The left-hand side boundary, bounding one of the layers just outside the planes of cutting shear is fixed, i.e. at a distance 0.016 m from the plate, both horizontal and vertical displacements are set to zero. Joint element nodes, at the edge of the plate, are allowed to move freely in the vertical direction while horizontal motion is prevented, i.e. horizontal displacements are zero. The bottom boundary, which is located sufficiently far away from the plate in order to minimize bottom boundary effects, is also fully restrained, i.e. both horizontal and vertical displacements at each node are zero. Motion of the nodes along the right-hand side (i.e. the plane of symmetry) is constrained to be vertical only due to considerations of symmetry of the problem, i.e. displacements are allowed in the vertical direction and restricted in the horizontal direction.

Solution procedure

The finite element algorithm used in the solution of the problem is derived from a computer program developed by Hanna [10] and begins with the initialization of material properties according to the initial density of the snow, i.e. before any plate penetration occurs. The stress–strain properties of snow in compression and shear are functions of density and plate penetration speed so that the corresponding parameters, $E_c(\gamma, u)$ (compressibility), and $\tau_f(\gamma, u)$ (shear strength) obtained from confined compression and vane shear tests respectively, are all initially defined according the results from tests performed on snow at the initial density. More specifically, the value of modulus of elasticity initially assigned at the triangular continuum elements is equal to the other tangent modulus of the stress–strain curve in the confined compression test at zero strain. The value of Poisson's ratio is set to zero and is kept constant throughout the entire analysis. Similarly, the shear stiffness of joint elements is initally assigned a value, which is assumed to remain constant, and other maximum stresses tolerated by these elements correspond to the shear strength of the snow at the initial density. The normal stiffness is irrelevant in the present analysis, since the normal displacement of joint elements is prevented according to the specified boundary conditions, but is arbitrarily given a value of 100 000.

The size of the specified incremental plate displacement (i.e. 2 mm) used in the finite element analysis is determined simply by dividing the maximum plate penetration (approximately 70 mm) by the total number of increments, which, in the program presented in this study, is set to 35.

The proposed method of solution thus consists of a series of finite element analyses, each applying to an increment of plate displacement of 2 mm, for which material properties in the form of stiffness parameters, are obtained from characteristics derived from test results. The non-linearity of the material implies the use of an iterative technique, developed for the triangular elements, as discussed by Zienkiewicz [11] and Yong et al. [12].

Following a particular increment of plate displacement, stresses and strains in triangular elements are computed from the resulting incremental nodal displacements and the non-linear analysis procedure mentioned above is undertaken and is carried through for a maximum of 12 iterations. Upon completion of the algorithm for material non-linearity, stresses in joint elements are examined. Failure in shear at various points along the vertical cutting shear planes is reflected, in the proposed model, by a total or cumulative shear stress in a given joint element greater than that tolerated by the snow material at a density equal to that across the plane of shearing. When failure does occur, a very small value (i.e. 0.0001) of shear stiffness is assigned to the element and shear stresses subsequently remain constant at the failure value according to the idealized stress–strain curve in shear. As a result, after failure of a given joint element, the difference between the cumulative shear stress and the stress corresponding to failure must be "released" back into the snow mass on both sides of the plane of shear. This is done by converting the excess shear stress into an equivalent system of vertical forces [12] which are then applied to nodes on either side of the plane(s) of shear. A finite element analysis, also including the non-linearity algorithm, is performed for this loading situation while keeping the plate stationary. The resulting reactions on the plate prove to be opposite to those generated during the increments of plate penetration. Ideally, the stress release cycle should be repeated until the excess shear stress in any joint element is zero, but, because of computer time costs, additional analyses are undertaken only if the last increment (negative) reaction load on the plate is of significant magnitude with respect to the value corresponding to the previous stress release cycle. Incremental reactions due to either plate penetration or excess shear stress releases are determined by summation of the individual vertical reactions exerted on the nodes representing the plate–snow interface and multiplication of the results by the plate width PW (Fig. 3) as a result of the assumed plane strain condition. The resulting value is then doubled since, as it can be recalled, the finite element analysis performed applies to only half of the plate. The total updated load on the plate is then computed by summation of the incremental reaction loads on the plate computed for each plate displacement increment or excess shear stress analysis.

At the end of every increment of either plate displacement or shear stress release cycle, the nodal coordinates are then updated simply by adding the incremental horizontal and vertical displacement to the coordinates at the end of the previous increment. The density distribution beneath the plate can thus be obtained. The basis for computing density is the change in area of the triangular elements as deformations occur. The area of these elements at any stage of plate penetration is calculated from the updated coordinates of the nodes. Since the initial area of each element in the original, undeformed finite element mesh is computed and stored in the finite element mesh generating subroutine, the ratio of deformed to undeformed element areas can be determined. Due to the plane strain condition imposed on the problem, these ratios are also the volume ratios from which density is obtained through the following expression:

$$\gamma = (A_0/A)\gamma_0 \tag{16}$$

where: γ = updated density in a given element; A_0 = initial area of undeformed mesh coordinates; A = area of deformed element (i.e. area computed from updated nodal coordinates), and γ_0 = initial snow density (snow density prior to plate penetration). From the resulting density distribution within the snow mass, an equivalent average strain in each triangular element is then determined in order to prepare the non-linear analysis in the next increment.

The shear stress in failed joint elements is then recorded in order to maintain the bookkeeping on the updated state of shear strain in joint element subjected to subsequent excess stresses which must then be removed leading to the stress release effect discussed earlier.

The finite element algorithm proceeds to another increment of plate displacement equal to 2 mm and the entire analysis is repeated, each time with proper consideration of the variation of material properties with density distribution, which is dependent on the total plate penetration. The procedure is terminated when the plate penetration equals a value selected according to the maximum plate penetration achieved in the experiments (about 70 mm).

EXPERIMENTATION

Sample preparation

Artificial snow material was used in this study because of the critical need to replicate test samples of snow. Snow was produced by crushing 3-day old ice with a pulverizing machine in a cold room of inside average temperature −13 °C with fluctuation of +3 °C due to defrosting cycles. The ice crushing process was repeated three times in order to achieve a snow density of approximately 0.35 Mg/m^3. Two types of snow, distinguished by the number of ageing days in the cold room were used: (1) 4-day-old snow, and (2) 30-day-old snow. Snow samples were aged in the same cold room inside which the snow was produced. The grain size distributions of the snow used as a function of ageing time are shown in Fig. 5.

Confined compression testing

Confined compression tests basically consisted of compressing, at a specified deformation rate, cylindrical samples of snow from its initial density to a final specified density of approximately 0.6 Mg/m^3 while recording the load–deformation response. The rate of deformation used was 0.58 mm/s. Tests were conducted using plexiglass cylinders of 38 mm inner diameter, 6 mm wall thickness and 178 mm height, perforated by small holes to allow for air extrusion during compression of snow samples. Artificially prepared snow was deposited into the cylinders with a 2.4 mm size sieve from a height of 100 mm. The initial density of snow, determined using a Ohaus triple beam balance with a precision of 0.1 g, was more or less constant and equal to 0.35 Mg/m^3 ± 1.2%. Ageing of samples took place inside the cold room in thermally insulated boxes to avoid temperature change effects due to defrosting cycles. These boxes provided protection to the samples from air movement, humidity, light and other factors possibly influencing the ageing process.

Each individual test began by placing a cylinder containing a snow sample on the

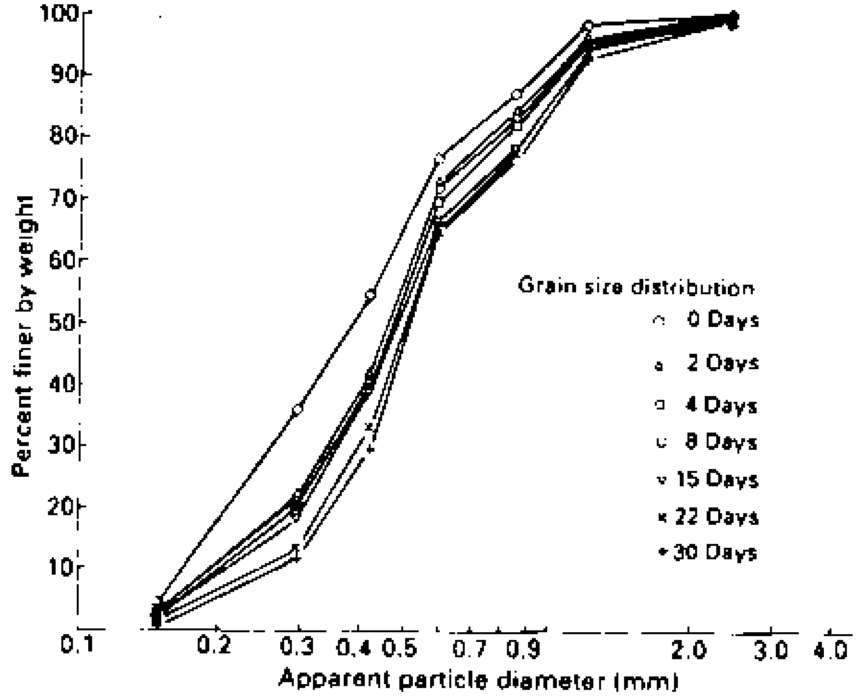

FIG. 5. Variation of grain size distribution of artificial snow with age.

compression machine piston, just small enough to fit inside the cylinder. Friction between the piston and the interior wall of the cylinder was thus minimal. The compression machine was then started moving the piston upwards at a constant specified rate, thus compressing the snow. Friction between the snow and the cylinder wall was negligibly small due to both the self-lubricating properties of the snow and the smoothness of the plexiglass material. As the piston moved, the load–displacement response was recorded on the chart recorder. The compression machine was stopped at piston penetration of approximately 76 mm, corresponding to a density of about 0.6 Mg/m^3.

Shear testing

The shear strength of snow was investigated through vane shear tests on snow compressed to a given density. More specifically, these tests were performed on the snow compressed during the plate penetration process. Once the desired maximum plate pènetration was achieved, the plexiglass boxes were turned on their side and the front side wall removed. Samples were then extracted from the snow mass using thin walled aluminum tubes for determination of density. Density was calculated from the weight of the samples and the volume of the tubes. A portable hand vane was then utilized to determine the shear strength of the snow at approximately the same location from which the snow samples were taken.

Plate penetration testing

Speed controlled plate penetration tests were performed on deep snow of 0.35 Mg/m^3 approximate initial density and aged for a specified number of days in the cold room. Plexiglass boxes, measuring 0.54 m in length, 0.79 m in depth and 0.1 m in width, contained the snow samples for plate penetration testing. The length and depth of the boxes were chosen in relation to the loading plate length and maximum penetration depths to avoid side and bottom effects respectively. A 71 × 71 mm square plate of 13 mm thickness was used.

Test began by placing a given snow box on the platform and setting the deformation rate control switch to the position corresponding to the specified value of platform speed. The load cell and displacement transducer recorded the reaction force on the plate and the platform displacement respectively. Simultaneously, photographs of the grid, drawn on the snow surface during sample preparation using fine black sand, were taken at given time intervals thus, recording the deformation patterns below the plate induced by the loading process. A schematic representation of the apparatus used for plate penetration tests is shown in Fig. 6.

MATERIAL PARAMETERS

The proposed method of analysis described previously implies assumptions and approximations necessary to the formulation and solution of the present problem. In

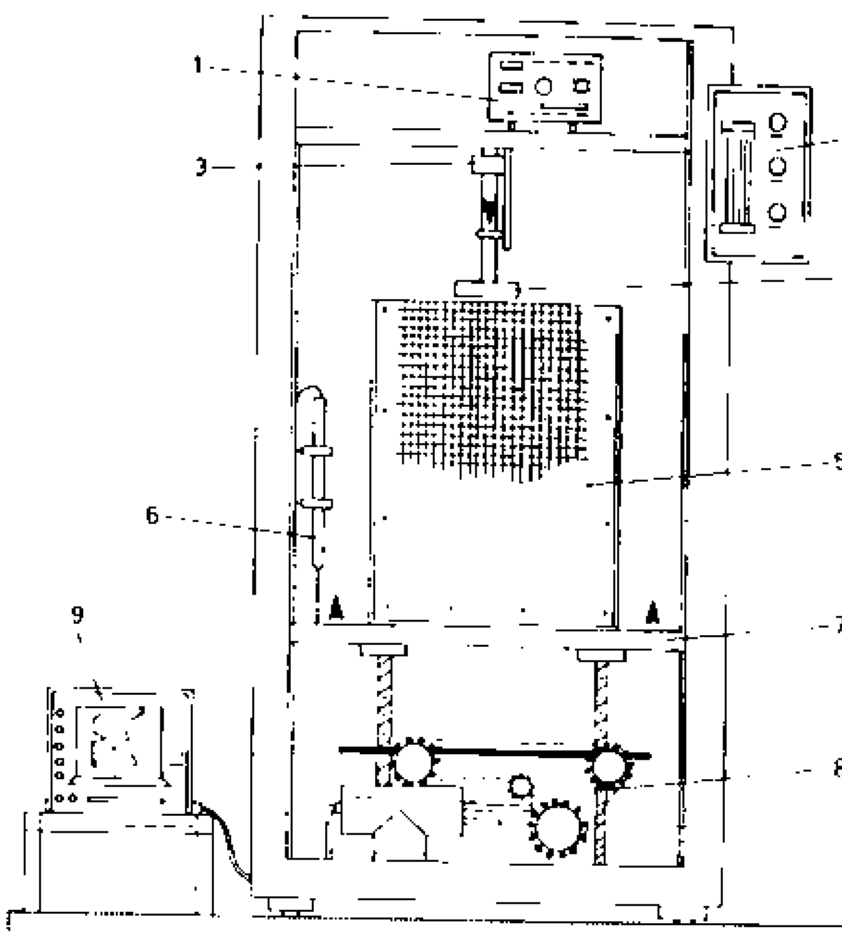

1 Switch box
2 Speed control unit
3 Load cell
4 Rigid plate
5 Snow box
6. Displacement transducer
7. Moving platform
8. Driving system
9 Recording system

FIG. 6. Apparatus used for plate penetration test.

addition, the components of the proposed model require the following characteristics of the snow material:

(1) compressibility as a function of density (axial stress–strain relationship for fully confined conditions),
(2) shear stress–strain response as a function of density.

In view of the above, the experimental program carried out during the course of this study was designed to provide required material input parameters as well as for verification purposes of the proposed model.

Typical results from the three types of tests are shown and discussed in the following sections.

Confined compression response

In a confined compression test, the material undergoes an axial deformation while lateral displacements are prevented. For a material with a relatively high Poisson's ratio, a lateral pressure develops and therefore the confining stress on the sample increases due to the restriction of lateral movement by the rigid wall of the plexiglass container. For soils, stress–strain behavior is dependent on confining pressure and consequently, a confined compression test yields information of questionable value since the confining pressure varies throughout the test. However, when a material with a low Poisson's ratio, such as the snow types used in the present study, is tested in similar conditions, lateral deformations are minimal and thus lateral pressure is small in relation to the axial pressure. It can therefore be deduced that for such a material, the effect of confining pressure is insignificant.

Stress–strain relationships under confined compression conditions were obtained from test results simply by dividing the recorded load and piston displacement values by the cross-sectional area and original height of the sample, respectively. An example of a typical curve is illustrated in Fig. 7(a), showing a generally increasing slope, i.e. characteristic of a stiffening material, and the presence of microfractures also referred to as the "saw-tooth" effect and previously reported by Yong and Fukue [13]. This microfracturing behavior is reflective of local failures caused by fracture of bonds between snow particles due to local stresses exceeding the bond strength. A resulting load transfer to other bonds occurs until their strength is in turn exceeded, due to stress superposition. A stress release is exhibited whenever bonds are broken and a subsequent stress build-up occurs as other bonds accept a share of the load transferred to them. The process, however, also causes packing of the snow particles which then offer more and more resistance to further compression. Their effect seems to be dominant as the shape of the stress–strain curve, including both the bond fracture and densification mechanisms, is typically concave up thus implying that the material becomes stronger as load increases, in spite of the increasing number of broken bonds. It can also be seen from the stress strain curve that continued compression eventually produces a condition in which microfracturing eventually stops thus seeming to indicate that bonds breakage becomes negligible after a certain point. This condition arises when the snow material, having undergone a given volumetric strain, reaches the "threshold density", also discussed by Yong and Fukue [13]. Threshold density can be formally defined as the snow density at which no microfracturing will subsequently develop when the snow is subjected to controlled confined compression testing conditions and depends on the deformation rate.

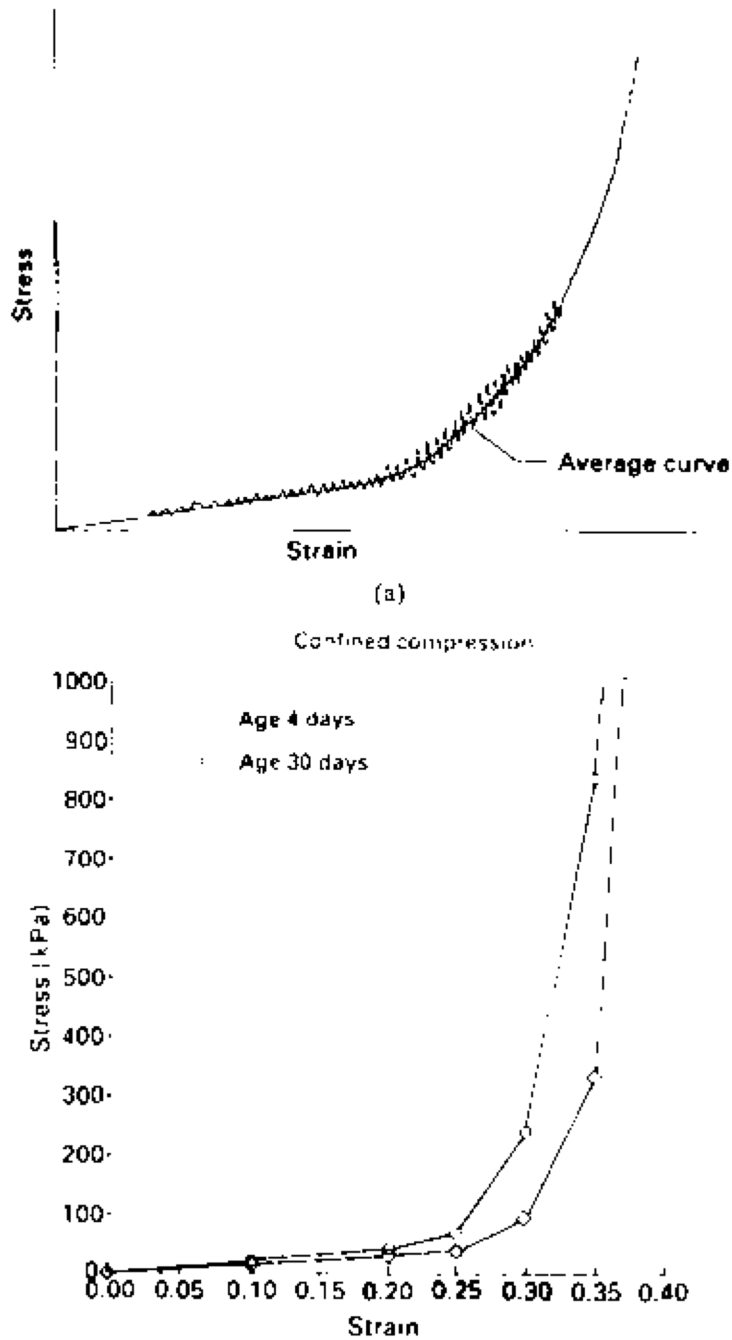

FIG. 7 (a) Typical curve from a confined compression test; (b) confined compression test results with age effect

Beyond the volumetric strain, corresponding to the threshold density, stress increases rapidly with respect to strain as microfracturing no longer occurs and as the degree of particle packing increases. Ultimately, further compression would produce a high density snow (0.60 Mg/m^3 and greater) with a higher Poisson's ratio and thus for which the confining stress during confined compression testing can no longer be disregarded. The analysis of the behavior of such a type of snow is, however, beyond the scope of the present study.

In the present work, results from confined compression tests are viewed simply as a characteristic to be inputted in the developed finite element model. The data describes the stress–strain behavior in compression or compressibility of the snow material. The amplitudes of the stress releases observed during tests were seen to be small with respect to the stress values themselves so that, consequently, the "saw-tooth" effect due to microfracturing is ignored as a parameter describing the stress–strain response. An average curve was thus fitted through the center of the recorded peaks and troughs, as shown in Fig. 7(a). The resulting stress–strain relationships obtained for the two snow types (i.e. age 4 and 30 days) are shown in Fig. 7(b). Ageing of snow increases the degree of bonding and, as expected, the stress corresponding to a particular value of strain increases with the number of ageing days, thus demonstrated in the higher resistance of older snow.

Response in shear

In a vane shear test, it is assumed that the snow is tested at essentially constant density. The fact that the failure plane is predetermined is consistent with the idealized version of the real situation of plate penetration in which the location of the shear plane is known (i.e. vertical planes through the edges of the plate). Although, in reality, the failure plane develops progressively as opposed to being established completely prior to loading as in the analytical model, it was felt that results from vane shear tests could be useful in the description of characteristics representing the behavior of snow at points where the material is acting principally in pure shear (i.e. along the failure planes).

Results from vane shear tests essentially consisted of shear strength–density relationships, corresponding to the given deformation rate, for the two types of snow used. Shear strength of snow was computed from the vane reading and a calibration factor. Results, illustrating the effect of age, are graphically displayed in Fig. 8. A general pattern is observed according to which, as expected, shear strength of snow

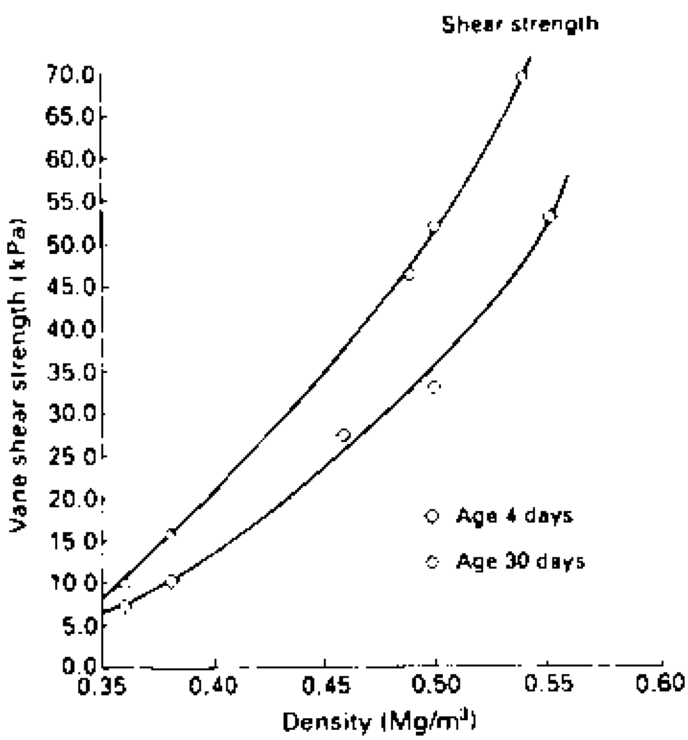

FIG. 8. Vane shear test results with age effect.

increases with density as well as with the number of ageing days. During the vane shear tests performed during the study, it was not possible to measure the shear resistance as a function of vane rotation since the recorded vane reading corresponded to the maximum shear stress developed (i.e. the shear strength). This, however, did not cause many problems in the formulation of the present model as the post-peak behavior in shear was actually idealized in this study. Since the proposed model does require a stiffness parameter of snow in shear, which can only be obtained from a shear stress–deformation curve, such a number was thus assumed and considered as an additional parameter in the present study.

Shear tests thus provided means to determine the shear resistance of snow at a given density but other parameters describing the shear stress–deformation curves required in the model had to be obtained from other sources due to limitations of the experimental facility.

Plate penetration response

A plate penetration test represents a loading situation in which both volume change and shear mechanism occur simultaneously. As penetration of the plate in the snow sample progresses, a reaction load on the plate develops because of the resistance of the snow beneath the plate to undergo volume change and shear along the vertical planes of cutting shear passing through the edges of the plate. The recorded load penetration response of a given snow type corresponding to a given penetration rate is therefore the results of the combined action of the two mechanisms mentioned above.

The load–penetration curves for ages 4 and 30 days are shown in Fig. 9(a) and (b) respectively. The "saw tooth" effect, observed in confined compression tests, is also exhibited due to elements of snow within the stress bulb beneath the plate being subjected to a loading condition similar to that of confined compression as a result of the low Poisson's ratio of the material. As the plate penetrates deeper into the snow, more and more of these elements are involved in the volume change process, i.e. the stress bulb extends deeper as penetration progresses. This reasoning seems to be supported by the fact that the amplitudes of stress release increases with plate sinkage, due to a greater amount of snow material undergoing the bond breaking mechanism.

As mentioned earlier, a plate load–penetration curve reflects the combined action of volume change and shearing mechanisms and, therefore, it can be expected that its shape is governed by the individual characteristics, describing the behavior in volume change and pure shear, as obtained from confined compression and shear tests, respectively. During plate penetration in deep snow, the depth of the pressure bulb beneath the plate is controlled by the magnitude of shear stresses supporting it along its sides. As the plate sinks into the snow, the shear strength of snow at any point along the planes of cutting shear could be exceeded depending on the density of the snow and cumulative shear stress at that point. It is therefore obvious that maximum stress bulb support in terms of side shear action occurs at the beginning of the plate penetration process and decreases as more snow material is stressed beyond its shear strength. Since the stiffness in shear of snow elements located along the planes of cutting shear is reduced to a negligible value after shear failure occurs, it thus becomes evident that the total stiffness of the system in shear decreases with increasing plate penetration.

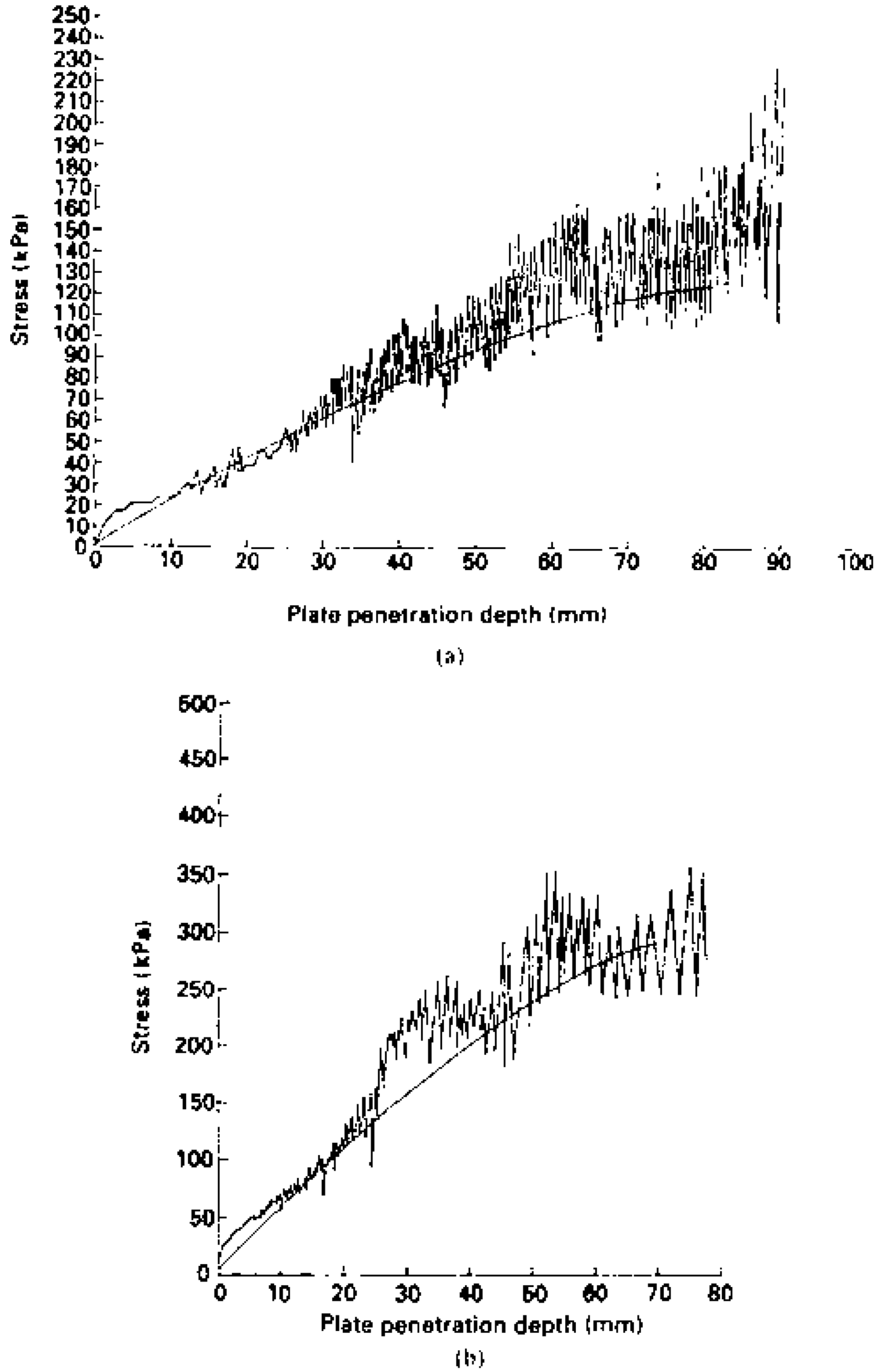

FIG. 9 (a) Plate penetration test results: age 4 days; (b) plate penetration test results: age 30 days.

On the other hand, the volume change mechanism occurs simultaneously during which the density of snow within the stress bulb generally increases. As a result, and referring back to the stiffening behavior of snow under compression loading, the resistance of the system to volume change increases (i.e. compressibility decreases). The shape of a given plate penetration curve therefore depends on two mechanisms with opposite effects, i.e. softening effect in shear and stiffening effect in volume change. A plate load–penetration curve of the softening types (i.e. tangent slope decreases with increasing plate penetration) therefore represent a situation in which the cutting shear mechanism along the failure planes is dominant over the volume change action of the snow within the stress bulb beneath the plate. Similarly, a curve of the stiffening type (i.e. tangent slope increases with plate penetration) indicates that the volume change effect is more significant than the cutting shear effect. It is suspected that the first case applies to relatively old snow with a high degree of bonding (high shear strength) and low compressibility whereas the second case is typical of fresh or low age snow, characterized by a low shear strength and high compressibility. Following the same type of reasoning, a relatively linear plate load–penetration curve reflects the situation in which both volume change and shear mechanisms participate equally in the vertical support of the pressure bulb and thus tend to counteract one another. The validity of the above statements is demonstrated by the results of the plate penetration tests. The load–penetration curves from a test performed on 4 day old snow (Fig. 9a) show that the response is essentially linear whereas results from the tests performed on older snow, aged 30 days, shows a strain softening behavior (Fig. 9b). The plate penetration behavior for the two snow types considered is thus as expected. The curves fitted through the experimental plots in Fig. 9(a) and (b) serve as reference for comparative purposes with analytical predictions.

PREDICTION AND COMPARISON

Load penetration curves

The plate penetration curves are expressed in terms of stresses on the plate as a function of penetration. Plate stress is obtained by dividing the reaction load by the area of the plate. The stress–penetration relationships for 4-day-old snow obtained from the plate test and predicted by the finite element model are depicted on the plot in Fig. 10(a) for comparison purposes. The experimental curve shown in the same figure is the same as that fitted through the experimental graph (Fig. 9a) which passed approximately half-way between the mean of the band of the test curve and the lower boundary of the same curve. The reason for the selection of such a reference curve is due to the fact that the finite element model predicts the plate load after stress release caused by failing shear elements. In the actual case, the stress vibrations observed are produced by both the microfracturing of snow while compressed and the stress release effect mentioned above. It is therefore difficult to affirm that the lowest boundary of the plate penetration curve represents the behaviour after shear element stress release since the microfracturing effect is also incorporated into the response with the result that it is impossible to separate the two components. Similarly, the mean value of the same curve does not necessarily represent the response that can be compared to the finite element prediction because of the stress release effect although the latter is not suspected to cause large drops in plate stress. Therefore, due to the above arguments, a curve in the model of the mean of the band and the lower boundary was selected as the reference experimental curve.

In the predicted response, the effect of shear stiffness is included. For the values of K_s considered, the agreement between experimental and finite element results is reasonable (Fig. 10a). The shape of both experimental and predicted curves is similar in that the relationships are characterized by a bi-linear type of behavior such that the

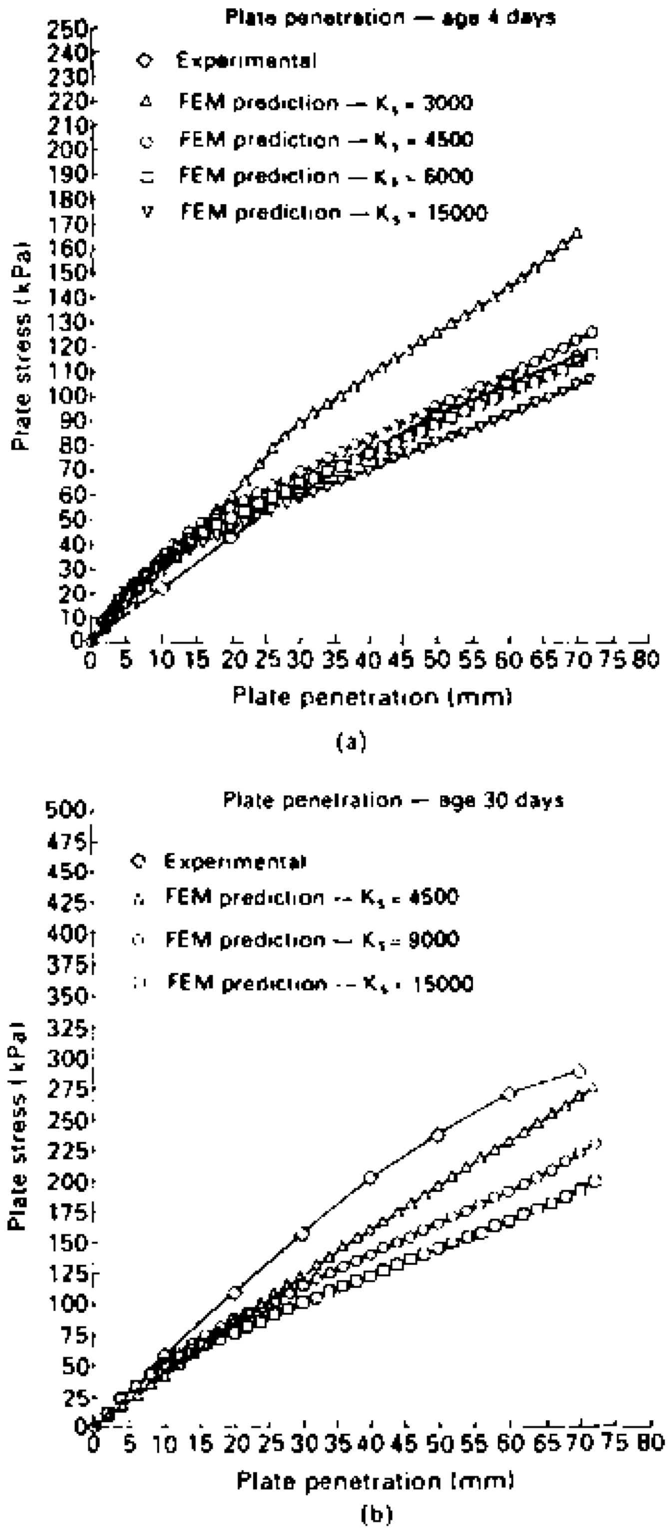

FIG. 10. (a) Experimentally obtained and predicted plate penetration curves: age 4 days; (b) experimentally obtained and predicted plate penetration curves: age 30 days.

response is essentially linear, starting at a given slope, then followed by a decrease in slope. It should also be noted that the predicted stress–penetration response is somewhat sensitive to the value of shear stiffness K_s and thus different values of K_s generate different curves. In the set of curves shown in Fig. 10(a), the relationships pertaining to $K_s = 4500$ and $K_s = 6000$ seem to give the test results or close agreement with the experimental curve. The curve corresponding to $K_s = 3000$ overestimates the response, whereas that for $K_s = 15000$ tends to underestimate it. In general, the plot on Fig. 10(a) implies that an increase in K_s lowers the predicted curve whereas a decrease in K_s tends to raise it.

The reaction of the curve to a change in shear stiffness can be explained as follows; a low value of K_s implies a "ductile" behavior of snow in shear so that elements of the material along the failure planes, and thus acting principally in shear, tolerate relatively large displacements before mobilizing the full shear strength. In such a case, if the value of K_s is too low in the model, the total shear stiffness of the system (i.e. the stiffness contributed by the shear elements along the planes of shear) changes too slowly, as compared to the real situation, since few elements have failed for a given plate penetration. Conversely, a high value of shear stiffness results in a "brittle" behaviour in shear such that failure occurs at a small shear deformation. A high value of K_s in the model causes a rapid progressive failure of shear elements resulting in a low value of the shear stiffness of the system starting at a small value of plate penetration and thus applying for most of the penetration process.

The corresponding plate stress–penetration curves for 30-day-old snow are shown in Fig. 10(b). The agreement between experimental and predicted curves is not as good as for the 4-day-old snow especially for the higher values of K_s, but K_s 4500 yields relatively good results. Again, the predicted curves are bi-linear, but to a lesser degree than those for 4-day-old snow. The analytical model is consistent in that its sensitivity parameters are similar to those for 4-day-old snow; an increase in K_s results in a lower plate stress–penetration response and vice versa. It is also interesting to note that, as for 4-day-old, predictions are quite good when the shear stiffness parameter K_s is 4500.

Partition of total plate resistance

In the finite element model, provisions were made for determining the individual components of plate penetration resistance:

(a) resistance due to shear along the planes of shear;

(b) resistance due to compression of snow inside the pressure bulb, i.e. snow beneath the plate and bounded by the shearing planes;

(c) resistance due to compression of snow outside the shearing planes.

The predicted distribution of the three components of plate penetration resistance for both types of snow is graphically displayed in Fig. 11(a) and (b) for the best predicted curves. For both types of snow, the greatest component of plate resistance is that of compression beneath the plate followed by that due to shear along the failure planes. Compression outside the shearing planes stays practically constant and contributes very little to the total plate resistance in both cases. The relative magnitudes pertaining to compression and shear vary with the age of the snow and with plate penetration. For 4-day-old snow, the plate resistance due to shear is approximately half of that due to compression beneath the plate for low penetration values and decreases to about 20% of the latter value at the highest penetration. This is a result of less load being carried in shear as more shear elements have failed at higher plate penetration. In the case of 30-day-old snow, the shear strength of the snow is higher and plate resistance due to shear contributes a greater percentage of the total response as shown in Fig. 11(b).

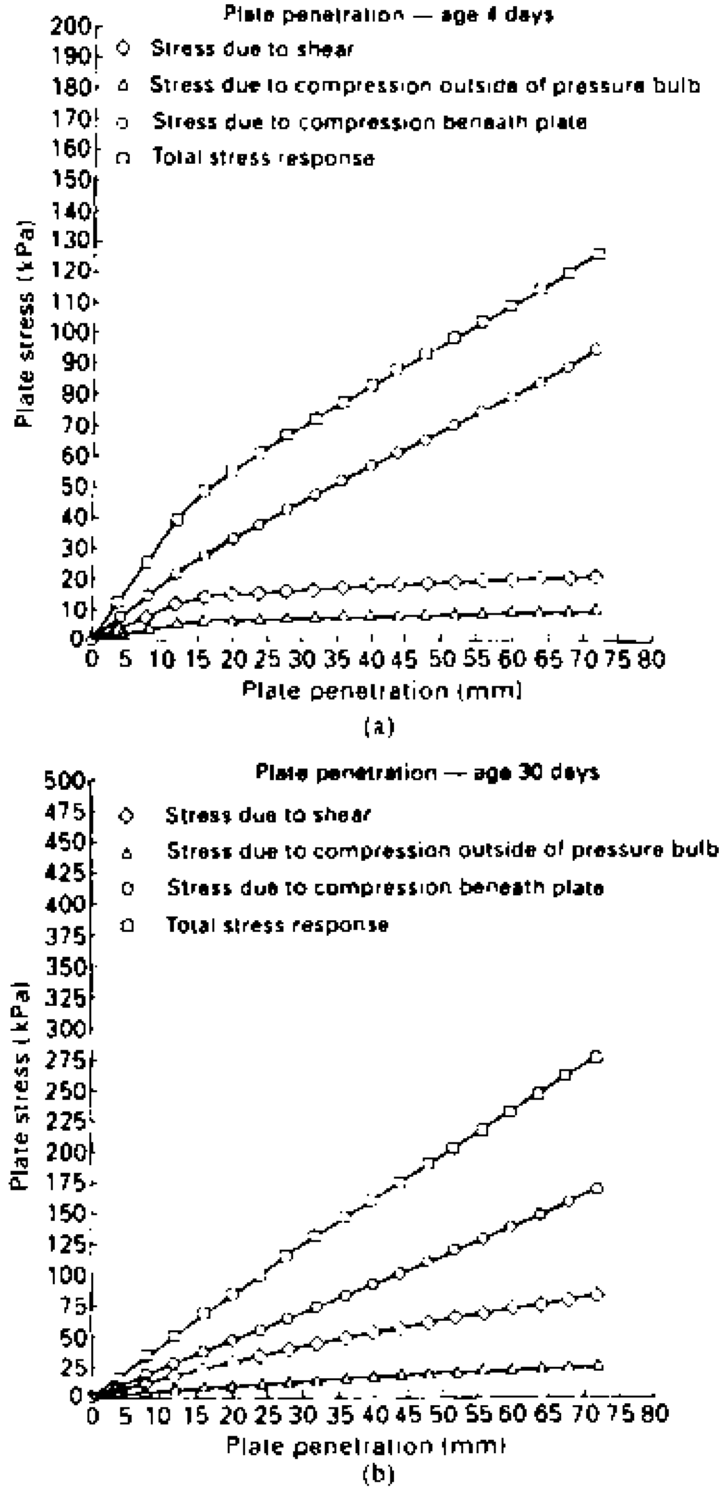

FIG. 11. (a) Finite element prediction of distribution of components of total plate resistance: age 4 days; (b) finite element prediction of distribution of components of total plate resistance: age 30 days.

The above relative amounts of plate resistance due to compression and shear are consistent with results obtained by Metaxas [8].

Displacement fields

In this study, the similarity between experimentally obtained and predicted displacement fields is established in terms of vertical displacement profiles only. Observations during plate tests and grid line photographs showed that, by and large, horizontal displacements in the snow mass were negligible and could therefore be omitted from the comparative study.

The experimental and predicted cumulative vertical displacement under two points below the plate center for 4-day old snow at penetrations of 36 mm and 64 mm are shown in Fig. 12(a) and (b) respectively. Predicted vertical displacement profiles were obtained from the displacement of selected nodes originally located at a given distance away from the plate. For both plate positions, the agreement between the experimental and analytical values is good especially for points originally less than 1.5 plate lengths away from the original snow surface. Experimental and predicted values diverge from each other for some distance below and then seem to converge again. A similar comparison between vertical displacement profiles under a point some distance away from the plate center for the same plate penetrations is illustrated in Fig. 12(c) and (d) respectively. For a plate displacement of 36 mm, the agreement between experimental and predicted values is again very good for points originally located less than 1.5 plate lengths from the original snow surface. The above diverge-converge effect between experimental and predicted displacement values is also observed in this case. For a plate penetration of 64 mm, the discrepancy is more uniform along the curve(s).

It should be noted that for a given plate penetration, both experimental and predicted displacement profiles are essentially linear up to a certain depth, thus simplifying a uniform vertical strain distribution, and are characterized by a change in gradient below that depth. The change in slope of the displacement profile is mainly due to the variation in stiffness of the system in shear. As discussed earlier, shear elements along the plate of cutting shear fail progressively so that for a given plate penetration, snow has failed above a certain point and has not failed below the same point. The stiffness to the system is thus lower above the given point and higher below so that displacements are also expected to be higher for the region of lower stiffness. As a result, the gradient of the displacement profile, or strain, is also expected to be higher for the less stiff snow and lower for the stiffer snow. The change of displacement gradient is particularly obvious in the profiles shown in Fig. 12(a) and (c). The above arguments thus seem to imply a relationship between the point of change in displacement gradient and the point above which the snow has failed completely, i.e. depth of full shear.

The predicted displacement profiles in Fig. 12(a) to (d) also show their sensitivity to the shear stiffness parameter K_s, which in all cases, proves to be relatively small and, in any case, lower than that observed for the plate stress–penetration curves.

The displacement profiles obtained for 30-day-old snow below two different points on the plate and for two plate penetrations are shown in Fig. 13(a) to (d). The agreement between experimental and predicted values can be seen to be very good. As for 4-day-old snow, the displacement profiles are linear for some depth and then feature a change in slope, the reasons for which have already been previously discussed. Also, as for 4-day-old snow, it appears that the shear stiffness parameter K_s has less effect on the resulting displacement profile than on plate penetration response.

Depth of full shear

The depth of full shear D_s is a description of the plate–snow system which quantifies the progressive shear failure mechanism generated by the plate penetration

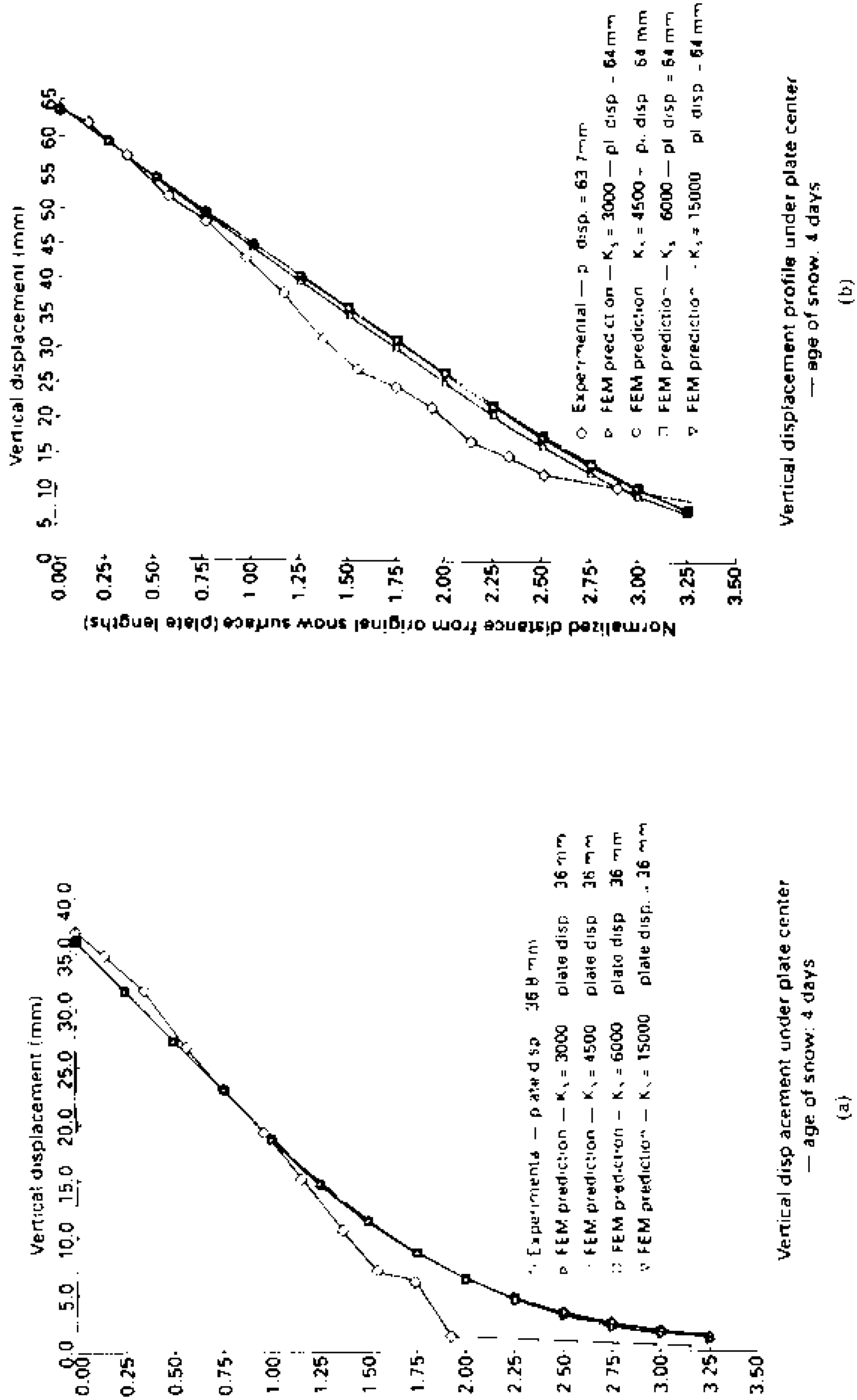

FIG. 12. (a) and (b) Caption on p. 245.

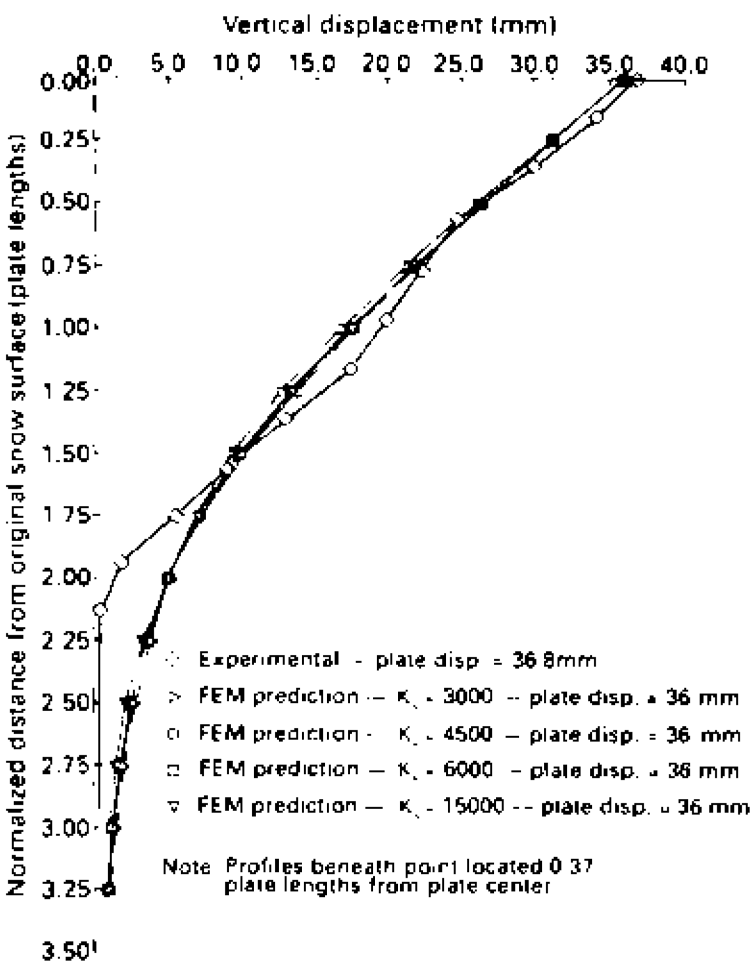

Vertical displacement profile — age of snow: 4 days

(c)

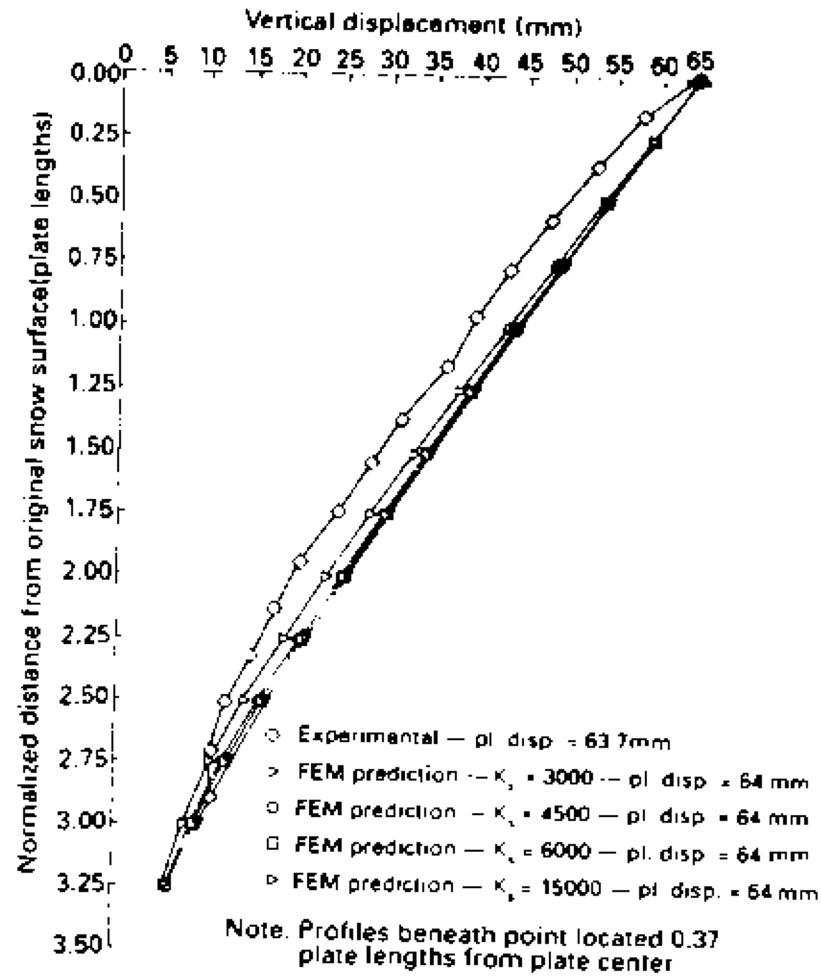

Vertical displacement profile — age of snow: 4 days

(d)

FIG. 12 (a) Experimentally obtained and predicted displacement profiles under plate center: age 4 days (plate penetration = 36 mm); (b) experimentally obtained and predicted displacement profiles under plate center: age 4 days (plate penetration = 64 mm); (c) experimentally obtained and predicted displacement profiles: age 4 days (plate penetration = 36 mm); (d) experimentally obtained and predicted displacement profiles: age 4 days (plate penetration = 64 mm).

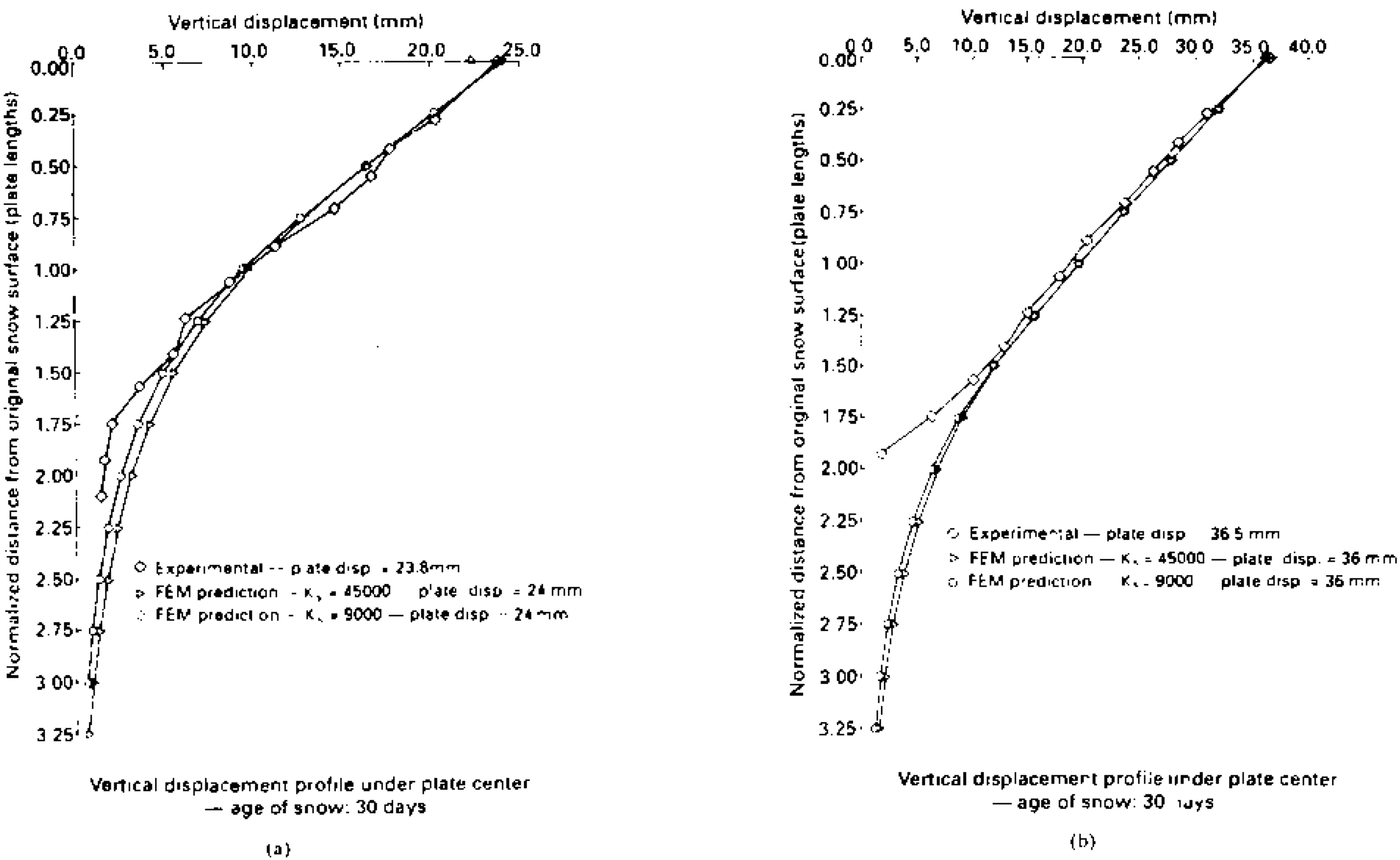

FIG. 13 (a) and (b) Caption on p. 247.

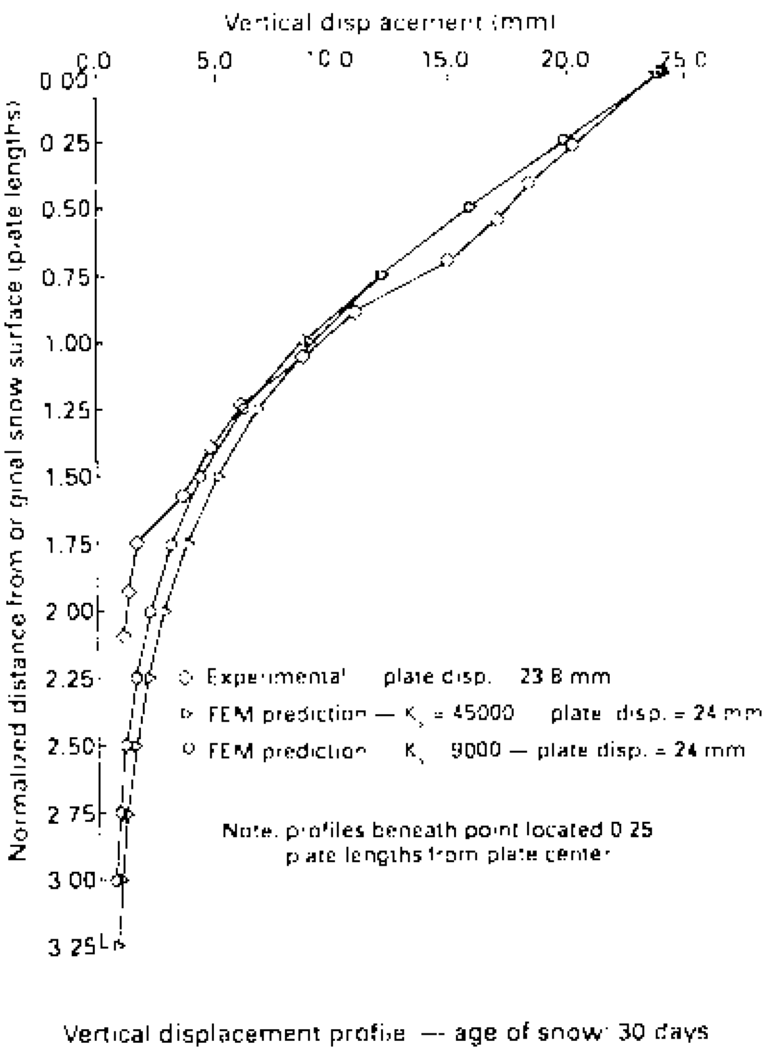

(c)

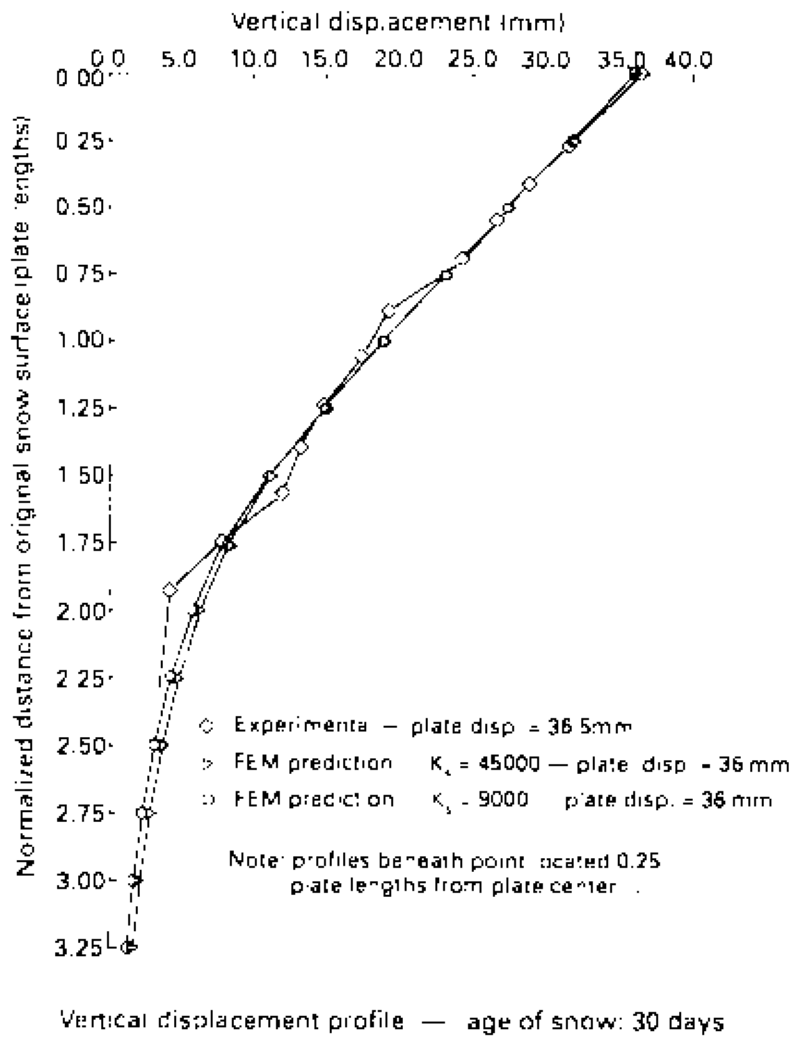

(d)

FIG. 13 (a) Experimentally obtained and predicted displacement profiles under plate center: age 30 days (plate penetration 24 mm); (b) experimentally obtained and predicted displacement profiles under plate center: age 30 days (plate penetration – 36 mm), (c) experimentally obtained and predicted displacement profiles: age 30 days (plate penetration – 24 mm); (d) experimentally obtained and predicted displacement profiles: age 30 days (plate penetration – 36 mm).

process. The predicted values of depth of full shear D_s are obtained from the finite element analysis which, for each increment, updates the values of total shear deformation for each joint element along the plate of shear. The depth of full shear value D_s is obtained by searching the deepest element for which the total shear deformation is greater or equal to the original depth.

For 4-day-old snow, a comparison between experimental and predicted values of D_s for various values of the shear stiffness parameter D_s is presented in Table 1. The tabulated values are consistent with the sensitivity analysis performed for the plate penetration response of the 4-day-old snow in that there exists an optimum value of K_s which generates a shear depth value quite close to the experimental one obtained from plate penetration test photographs. As for the plate stress–penetration response, reasonable agreement between experimental and predicted values is obtained for the range of K_s values considered. Best are obtained for values of $K_s = 4500$ and $K_s = 3000$. For the lower value of shear stiffness, the predicted shear depth implies that the failing mechanism along the planes of shear does not extend as deep as for the actual plate penetration test whereas the opposite applies for the higher K_s value thus indicating that the best prediction of D_s would be using a K_s value in between the above two values.

Depth of full shear values for 30-day-old snow are shown in Table 2. For a plate penetration of 24 mm, the discrepancy between experimental and predicted values is considerable for both values of shear stiffness K_s considered whereas much better agreement is obtained for a plate penetration equal to 36 mm. Note that for

TABLE 1. EXPERIMENTAL AND PREDICTED DEPTH OF FULL SHEAR: AGE 4 DAYS

	Plate Pen (mm)	K_s	D_s (mm)
Experimental	36.8	—	80.6
Predicted	36.0	15000	97.4
"	36.0	9000	93.3
"	36.0	6000	93.1
"	36.0	4500	92.8
"	36.0	3000	73.7
Experimental	63.7	—	135.2
Predicted	64.0	15000	166.3
"	64.0	9000	166.4
"	64.0	6000	162.4
"	64.0	4500	158.2
"	64.0	3000	124.1

TABLE 2. EXPERIMENTAL AND PREDICTED DEPTH OF FULL SHEAR: AGE 30 DAYS

	Plate pen. (mm)	K_s	D_s (mm)
Experimental	23.8	—	34.5
Predicted	24.0	9000	52.7
"	24.0	4500	60.9
Experimental	36.5	—	97.8
Predicted	36.0	9000	88.9
"	36.0	4500	93.2

30-day-old snow, the sensitivity analysis intentionally involves fewer values of the shear stiffness K_s since information about realistic values of K_s was already available from the computer runs for 4-day-old snow.

The relationship between the point of change in gradient of the displacement profile and the depth of full shear can now be verified. For the 4-day-old snow, inspection of Fig. 12(a) and (c) shows that for a plate displacement of 36 mm, the point of change of displacement gradient in the case of the actual experiment occurs at a depth of approximately 1.9 plate length whereas of this prediction, this value is about 1.5 plate length. From Table 1, the experimental value of depth of shear is 81 mm to which the plate penetration value of 37 mm must be added for a proper comparison with the values obtained from displacement profiles. The resulting value is therefore 118 mm or 1.67 plate length. Predicted values of depth of full shear from Table 1 corresponding to a plate displacement of 36 mm is about 95 mm which when added to the plate penetration value yields a value of 131 mm or 1.86 plate lengths. For a plate displacement of 64 mm, Fig. 12(b) and (d) indicate that the change in slope of the displacement profile, although not as obvious, occurs at a distance between 2.0 and 2.25 plate length for both the actual case and the prediction. Table 1 shows experimental and predicted values of depth of full shear of 135 mm and about 165 mm respectively which, when adjusted for plate penetration, yield values of 199 mm (2.82 plate length) and 229.0 mm (3.24 plate length).

Similarly, in the case of 30-day-old snow and for a plate penetration of 36 mm, Fig. 13(b) and (b) show that the change in gradient of the displacement profile occurs at a depth of approximately 1.75–2.0 plate lengths below the original snow surface. Consultation of Table 2 indicates experimental and predicted values of shear depth of 98 mm and approximately 90 mm, which, when corrected for plate displacement, correspond to 134 mm (1.9 plate length) and 126 mm (1.8 plate length). For a plate displacement of 24 mm, the agreement between depth of full shear and point of change of displacement gradient is quite poor.

The above comparison between the point of change of displacement gradient and the depth of full shear is summarized in Table 3 and shows that in general there seems to exist a relationship between the two parameters.

Density profiles

Density profiles derived from the change in area of square elements of the grid photographed during plate penetration tests and those predicted by the finite element model are displayed in Fig. 14(a)–(h) for both types of snow used. As shown in the plots, the experimental profiles feature a considerable scattering of the points

TABLE 3. DEPTH FULL SHEAR VERSUS POINT OF CHANGE OF DISPLACEMENT GRADIENT

Age of snow (days)	Plate penetration (mm)	Depth of full shear D_s (plate lengths)		Point of change of displacement profile (plate lengths)	
		Exp.	Pred.	Exp.	Pred.
4	36	1.67	1.86	1.9	1.5
4	64	2.82	3.24	2.0 –2.25	2.0 –2.25
30	24	0.5	0.9	1.5 –1.75	1.5 –1.75
30	36	1.9	1.8	1.75–2.0	1.75–2.0

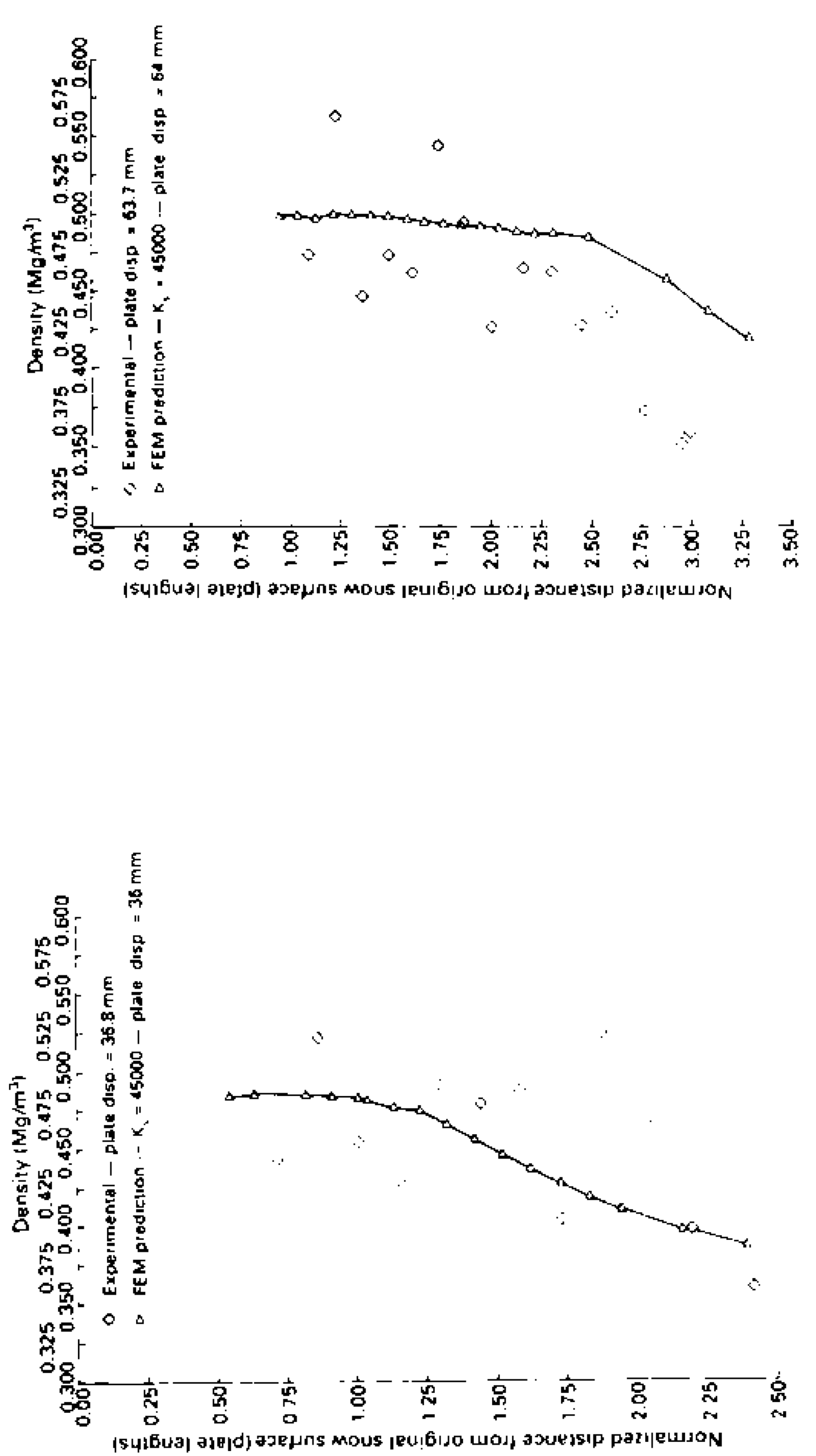

Density profile under plate center — age of snow: 4 days
(a)

Density profile under plate center — age of snow: 4 days
(b)

FIG. 14. (a) and (b) Caption on p. 253.

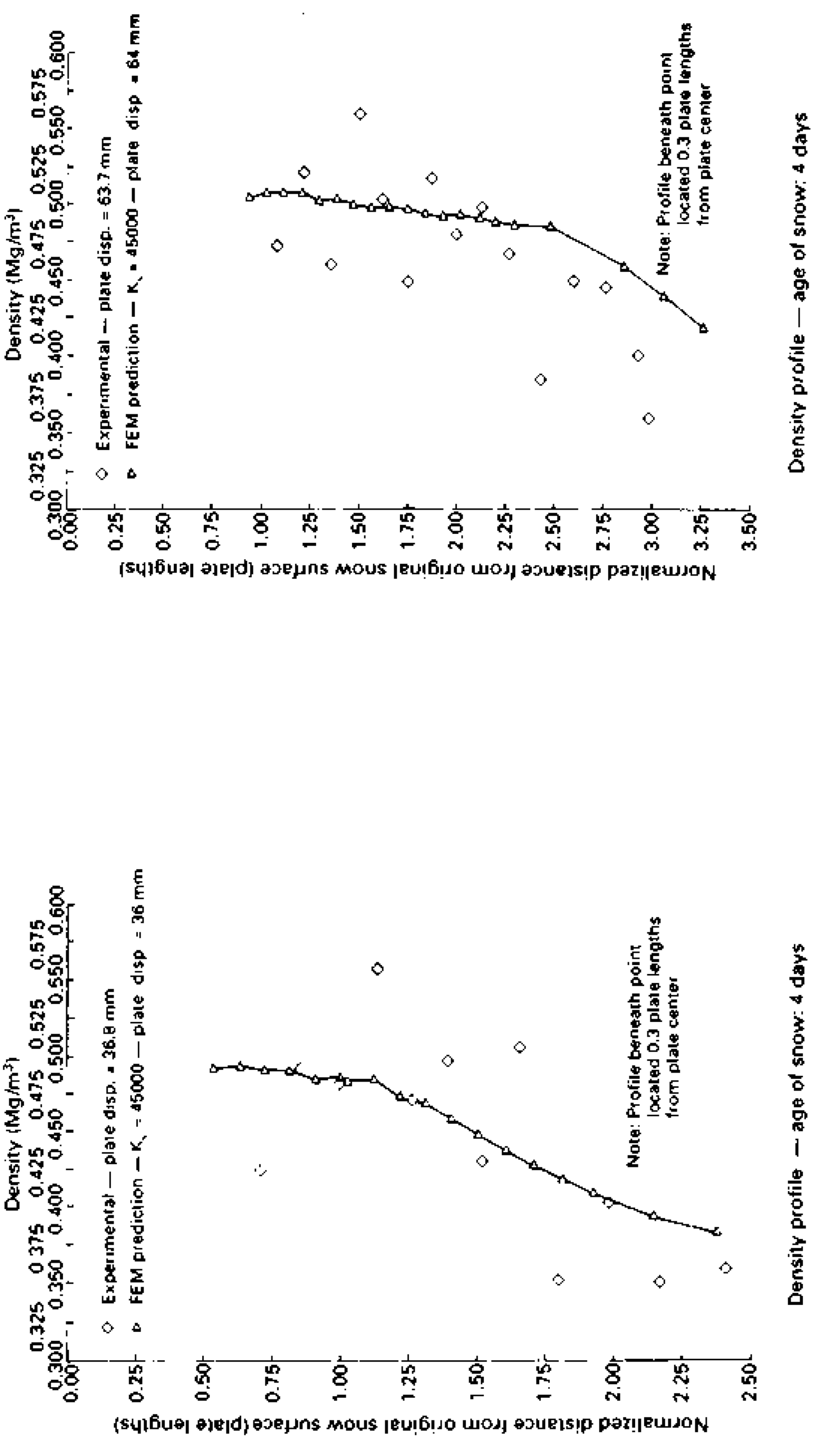

FIG. 14. (c) and (d) Caption on p. 253.

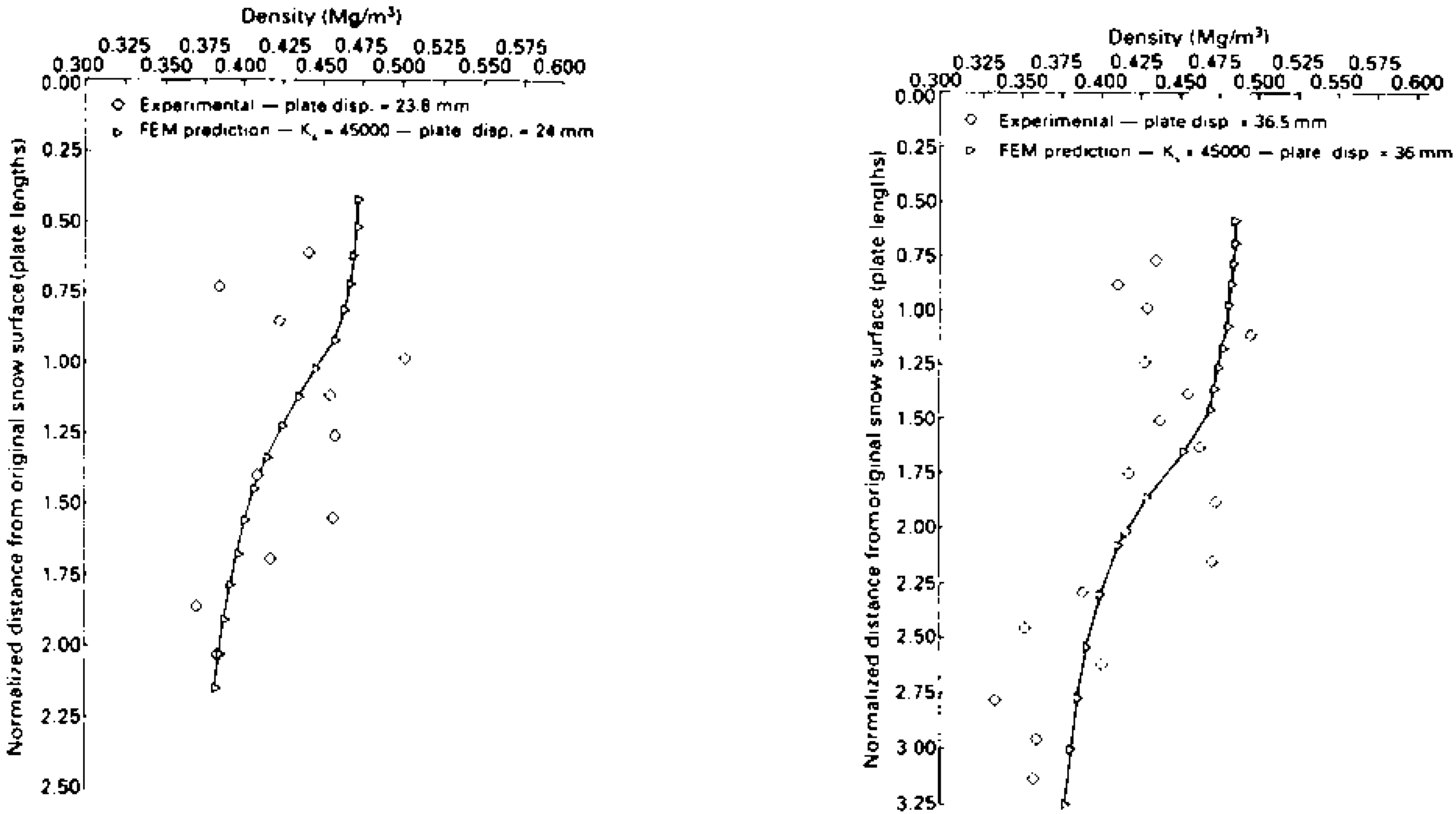

Density profile under plate center — age of snow. 30 days

(e)

Density profile under plate center — age of snow: 30 days

(f)

FIG. 14. (e) and (f) Caption on p. 253.

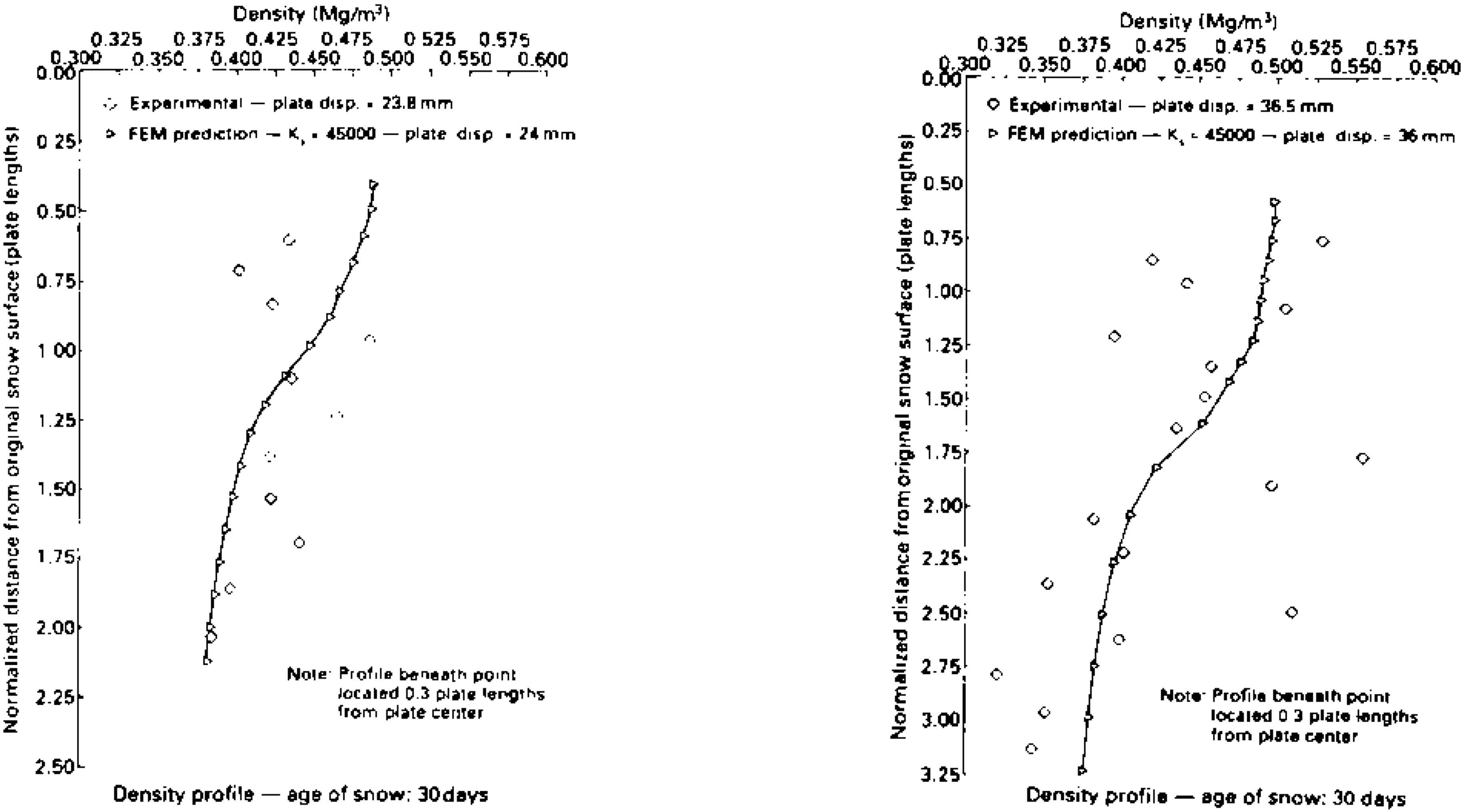

(g) (h)

FIG. 14. (a) Experimentally obtained and predicted density profiles under plate center: age 4 days (plate penetration = 36 mm); (b) experimentally obtained and predicted density profiles under plate center: age 4 days (plate penetration = 64 mm), (c) experimentally obtained and predicted density profiles: age 4 days (plate penetration = 36 mm); (d) experimentally obtained and predicted density profiles: age 4 days (plate penetration = 64 mm), (e) experimentally obtained and predicted density profiles under plate center: age 30 days (plate penetration = 64 mm); (f) experimentally obtained and predicted density profiles under plate center: age 30 days (plate penetration = 36 mm); (g) experimentally obtained and predicted density profiles: age 30 days (plate penetration = 64 mm); (h) experimentally obtained and predicted density profiles: age 30 days (plate penetration = 36 mm).

although following more or less the same pattern as the predicted ones, i.e. density decreases with depth. The predicted density profiles are, of course, more clearly defined and in all cases, are characterized by a more or less constant value for some depth below the plate followed by a decrease towards the initial density (prior to loading). This is therefore consistent with the predicted (and experimental) displacement profiles which followed a similar pattern by which a linear displacement profile implies a constant degree of strain. Since in the present loading situation a relationship between vertical strain and density clearly exists, it is hence not surprising to observe a uniform density of some depth below the plate.

The agreement between the experimental and the predicted density profiles can be said to be satisfactory in so far as the trends are similar. The scattering of experimental values, mainly due to the probably non-uniform density distribution of the snow deposit prior to loading, does not allow an accurate comparison between individual, experimental and predicted density values along the profiles.

Load distribution on the plate

The developed model has the capability of predicting the load distribution on the plate as a function of plate penetration. Load at a given point along the plate is computed as the product of the reaction on a given node representing the plate–snow interface in the finite element mesh and the plate width since the problem is analysed in terms of plane strain conditions.

The load distribution on the plate for several levels of plate penetration and for both types of snow used are shown in Fig. 15(a) and (b). In both cases, the distributions follow the same trend in that the portion of load carried increased from the center to the edges of the plate. Points near the plate center are subjected to reactions resulting from the resistance of the snow to undergo volume change. At or near the edges, the snow tends to simultaneously compress and shear along the failure planes so that an additional resisting force is involved. The predicted behavior is therefore as expected.

CONCLUSIONS

On the basis of the tests performed and the results of the developed predicting analytical model, the following conclusions may be drawn:

(1) The compressive modulus of snow, as shown in by confined compression tests, increased with density. A stiffening type of curve was obtained for all tests on both types of snow used. As expected, the response of 30-day-old snow was stiffer due to the higher degree of sintering.

(2) The shear strength of snow increased with age, due to the greater strength of bonds between particles, and with density, as demonstrated by results of vane shear tests.

(3) The experimental plate stress–penetration curves were essentially bi-linear with a change of slope occurring relatively early in the penetration process. Significant stress vibration due to microfracturing was observed.

(4) A method to model a highly compressible non-linear material which failed according to a punching shear type of mechanism was developed. The model includes the effect on non-linearity and strain hardening behavior in compression as well as the effect of shear stresses generated along the vertical sides of the pressure bulb. The

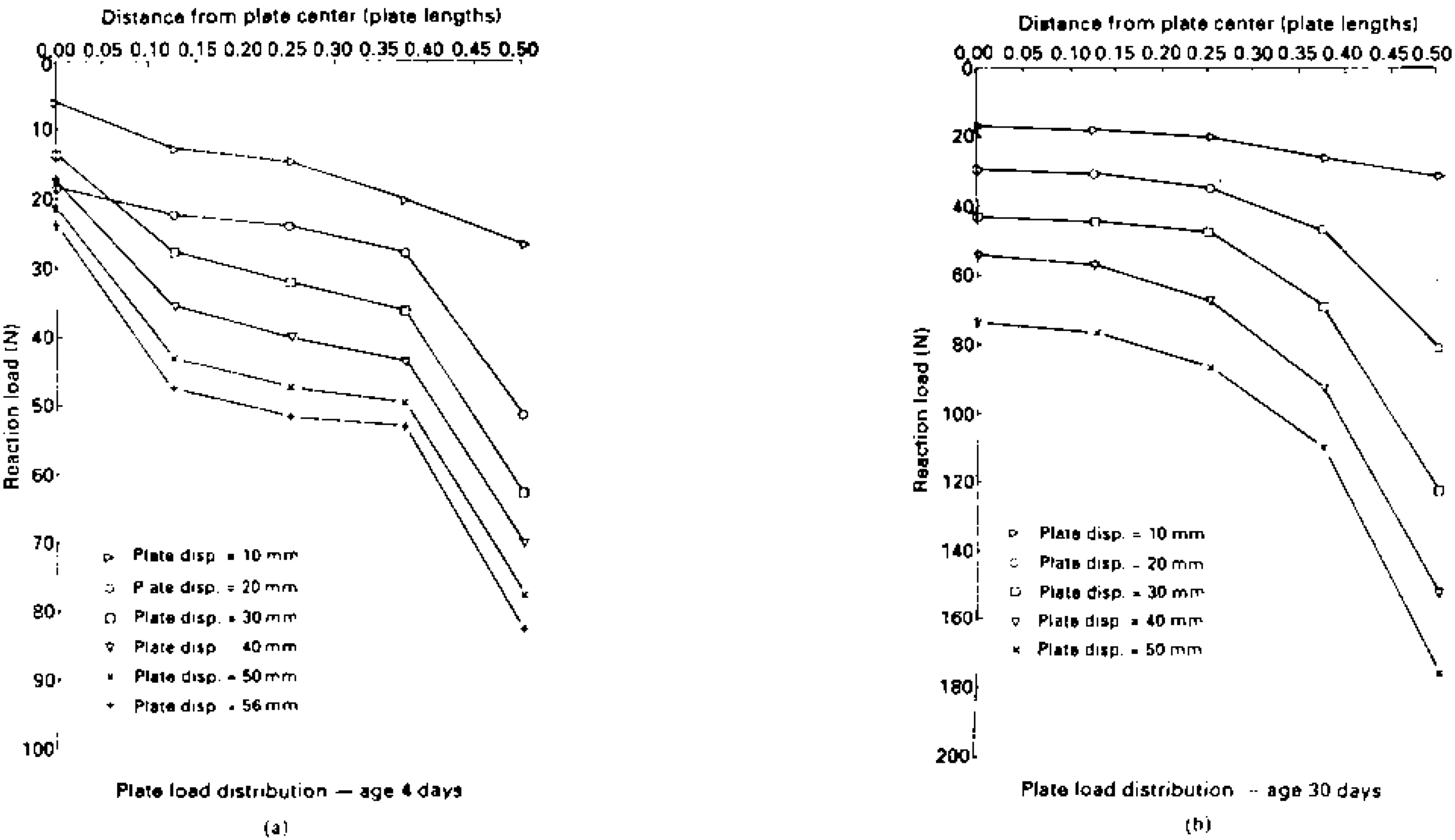

FIG. 15. (a) Load distribution under plate footing: age 4 days (K_s = 4500); (b) load distribution under plate footing, age 30 days (K_s = 4500)

maximum shear stress tolerated by a shear element was limited by its shear strength which in turn depended on density. Provisions were made to simulate this effect so that the model includes an algorithm by which excess shear stress in failing joint elements are redistributed within the snow mass. The shear stress in any shear element never exceeds the value corresponding to its shear strength.

(5) The plate resistance–penetration curves as predicted by the analytical model compared rather well with the experimentally obtained ones. The predicted response was somewhat sensitive to the single value of shear stiffness employed in the model but a value of 4500 for this parameter gave satisfactory results for both types of snow used. As expected, the predicted value for 30-day-old snow is higher than that for 4-day-old snow. The good agreement between predicted and experimental plate stress–penetration curves demonstrates the ability of the proposed model to simulate the plate penetration mechanism.

(6) The predicted displacement depth profiles below the plate were, in general, in good agreement with the ones derived from experimental data. In both cases, the displacement profiles were found to be linear with a change of slope occurring at some depth more or less related to the degree of failure exhibited along the planes of cutting shear. Displacements and strains were found to be greater in the snow above the point of displacement gradient change. The displacement profile prediction was less sensitive than the plate penetration response to the change in shear stiffness.

(7) The predicted values of depth of full shear, which are representative of the degree of failure along the planes of cutting shear were, in general, in relatively good agreement with those obtained from analysis of experimental data. The proposed relationships between the values and the point of displacement gradient change was established.

(8) Density profiles obtained experimentally yield scattered results probably due to the initial non-uniform density distribution with depth and the non-homogeneity of the material. Predicted density profiles were smooth continuous curves whose shape was consistent with the predicted displacement profiles. Comparison of experimental and predicted results was difficult due to the degree of scattering of experimental points. But predicted curves, in general, fitted the points reasonably well.

(9) The predicted load distribution on the plate was such that a greater portion of the reaction load was carried by the edges of the plate. This is mainly due to the additional resistance of the snow to shear along the failure planes. The effect was more pronounced for 4-day-old snow.

(10) Discrepancies between predicted and experimental values of parameters describing the plate penetration mechanism were due to combined effects of the following:

(a) Deposition of snow in the deep boxes was performed with care but nevertheless resulted in a non-homogeneous layer of non-uniform density. In addition, snow is not isotropic in reality.

(b) The presence of some friction between the snow and the sides of the plexiglas boxes and that existing between the snow sample and the walls of the confined compression test cylinders.

(c) The problem is not exactly plane strain since, in reality, stresses, strains, displacements, etc., also vary across the width of the plate.

(d) The behavior of snow in shear is possibly such that shear stiffness is not constant and may actually vary with density. The stress–deformation curve in shear may thus be non-linear. Also, during vane shear test, snow is not sheared at an absolutely constant value of density due to the compressing action of the blades on the snow upon rotation of the vane.

(e) The viscous nature of the material is such that its response is quite sensitive to strain rate, particularly in the case of shear. An implicitly assumed uniform strain rate field generated in the snow may be an additional source of error.

(f) The algorithm developed on the basis of the finite element method involves assumptions and idealizations, such as the handling of the large volume change behavior of the material by a stress-strain curve updating procedure.

(g) Good replication of snow samples is very difficult due to the thermodynamic activity of the material and its sensitivity to variation in surrounding conditions such as temperature, humidity, wind and light.

(h) Similarly, the correspondence of snow produced for confined compression and plate penetration tests is questionable due to the different thermal isolation conditions.

Acknowledgements The work performed in this study was in partial fulfillment of the study requirements for Defence Research Establishment Suffield (DRES) under contract arrangement with Department of Supply and Services (DSS), Canada.

REFERENCES

[1] P. V. Hobbs, Ice in the atmosphere: review of the present position. *Physics and Chemistry of Ice* (edited by E. Whalley *et al.*), pp. 208–319. R. Soc. Can., Ottawa (1973).
[2] R. I. Perla and M. Martinelli Jr, *Avalanche Handbook*. Agricu. Handbook, No. 489, U.S. Govt. Printing Office, Washington, D.C. (1976).
[3] C. Fraser, *Avalanches and Snow Safety*. Scribet and Sons, New York, N. Y. (1978).
[4] W. L. Harrison, Vehicle Performance over Snow: Mathematical Model Validation Study. CRREL, Technical Report 268 (1975).
[5] R. N. Yong, Snow traction mechanics. *Proc. ISTVS Workshop on Snow Traction Mechanics, Alta, Utah* (1979).
[6] R. L. Brown, Applications of energetics to vehicle trafficability problems. *Proc. ISTVS Workshop on Snow Traction Mechanics, Alta, Utah* (1979).
[7] G. E. H. Ballard and R. W. McGaw, A theory of snow failure. U.S. Cold Regions Research and Engineering Laboratory. Research Report 137 (1965).
[8] I. Metaxas, Snow Mechanics: Mechanical Properties, Energy Analysis. Master's Thesis, McGill University, Montreal (1984).
[9] R. E. Goodman, R. Taylor and T. L. Brekke, A model for the mechanics of jointed rock. *J. Soil Mech. Foundations Div. ASCE* **94** (SM3), 637–659 (1968).
[10] A. W. Hanna, Finite Element Analysis of Soil Cutting and Traction. Ph.D. Thesis, McGill University (1975).
[11] O. C. Zienkiewicz, *The Finite Element Method*, 3rd Edn. McGraw-Hill, London (1977).
[12] R. N. Yong, A. M. O. Mohamed and R. G. Tali, Non-linear stress analysis of muskeg via finite element. *Can. Geotech. J.* **28** (4), 613–629 (1991).
[13] R. N. Yong and M. Fukue, Performance of snow in confined compression. *J. Terramechanics* **14** (2), 59–82 (1977).

International Society for Terrain-Vehicle Systems
Proceedings of the 4th Regional North American Meeting
Sacramento, CA, March 25-27, 1992

TRAFFICABILITY EVALUATION OF DEEP SNOWPACK

G.J. Irwin[1], D.M. Xu[2], A.M.O. Mohamed[2] and R.N. Yong[2]

ABSTRACT

This study examines the relationship between measured deep snowpack properties and developed vehicle sinkage as a measure of trafficability. A snow model which makes reference to a plate footing is proposed for the purpose of obtaining basic parameters of snow from plate footing data. Basic to the model is the analytical calculation of the depth of the pressure bulb formed below the plate footing. From a prediction of deep snow trafficability infered by the model, vehicle mobility may be evaluated.

INTRODUCTION

Since the terms "mobility" and "trafficability" are often erroneously used interchangeably by many individuals, it is useful to indicate that the terms refer to specific performance requirements for vehicles and the supporting deep snowpack. The term "mobility" is used in the context of a vehicle and refers to the demonstrated ability of a vehicle to perform a surface traverse over a designated route, whereas the term trafficability refers to the supporting snowpack required to provide flotation and traction for the surface traverse of a vehicle. Obviously, the vehicle that is required to perform the traverse is the common link between mobility and trafficability.

The trafficability of deep snow has traditionally been a major concern in cold climates with heavy precipitation where vehicle operators want to be assured of a GO capability. The consequent mobility of a particular vehicle configuration is thus basic to the quality or efficiency of job completion when transiting between points. Vehicle footing is, through design, dimensioned to control sinkage yet achieve sufficient substrate strength as to develop the necessary traction for mobility. This paper addresses the problem of load-deformation relationship; how they are affected by deep snow conditions and how a solution may lead to a confident prediction of GO or NO GO performance of over snow vehicles.

---

1 Defence Reseach Establishment Suffield, Military Engineering Section, P.O. Box 4000, Medicine Hat, Alberta, Canada T1A 8K6

2 Geotechnical Research Centre, McGill University, 817 Shebrooke St. West, Montreal, Quebec, Canada H3A 2K6

TRAFFICABILITY EVALUATION

The assessment of snow trafficability, i.e., the measurement of its ability to support a vehicle and provide adequate friction for traction, has involved several experimental test techniques. Namely these include load application by a plate footing, by indentation with a cone or Rammsonde or by a vane shear apparatus. The results may be complicated by a size dependence on the testing equipement. A suitable model of snow deformation would relate snow basic mechanical properties such as compression and shear parameters with the test method. Through experience the use of the plate footing is considered to be the preferred test method as it yields data of relatively low variability in a given snow condition.

MODEL FORMULATION

Plate Footing Test In field condition the plate footing test is conveniently conducted manually and involves the vertical penetration of snow usually with a circular rigid plate (Fig. 1). Load and sinkage are recorded at intervals. As supporting information, a standard snow classification is conducted so as to include profiles of temperature and density with depth along with stage of metamorphic development. The latter might be age of layers since deposition, or alternatively snow grain shape, size and nature of intergranular bonding. The size of plate chosen should be as large as will permit the attainment of a limiting maximum density during compression of snow while the range of applied pressure covers the expected ground pressure of a given vehicle. In Figs. 2 and 3 one may compare the effect of ageing on the pressure-sinkage relationship. Natural snow is relatively insensitive while manufactured snow implies a limiting density (or displacement) by the sharp rise of the curve in Fig. 3.

Model Development During plate indentation, resistance to load is developed within two areas of the deformation zone or pressure bulb as illustrated in Fig. 4 [1]. Area "A" is identified with shearing resistance at the zone periphery and B indicates the resistance of compression within the zone. The balance of forces may be presented thus:

$$P\left(\frac{\pi D^2}{4}\right)=\tau(\pi DH)+\sigma\left(\frac{\pi D^2}{4}\right) \qquad (1)$$

where: H is the pressure bulb depth, τ is the peripheral shear stress, p is applied pressure, σ is normal stress resistance at any level inside the bulb and D is plate diameter.

Snowcover is considered deep if snow deformation, i.e., the lower edge of the pressure bulb, does not intersect the base of the snowpack at ground level.

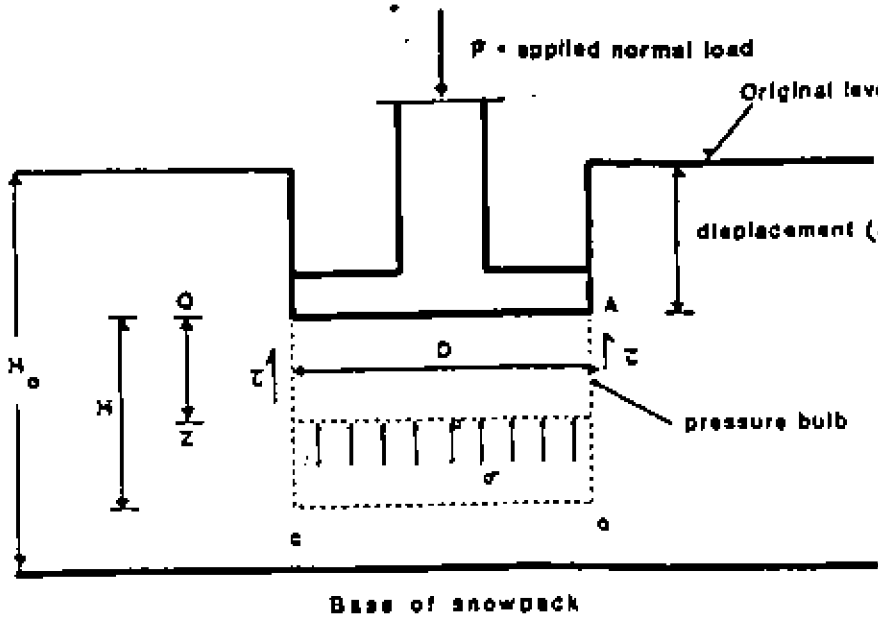

δ = sinkage; τ = shear resistance; σ = penetration resistance ; D = footing plate diameter
H = depth of pressue bulb, and H_o = original depth of snow covering

Fig. 1 Force Equilibrium after Footing Penetration

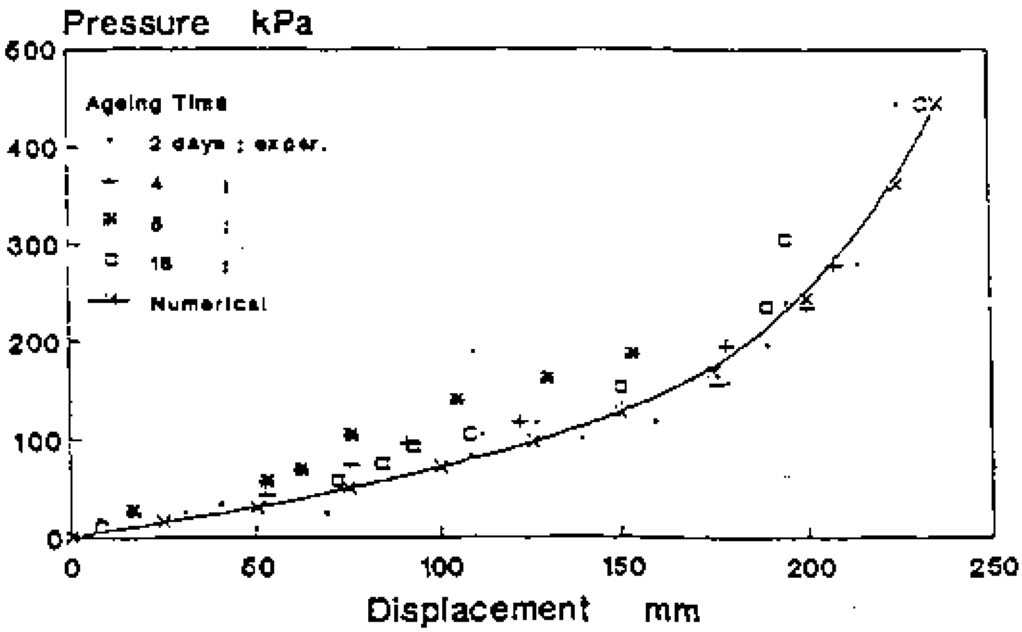

Natural Snow; Init. Dens. = 340 kg/m^3

Fig. 2 Pressure - Displacement Relations for Circular Footing (D = 101.6 mm)

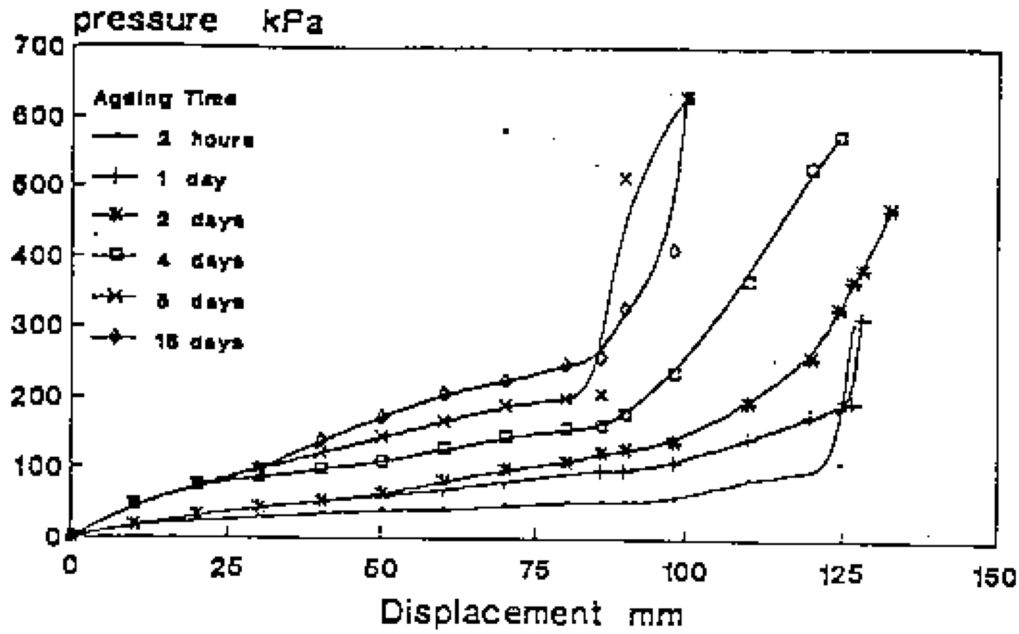

Manufactured Snow; init. Dens. = 480 kg/m ^{3}

Fig. 3 Pressure - Displacement Relations For Circular Footing (D = 101.6 mm)

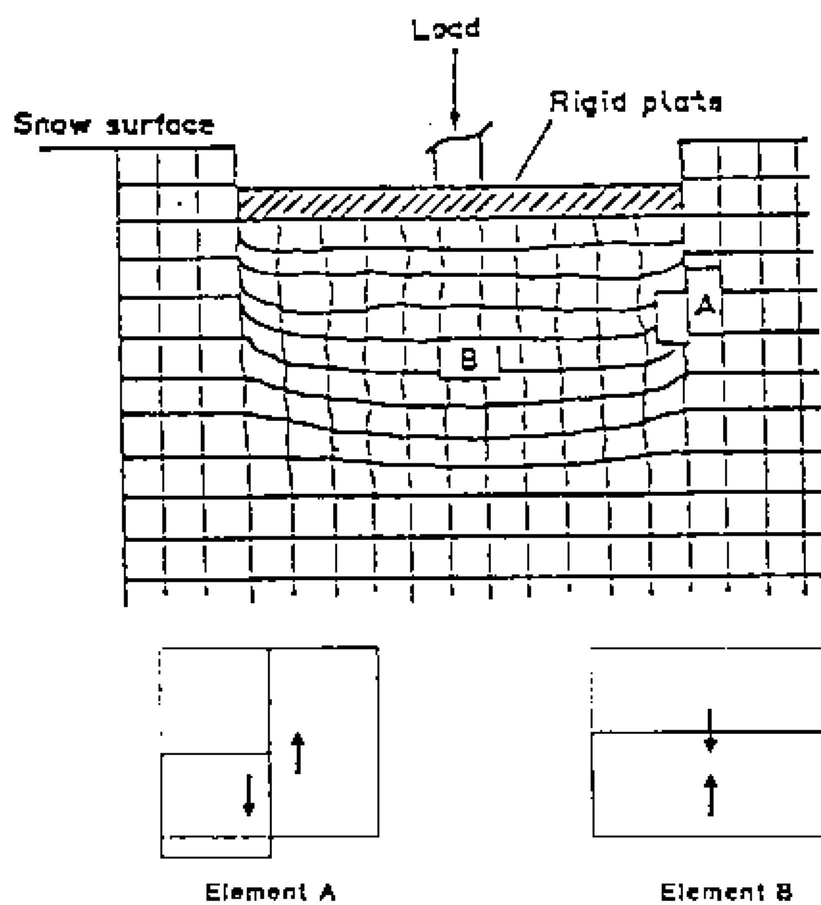

Fig. 4 Failure modes in snow during the penetration of rigid plate

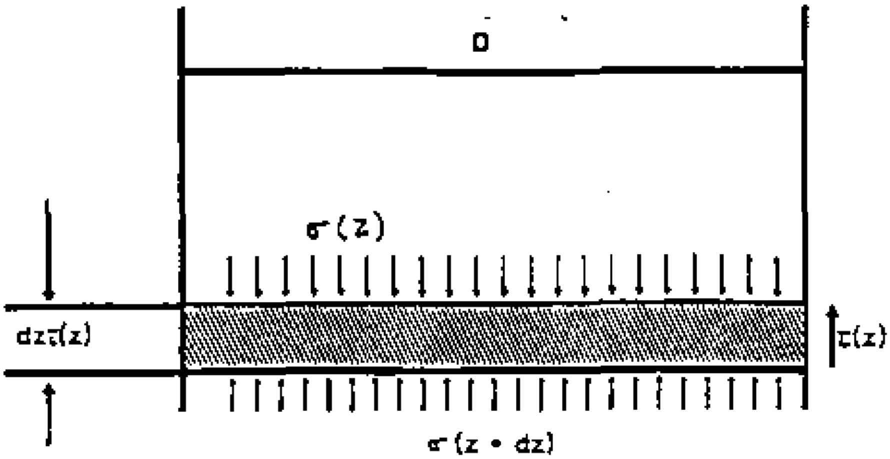

Fig. 5 Force equilibrium for snow dz element

Basic Assumptions The model is developed based on the following assumptions:

1. The zone of failure by slip is vertical at the plate edge,
2. Analysis is one dimensional and hence assumes that σ is uniformly distributed on any level cross section,
3. The depth of the pressure bulb corresponds to the applied load,
4. Outside the immediate zone of failure by slip, the snow medium is unaffected,
5. Snow obeys Coulomb's Law, and
6. Ageing does not affect natural snow.

Equations and Solution Taking an infinitesimal slice dz within the pressure bulb to analyze force equilibrium (Fig. 5):

$$\frac{d\sigma(z)}{dz}=\frac{4\tau(z)}{D} \tag{2}$$

Solving for σ *and* z and taking proper account of boundary condition, the depth of the pressure bulb, H, may be written as follows [2]:

$$H=\frac{pD}{2(c+p\ \tan\ \phi)} \tag{3}$$

where p is applied plate pressure, c and ϕ are Coulomb shear parameters applicable to initial snow density neighbouring the peripheral slip failure zone. It should be emphasized that these parameters may be determined by using: (1) experimental data from plate footing tests, and (2) numerical technique for minimization. Sinkage, δ, is given by:

$$\delta = \int_o^H \varepsilon dz \tag{4}$$

where ε is compressive strain. In turn

$$\varepsilon = \left(\frac{\rho(z)}{\rho_o} - 1 \right) \tag{5}$$

where $\rho(z)$ is snow density within the pressure bulb at depth z below the plate and ρ_o is initial density before disturbance by the plate footing. Through continued compression, snow density may be brought to an upper limit, ρ_c, at applied plate pressure, σ_c. Based on experimental data, the relationship between density and pressure may be expressed as:

$$\frac{\rho - \rho_o}{\rho_c - \rho_o} = \left(\frac{p}{\sigma_c} \right)^k \tag{6}$$

where ρ_c is the critical density of snow; ρ_o is snow initial density; ρ is snow density at any applied pressue, p; σ_c is maximum applied pressure which corresponds to ρ_c, *and* k_c is a snow material parameter. From experimental data in laboratory and field, the value of k is 0.25. The resulting relation between sinkage, δ, and snow parameters ρ_o, ρ_c, σ_c, and k yields [2]:

$$\delta = \frac{1}{3} \left(\frac{\rho_c - \rho_o}{\rho_o} \right) \cdot \left(\frac{pD}{c + p \tan \phi} \right) \cdot \left(\frac{p}{\sigma_c} \right)^k \tag{7}$$

Correlation A best fit to the δ-p curve of Fig. 2 yields $c=3$ *kPa*, $\phi=5.7°$ *and* $\sigma_c=425$ *kPa*. The theoretical curve presented by equation (7) agrees well with experimental curves for natural snow of varying initial density. Critical density, ρ_c, is experimentally observed [3] to be 600 kg/m^3. The values of c and ϕ above compare favourably with those reported by Blaisdell et al. [4] as c = 2.14 kPa and ϕ=6.8°.

For the prediction of trafficability for a tracked vehicle, equation (7) may be employed with the assumption that the track acts like a plate with uniform ground pressure distribution. From expressions for H, $\sigma(z)$ *and* $\tau(z)$, stress distributions and the depth of the pressure bulb may be calculated. A similar approach may be taken for a pneumatic tired vehicle in which the rubber footing deforms to a footing area dependent on load. Mobility evaluation of a vehicle may be derived from a knowledge of sinkage and bulb depth [5].

REMARKS AND CONCLUSIONS

The proposed plate footing model is intended to link snow basic parameters with prevalent vehicle features. To date only a single value of snow density explicitly represents snow condition although critical density, critical stress and snow parameter, k, probably depend on additional qualities of snow. It is to be noted that:

1. predictions of the model are in good agreement with plate footing test data; the basic parameters of c and ϕ obtained for natural snow are also in agreement with other work [4],
2. in deep snowpack, pressure bulb depth, H, is a useful concept which is closely tied to critical density,
3. the plate disk footing appears to be an effective tool for assessing snow trafficability and coulkd prove very practical when carried to remote locations.

ACKNOWLEDGEMENT

Contract support by arrangement with Department of Supply and Services in acknowledged.

REFERENCES

1. Yong, R.N. and Metaxas, I. (1985), "Influence of Age-Hardening and Strain-Rate on Confined Compression and Shear Behaviour of Snow, J. Terramechanics, Vol.2, No. 1, pp. 37-49.
2. Irwin, G.J., Xu, D.M., Mohamed, A.M.O., and Yong, R.N. (1991) "Analytical Model for Trafficability of Deep Snow" Submitted to J. of Terramechanis.
3. Yong, R.N., and Fukue, M. (1977), "Performance of Snow in Confined Compression", J. Terramechanics, Vol. 14, No. 2 pp, 59-32.
4. Blaisdell,G.L., Richmond, T.W., Shoop, S.A., Green, C.E., and Russell, G.A. (1990), "Wheels and Tracks in Snow (Validation Study of the CRREL Shallow Snow Mobility Model", CRREL Report 90-9, Hanover, New Hampshire, p. 72.
5. Xu, D.M., Mohamed, A.M.O., Yong, R.N., and Irwin, G.J., (1991) " Wheeled Vehicle Mobility Evaluation in Deep Snowpack" submitted to J. of Terramechanics.